# EXCITON MANAGEMENT IN METALLOPORPHYRINS AND THIAZOLOTHIAZOLE-BASED MATERIALS

by

Abhishek Shibu

A dissertation submitted to the faculty of
The University of North Carolina at Charlotte
in partial fulfillment of the requirements
for the degree of Doctor of Philosophy in
Nanoscale Science

Charlotte

2024

Approved by:

______________________________
Dr. Michael G. Walter

______________________________
Dr. Thomas A. Schmedake

______________________________
Dr. Christopher Bejger

______________________________
Dr. Lauren B. Woods

______________________________
Dr. Yong Zhang

# ABSTRACT

ABHISHEK SHIBU. Exciton Management in Metalloporphyrins and
Thiazolothiazole-Based Materials (Under the direction of DR. MICHAEL G. WALTER)

Over the last few decades, optical technologies utilizing organic materials in the solid state have become ubiquitous. In the solid state, contrary to their constituent molecules, organic materials exhibit energy level continuums along which excited-state energy (excitons) can diffuse. Controlled and efficient management of excitons in systems with numerous organic molecules packed in limited degrees of freedom has been the governing principle for organic optoelectronic devices. However, given the net neutral electrical charge of an exciton and the complex excited-state energy landscape in organic molecular aggregates, efficient management of excitons becomes a challenging task.

This dissertation presents three significant studies that explore the manipulation of exciton behavior in organic solid-state materials through self-assembly techniques. By modulating molecular packing in the solid state, the energetics and photophysical properties of the chromophores can be effectively controlled, opening up avenues for advanced optical and photonic applications. The successful modulation of exciton diffusion in Zn-metalloporphyrin solution-processable thin films and the establishment of a structure-photophysics correlation in disubstituted alkoxyphenyl thiazolo[5,4-*d*]thiazole (TTz)-based crystals demonstrate the potential of this approach. Furthermore, the controlled formation and relaxation kinetics of excimer-like states in asymmetric TTz films offer a novel route to achieving high luminescence efficiency, paving the way for a new generation of optical and photonic devices. These findings highlight the importance of self-assembly as a powerful tool for tailoring the behavior of excitons in organic chromophores, leading to significant advancements in various fields.

# ACKNOWLEDGEMENTS

The studies presented in this dissertation could not have been possible without the contributions from a host of gifted scientists. Camilla Middleton, Carly O. Kwiatkowski, Dr. Meesha Kaushal, and Jonathan Gillen were instrumental in the completion of chapter 2 on exciton diffusion in solution-processable metalloporphyrin thin films. Carly O. Kwiatkowski also contributed towards the completion of chapter 3 on structure-photophysics correlation in thiazolo[5,4-*d*]thiazole (TTz) crystals along with Sean Jones, P. Lane Tolley, David Diaz, Dr. Daniel S. Jones, Dr. Jessica M. Shivas, Dr. Jonathan J. Foley IV, and Dr. Thomas A. Schmedake. David Diaz, Thomas Perrell, and Isiah McPhee contributed to chapter 4 on photoactivated enhanced excimer-like emission. I sincerely thank all the aforementioned collaborators for their dedication and meaningful contributions towards the completion of this dissertation.

I especially thank my doctoral dissertation supervisor Dr. Michael G. Walter. He has spent numerous hours thinking through the problems discussed in this dissertation and editing the manuscripts presented herewith. He was extremely generous with his time, energy, and resources in helping me expand my imagination about the design and development of new advanced materials and their characterization in the light-matter interactions regime. He honed my experimental and scientific-writing skills. There was never a time when I left his office after a meeting and was not reinvigorated in my enthusiasm and excitement about research. He gave me enough space to independently try new things, fail, and then try again. He was very careful in creating a culture where I would never feel inferior for making a mistake or giving an incorrect answer. I am able to

finish this dissertation and graduate as a confident independent scientist because of his guidance. I hope I can be a generous and inspiring leader like him someday.

I would also like to thank my dissertation committee for the time and energy they have spent on my candidacy exams and final defense. I have learnt a lot about time-correlated single photon counting spectroscopy from Dr. Lauren Woods. Dr. Zhang's comments after my candidacy exam have played a significant role in the development of the narrative on the chapter on TTz crystals. Dr. Schmedake's questions have been uniquely helpful in bringing clarity to the chapter on excimers. Thank you all for readily agreeing to serve on my committee and guiding me into deeper waters of scholarly pursuit.

I also want to thank Dr. Jonathan Foley for the discussion on excimers. Meeting with him has led to a more robust explanation on the dynamics of TTz-based excimers.

I am overwhelmed with gratitude as I reflect on my time in UNC Charlotte and all the people without whom this dissertation would just not have been an enjoyable experience. Thank you to the Graduate School for the funding and all the competitions and training you organized. Thank you, Mrs. Rabinovich, for the privilege of working with you. To my fellow cohorts, 'survivors of the 2018 batch', Tyler and Venky, drinks are on me.

Cheers!

Abhishek

# DEDICATION

*To my family.*

*This victory belongs to all of us.*

# TABLE OF CONTENTS

# LIST OF FIGURES

# LIST OF ABBREVIATIONS

| | |
|---|---|
| $\eta_{\mathrm{PL}}$ | spectral overlap integral |
| $\lambda$ | wavelength |
| $\sigma_{\mathrm{A}}$ | absorption cross section |
| $A$ | donor-acceptor spectral overlap constant |
| $(\mathrm{BuOPh})_2\mathrm{TTz}$ | 2,5-Bis(4-butoxyphenyl)thiazolo[5,4-d]thiazole |
| CB | chlorobenzene |
| CIE | Commission Internationale de l´Eclairage |
| CT | charge transfer |
| $d$ | distance between two weakly coupled molecular dipoles |
| $D$ | diffusion coefficient |
| D-A-D | donor-acceptor-donor |
| DCM | dichloromethane |
| DFT | density functional theory |
| $d_{\mathrm{norm}}$ | normalized interatomic contact distance |
| $E_{\mathrm{B}}$ | binding energy |
| EHOPhTTzPy | 2-(4-(2-ethylhexyl)oxyphenyl)-5-(4-pyridyl)thiazolo[5,4-d]thiazole |
| $F_{\mathrm{D}}$ | normalized fluorescence |

| | |
|---|---|
| FRET | Förster resonance energy transfer |
| $(HepOPh)_2TTz$ | 2,5-Bis(4-heptyloxyphenyl)thiazolo[5,4-d]thiazole |
| HOMO | highest occupied molecular orbital |
| $k$ | orientation of molecular dipole PL efficiency |
| $k_B$T | product of Boltzmann constant and temperature |
| $k_F$ | rate of energy transfer |
| $L$ | sum of van der Waals effective radii |
| $L_D$ | exciton diffusion length |
| LUMO | lowest unoccupied molecular orbital |
| MALDI-TOF | matrix assisted laser desorption ionization time of flight |
| $(MeOPh)_2TTz$ | 2,5-Bis(4-methoxyphenyl)thiazolo[5,4-d]thiazole |
| NMR | nuclear magnetic resonance |
| OLED | organic light emitting diode |
| OPV | organic photovoltaic |
| PAH | polyaromatic hydrocarbon |
| *pc* | phosphor-converted |
| PL | photoluminescence |
| PLQY | photoluminescence quantum yield |

| | |
|---|---|
| PMMA | polymethylmethacrylate |
| $(PrOPh)_2TTz$ | 2,5-Bis(4-propoxyphenyl)thiazolo[5,4-d]thiazole |
| PS | polystyrene |
| rpm | rotations per minute |
| *s* | hopsize |
| SBS | styrene-butadiene-styrene |
| SC-XRD | single crystal x-ray diffraction |
| $R_o$ | radius of energy transfer |
| $TCB_4PP$ | 5,10,15,20-tetrakis[4-(butoxycarbonyl)phenyl]porphyrin |
| $TCEH_4PP$ | 5,10,15,20-tetrakis[4-((2-ethylhexyl)oxycarbonyl)phenyl]porphyrin |
| $TCH_4PP$ | 5,10,15,20-tetrakis[4-(hexyloxycarbonyl)phenyl]porphyrin |
| $TCO_4PP$ | 5,10,15,20-tetrakis[4-(octyloxycarbonyl)phenyl]porphyrin |
| TCPP | 5,10,15,20-Tetrakis(4-carboxyphenyl)porphyrin |
| THF | tetrahydrofuran |
| TLC | thin layer chromatography |
| TTz | Thiazolo[5,4-*d*]thiazole |
| UV | ultraviolet |
| Vis | visible |

| | |
|---|---|
| WLED | white-light-emitting-diodes |
| ZnTCB$_4$PP | 5,10,15,20-tetrakis[4-(butoxycarbonyl)phenyl]porphyrin |
| ZnTCEH$_4$PP | Zn-5,10,15,20-tetrakis[4-((2-ethylhexyl)oxycarbonyl)phenyl]porphyrin |
| ZnTCH$_4$PP | Zn-5,10,15,20-tetrakis[4-(hexyloxycarbonyl)phenyl]porphyrin |
| ZnTCO$_4$PP | Zn-5,10,15,20-tetrakis[4-(octyloxycarbonyl)phenyl]porphyrin |

# Chapter 1:

# Introduction

In 1941, Szent-Györgyi wrote an article that described a fundamental phenomenon which has become ubiquitous in a plethora of modern-day technologies. He began his article by describing a small molecule; a collection of atoms surrounded by a cloud of their corresponding electrons. He then wondered if research in biochemistry has been limited in its scope because of this confined imagination of excited-state energy at the quantum level. Upon reflecting on his work spanning for over two decades he says, "(it) has yielded one or another insignificant result – the isolation of this or that – but whenever I was faced with a fundamental problem, I failed." Györgyi wrote these words four years after he was awarded the Nobel Prize for the isolation of Vitamin C. With this dissertation, I join a vast cohort of scientists who have probed the "fundamental question" that Györgyi spoke about.

The problem that Györgyi was referring to was managing excited-state energy in a system which is composed of a large number of molecules. In such a system, contrary to its constituent molecules, an energy level continuum, bands, are formed along which electrons in excited-state energy can diffuse over a certain distance. The excited-state energy management in such a system is significantly different and more complex than in its molecular constituents. Controlled manipulation of excited-state energy in systems with a large number of organic molecules packed in limited degrees of freedom has been the governing principle for technologies like organic light emitting diodes (OLEDs), organic photovoltaics, printed electronics, battery technology, etc. What was once a niche field of research in physics has now attracted the attention of materials scientists, organic chemists, computational chemists, and device physicists. However, we must remember that though this understanding has sparked our imagination in the last two centuries, nature has been utilizing excited-state energy in multichromophoric systems for billions of years. Cyanobacteria, one of the first living organisms on our planet, evolved to develop a highly compact network of light harvesting antennae called thylakoids. The chlorophyll contained in the thylakoid sacs facilitated in the conversion of solar energy into chemical energy. In spite of the great technological advancements that understanding excited-state energy in multichromophoric systems has led us to, we are only neophytes in this field compared to nature.

Efficient excited-state energy, or exciton, management is crucial for a range of optical and photonic materials, coatings, and devices. Exciton management can be broadly categorized into formation, modulation, and utilization of excitons. These have been briefly discussed below.

*Exciton Formation*: When an electron is excited from HOMO to LUMO, the interstitial space (*'hole'*) it leaves behind assumes a positive charge and is coulombically bound to the excited electron. This excited electron-hole pair is called an exciton. Excitons can be broadly categorized into three types, Figure 1.1. Frenkel, Charge Transfer (CT) and Wannier-Mott.[1]

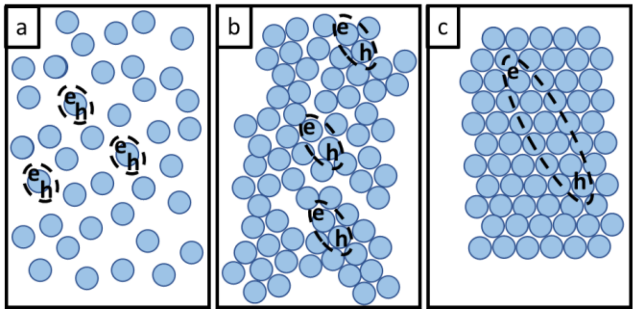

**Figure 1.1.** Types of excitons. a) Frenkel; b) Charge transfer; c) Wannier Mott

The distinct types of excitons mainly arise due to the vastly different electrical properties of materials. In organic amorphous materials, chromophores are held together by weak van der Waals interactions. These materials have a low dielectric constant and therefore, excitons remain localized over one molecule. The resultant Frenkel excitons are the most commonly generated excitons in organic materials and have small radius and high binding energy ($E_B = 0.1 – 1.0$ eV).[2, 3] CT excitons are usually generated in crystalline organic solids. They arise due to formation of $\delta^+$ and $\delta^-$ spatial charge distribution in the ordered organic solids which results in a larger radius and lower binding energy of the exciton. Frenkel and CT excitons usually coexist in organic semiconductor solids.[4] In contrast to organic materials, inorganic materials are held together by strong primary bonds and thus have a high dielectric constant. This allows charges to be effectively screened from one another. Therefore, excitons formed in inorganic materials have a large radius (40 -100 Å) and low binding energies ($E_B < 10$ meV).[5] At such low binding energies, $k_BT$ at room temperature (~ 30 meV) is sufficient to dissociate the exciton which makes inorganic crystalline solids enviable candidates for photovoltaics. These excitons are called Wannier-Mott excitons. Since Wannier-Mott excitons are formed exclusively in inorganic materials, we will focus only on Frenkel and CT excitons henceforth in this dissertation.

*Exciton Modulation*: Exciton transfer in organic materials follows mainly two processes: Förster resonance energy transfer (FRET) or Dexter energy transfer. Both processes involve non-radiative transfer of energy from a donor to an acceptor.

1. Förster resonance energy transfer (FRET): In organic semiconductors, exciton diffusion is often described by sequential Förster resonance energy transfer.[6, 7] Upon absorption of energy, an electron-hole pairs, excitons, are formed. Excitons can traverse through the energy levels of the excited system before recombining, Figure 1.2. The recombination of the electron and hole results in radiative or non-radiative photon release.

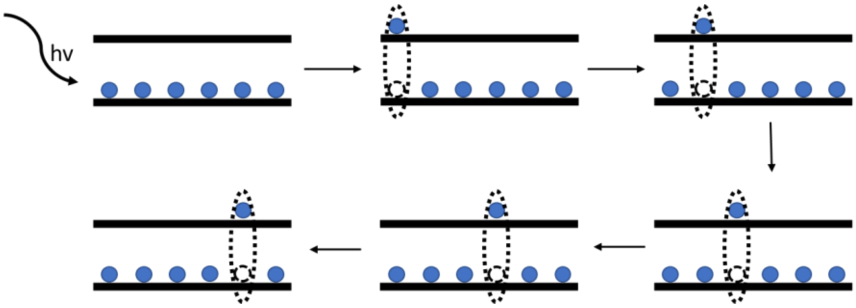

**Figure 1.2.** Schematic of exciton migration in FRET.

FRET is a long-range process with some studies reporting exciton diffusion lengths even above 100 nm.[8, 9] Förster theory indicates that rate of energy transfer ($k_F$) is a function of distance between two weakly coupled molecular dipoles ($d$) and the radius of energy transfer ($R_o$), as shown in the equations below:

$$k_F = \frac{1}{\tau}\left(\frac{Ro}{d}\right)^6,$$

$$R_o = \frac{9\eta_{PL}k^2}{128\pi^5 n^4}\int \lambda^4 F_D(\lambda)\sigma_A(\lambda)d\lambda$$

The radius of energy transfer ($R_o$) is directly proportional to the orientation of molecular dipole ($k$), PL efficiency ($\eta_{PL}$) and spectral overlap integral, where $\lambda$ is wavelength, $F_D$ is normalized fluorescence and $\sigma_A$ is the absorption cross section. Since the orientation of molecular transition dipoles and their distances play a crucial role in modulation of excitons following FRET, optimizing these parameters has become a priority in materials designed for optical and photonic applications. Among various methods that have been utilized to tune these parameters, changing their solid-state packing by method of alkylation has proven to be one of the most elegant techniques, and hence shall be discussed later.

2. Dexter energy transfer: Dexter transport requires significant wavefunction orbital overlap between the donor and the acceptor molecules and usually occurs over very short distances. Dexter transport is often seen in systems where molecules are in a state of constant collision with each other, thus resulting in an overlap of their corresponding electron clouds. Rate transfer ($k_\mathrm{D}$) for Dexter transfer follows the following relationship:

$$k_\mathrm{D} = A\exp(-\frac{2d}{L});$$

where, $A$ is a donor-acceptor spectral overlap constant and $L$ is the sum of van der Waals effective radii. As is evident from the equation, the rate of dexter transfer decays exponentially with increasing distance between the molecules.

*Exciton Utilization*: Due to spin statistics, in most optoelectronic devices, 25% of excitons formed will be singlets while 75% of excitons formed will be triplets. Therefore, a device aiming at optimum utilization of excitons should pursue to capitalize on both kinds of excitonic transitions. In OLEDs, this is done partly by manipulating the triplet excitons toward radiative recombination and minimizing deleterious pathways which would inhibit radiative singlet recombination.[10, 11] In OPVs, donor-fullerene heterojunctions are commonly used for exciton dissociation and charge collection. In these devices, semiconducting organic chromophore acts as the light absorber and generates singlet excitons. These excitons will diffuse to donor/fullerene interface where charge dissociation occurs. Therefore, the device performance is a function of exciton diffusion. It has been demonstrated previously that bi-layer solar cell efficiency can increase by 30% when exciton diffusion lengths are manipulated towards larger values.[12] There is also a recent rise in utilization of excitons for thermochromic, mechanochromic, and stimuli-responsive applications capitalizing mainly on structure-property relationship of exciton management.[13-15]

## Dissertation Summary:

Exciton management is the cornerstone of any efficient optical or photonic material. However, since excitons are electrically neutral, their modulation and utilization are a challenging task. Self-assembly of molecular materials with confined degrees of freedom has proven to be an effective method to circumvent this problem. An efficient tool to modulate self-assembly of molecular aggregates is by functionalizing them with alkyl chain appendages of varying lengths. The alkyl chains will modulate the transition dipole orientation and donor-acceptor distance. This would modulate the excitons formed and their subsequent processes like migration and recombination. The use of alkyl chains is highly innovative because alkyl chains themselves do not have a significant contribution to the electronics of the materials in question. Therefore, it is an effective tool to modulate molecular organization of chromophores in solid state and observe their excitonic characteristics.[16]

In the following chapters, I have established exciton management through self-assembly in two types of materials with immense interest in the context of optics and photonics: Metalloporphyrins and Thiazolo[5,4-*d*]thiazoles (TTzs).

In *Chapter 2*, I have studied chlorophyll-inspired Zn-metalloporphyrins which were functionalized with peripheral alkyl appendages of varying lengths. These materials were used in conjunction with a small dopant concentration of exciton quenchers to emulate the photoactive layer of a bulk-heterojunction solar cell. Since the goal of a solar cell is to successfully disassociate an exciton at the electron-acceptor nodes, long-lived and controlled diffusion of excitons is highly favorable. In this study, the exciton diffusion lengths in solution-processable thin films were established via Monte-Carlo simulations. It was found that Zn-metalloporphyrins formed highly organized domains in thin films due to their planar structure. This self-assembled organization could be tuned via alkyl chain lengths and branching. Exciton diffusion directionality with respect to the substrate could also be controlled via alkyl chain appendages. A remarkably long and rapid exciton diffusion length of 81 nm was reported. Such insights on self-assembly-directed exciton diffusion length and directionality could be highly resourceful for device engineers seeking to control excitonic diffusion in solar cells and other photonic devices.

In *Chapter 3*, symmetrically disubstituted TTz molecules with varying alkyl chain appendages were confined to form ordered organic crystals. TTz molecular materials have recently been studied in a wide range of systems for various optical and photonic applications. In this study, the solid state packing of TTz-based organic crystals was correlated with their excitonic properties. The solid state packing of crystals was established via single-crystal X-ray diffraction studies and computational simulations. The structure-energy effects of the molecules in crystals were then traced in photophysical characteristics such as absorption, emission, and lattice-phonon vibrational characteristics. The exciton dynamics were found to be highly dependent on solid-state packing in TTz-based crystals. PL emission of crystals was found to be ranging from orange-red to blue, spanning the majority of the visible electromagnetic spectrum. The correlation between structure and photophysical property of these crystals was then used to fabricate crystalline blends. These crystalline powders can be used for phosphor-converted-color-tuning and white-light-emission. The structure-property relationship in TTz crystals, along with cost-effectiveness and ease-of-synthesis, presents a compelling case for the adoption of TTz-based materials in solid-state optical and photonic devices.

In *Chapter 4*, an asymmetric TTz-based material was used to fabricate self-assembled dimers in thin films. The excitonic coupling of these dimers can be photo-controlled to yield highly stable excimer-like states. The prevailing notion regarding excimers is that they plummet the luminescence efficiency of a system. This has been challenged by a handful of reports where confining pyrene-based excimers enhanced the luminescence. In this study, we report that embedding TTz-based asymmetric dye in a neutral polymer matrix can effectively confine the excimer-like states, resulting in PL efficiency enhancement of over a factor of 2. In films with higher wt.% loading, the monomer:excimer PL intensity was found to enhance by over 8-fold. This study will be pivotal in expanding the scope of TTz-based materials and other organic luminophores for efficient luminescent optical and photonic coatings and devices based on excimer-like states.

Elucidating the dynamics of excitons in multichromophoric solid-state materials is a challenging task, one that can be approached from a variety of perspectives. In the following chapters, this problem has been approached by self-assembly of organic chromophores in compact thin films, crystals, and polymer/dye blend films. By tuning molecular-packing in confined systems exciton formation, modulation, and utilization can be controlled. This high level of control over exciton management in organic solid-state materials is pivotal for fabricating efficient optical and photonic devices.

# Chapter 2:

# Self-Assembly-Directed Exciton Diffusion in Solution-Processable Metalloporphyrin Thin Films

Adapted from *Molecules* **2022**, *27*, 35.

## 2.1 Introduction

Over billions of years of evolution, nature has optimized the process of photosynthesis through which living organisms can harvest sunlight for sustenance.[17, 18] When sunlight is absorbed by a chromophore or an array of chromophores the energy captured is transferred to reaction centers for dissociation of charges.[19, 20] This charge separation leads to storage of chemical energy which is later used for metabolic activities.[21] These photophysical processes of absorption of light, migration of energy and separation of charges have influenced the field of bio-inspired solar cell fabrication tremendously.[22-24] Persuaded by nature's efficiency, molecular engineers have been studying structural analogues of chlorophyll (porphyrins) which show attractive photophysical properties.[25-27] Porphyrins are tetrapyrrole-based aromatic macrocycles containing fully conjugated 18 π-electrons. Porphyrins have been used as linkers in metal and covalent organic frameworks and for a wide variety of applications such as photovoltaics, photocatalysis, and energy storage.[28-30] Porphyrins have also been explored for biomedical applications, photodynamic therapy, sensing and spintronics.[31-34] Despite the numerous photonic applications utilizing porphyrin materials, our understanding of energy migration in these synthetic materials is still relatively limited. Considering energy migration is a pivotal process in organic photovoltaic devices and related photonic applications, we believe a more thorough understanding of these molecular processes will lead to more efficient porphyrin-based devices.

Our earlier studies demonstrated how varying peripheral alkyl groups on free-base (alkoxycarbonyl)phenylporphyrins would affect molecular assembly and energy diffusion in solution-cast thin films.[35] We established that peripheral alkyl groups govern molecular organization and reported exciton diffusion lengths of up to 25 nm. This was one of the longest exciton diffusion lengths reported among free-base, tetraphenyl porphyrin thin films. However, in nature, porphyrins have a metal atom in the core of the macrocycle. The metal atom flattens the molecule facilitating higher excitonic coupling in the light harvesting antenna assemblies.[36] It also acts as an additional binding site for neighboring molecules yielding well-defined nanostructures, and preferential transition dipole stacking which is highly desired for excited state energy diffusion in organic thin films.[37-39] There is however an implied trade-off because the metal atom would assist in intersystem crossing of excited electrons via spin-orbit coupling, resulting in higher triplet state transitions and shortened singlet emission decay lifetime.[40] This tension makes the question of molecular organization and energy diffusion in metalloporphyrins interesting and one worth exploring.

In this study, we have synthesized (alkoxycarbonyl)phenyl zinc metalloporphyrins and developed techniques for depositing highly-uniform, solution-processable thin films. UV-Vis absorption, fluorescence spectroscopy, and X-Ray diffractometry were used to study the molecular organization in the thin porphyrin films. We found that out-of-plane ordering of transition dipoles increases with increase in linear alkyl chain length. We also determined that metalloporphyrins with branched peripheral alkyl chains assemble in-plane exclusively. The effect of peripheral alkyl groups on the photoluminescence of metalloporphyrin thin films was established by obtaining average singlet emission decay lifetimes in thin films. The thin films were doped with $C_{60}$ to determine relative fluorescence quenching efficiency. We utilized the quenching efficiency and fluorescent decay lifetimes in a Monte-Carlo simulation to establish the exciton diffusion coefficients and diffusion lengths of the metalloporphyrins in thin films. We report exciton diffusion length as high as 80.67 nm, one of the longest among similar kinds of dye molecules.[41, 42] The high transition dipole ordering and long exciton diffusion lengths in these self-assembled thin films make them highly desirable candidates for photonic and optoelectronic device fabrication.

## 2.2 Experimental

### Materials and Instrumentation

Zinc acetate dihydrate, 1-bromobutane, 1-bromohexane, 3-(bromomethyl)heptane, 1-bromooctane, chloroform ($CHCl_3$), dichloromethane ($CH_2Cl_2$), tetrahydrofuran (THF), chlorobenzene (CB) and methanol ($CH_3OH$) were purchased from Sigma-Aldrich and used without further purification. 5,10,15,20-Tetrakis(4-carboxyphenyl)porphyrin (TCPP) was purchased from TCI America and used as received. $^1H$ NMR measurements were carried out using a JEOL 300 MHz NMR and JEOL 500 MHz NMR. UV-Vis Absorption spectrometric data for solution and thin films was obtained using Cary 300 UV-Vis spectrophotometer. Solid state photoluminescence measurements were carried out on Jobin Yvon-Spex Fluorolog. PL decay lifetimes were obtained using a diode laser with repetition rate of 1 MHz and excitation wavelength 389 nm. XRD *θ/2θ* patterns were obtained using a Panalytical X'Pert Pro MPD with Ni filtered Cu K alpha radiation (λ = 1.541 Å) at 45 kV, 40 mA. The experiments were performed from 3° to 120° with 0.02° step size and a counting time of 0.35 s per point.

## Preparation of porphyrin derivatives

The following free-base 5,10,15,20-tetrakis(4-carboxyphenyl)porphyrin ($TCA_4PP$) were synthesized using previously reported synthetic methods[35]:

5,10,15,20-tetrakis[4-(butoxycarbonyl)phenyl]porphyrin ($TCB_4PP$), 5,10,15,20-tetrakis[4-(hexyloxycarbonyl)phenyl]porphyrin ($TCH_4PP$), 5,10,15,20-tetrakis[4-((2-ethylhexyl)oxycarbonyl)phenyl]porphyrin ($TCEH_4PP$) and 5,10,15,20-tetrakis[4-(octyloxycarbonyl)phenyl]porphyrin ($TCO_4PP$).

*General procedure for Zn porphyrin synthesis*

Zn-5,10,15,20-tetrakis(4-carboxyphenyl)porphyrin (Zn-$TCA_4PP$): 5,10,15,20-tetrakis(4-carboxyphenyl)porphyrin (50 mg, 0.074 mmol) was reacted with an excess of $Zn(OAc)_2 \cdot 2H_2O$ (15 mg, 0.11 mmol) in $CH_2Cl_2$:$CH_3OH$ (20 mL, 10:1) at 65 °C for 2 h in a dark environment. The reaction mixture was rinsed with Milli-Q. The product was purified by silica gel column chromatography with $CHCl_3$:$(CH_2)_4O$ (20:1) as mobile phase. Purity was confirmed with TLC, $^1$H NMR and MALDI-TOF Mass Spectrometry. Corresponding $^1$H-NMR, and MALDI-TOF mass spectra have been provided in Appendix A.

*Zn-5,10,15,20-tetrakis[4-(butoxycarbonyl)phenyl]porphyrin (Zn-TCB$_4$PP):*

Column chromatography using $CHCl_3$:$(CH_2)_4O$ (20:1) afforded 0.098 g (96%) of a slight reddish-purple solid. $^1$H NMR (300 MHz, $CDCl_3$, TMS, δ): 8.86 (s, 8H), 8.35 (d, *J* = 8.0 Hz, 8H), 8.23 (d, *J* = 8.3 Hz, 8H), 4.40 (t, *J* = 6.5 Hz, 8H), 1.83 (pnt, *J* = 7.0 Hz, 8H), 1.56 (sxt, *J* = 7.4 Hz, 8H), 1.01 (t, *J* = 7.3 Hz, 12H). UV-Vis $\lambda_{max}$ ($CHCl_3$, ε = $M^{-1}cm^{-1}$): 421 nm (ε = 935,320), 549 nm (ε = 38651), 587 nm (ε = 7558.9). MALDI-TOF (Calcd for $C_{64}H_{61}N_4O_8Zn$, $[M+H]^+$): 1077.37, found: M = 1077.10.

*Zn-5,10,15,20-tetrakis[4-(hexyloxycarbonyl)phenyl]porphyrin (Zn-TCH$_4$PP):*

Column chromatography using $CHCl_3$:$(CH_2)_4O$ (20:1) afforded 0.08 g (71%) of a slight reddish-purple solid. $^1$H NMR (300 MHz, $CDCl_3$, TMS, δ): 8.92 (s, 8H), 8.45 (d, *J* = 8.0 Hz, 8H), 8.31 (d, *J* = 8.0 Hz, 8H), 4.53 (t, *J* = 6.6 Hz, 8H), 1.92 (pnt, *J* = 7.04 Hz, 8 H), 1.59 (m, 8H), 1.43 (m, 16H), 0.96 (t, *J* = 7.0 Hz, 12H). UV-Vis $\lambda_{max}$ ($CHCl_3$, ε = $M^{-1}$ $cm^{-1}$): 421 nm (ε = 758500), 548 nm (ε = 29000), 583 nm (ε = 13000). MALDI-TOF (Calcd for $C_{72}H_{76}N_4O_8Zn$): 1188.50, found: M = 1188.06.

*Zn-5,10,15,20-tetrakis[4-((2-ethylhexyl)oxycarbonyl)phenyl]porphyrin (Zn-TCEH$_4$PP):*

Column chromatography using $CHCl_3$:$(CH_2)_4O$ (20:1) afforded 0.08 g (64%) of a slight reddish-purple solid. $^1$H NMR (300 MHz, $CDCl_3$, TMS, δ): 8.93 (s, 8H), 8.44 (d, *J* = 8.0 Hz, 8H), 8.30 (d, *J* = 8.3 Hz, 8H), 4.44 (t, *J* = 6.5 Hz, 8H), 1.87 (pnt, *J* = 7.0 Hz, 8H), 1.60 (m , *J* = 7.4 Hz, 10H), 1.43 (m , *J* = 7.4 Hz, 20H), 1.05 (t, *J* = 7.3Hz, 12H), 0.96 (t, *J* = 7.3Hz, 12H). UV-Vis $\lambda_{max}$ ($CHCl_3$, ε = $M^{-1}$ $cm^{-1}$): 426 nm (ε= 653000), 553 nm (ε = 29000), 596 nm (ε = 13000). MALDI-TOF (Calcd for $C_{80}H_{93}N_4O_8Zn$, $[M+H]^+$): 1301.62, found: M = 1303.81.

*Zn-5,10,15,20-tetrakis[4-(octyloxycarbonyl)phenyl]porphyrin (Zn-TCO$_4$PP):*

Column chromatography using $CHCl_3$:$(CH_2)_4O$ (20:1) afforded 0.08 g (66%) of a slight reddish-purple solid. $^1$H NMR (300 MHz, $CDCl_3$, TMS, δ): 8.87 (s, 8H), 8.36 (d, *J* = 8.0 Hz, 8H), 8.24 (d, *J* = 8.3 Hz, 8H), 4.42 (t, *J* = 6.5 Hz, 8H), 1.85 (pnt, *J* = 7.0 Hz, 8H), 1.43 (m , *J* = 7.4 Hz, 40H), 0.83 (t, *J* = 7.3Hz, 12H). UV-Vis $\lambda_{max}$ ($CHCl_3$, ε = $M^{-1}$ $cm^{-1}$): 421 nm (ε = 453000), 549 nm (ε = 21000), 584 nm (ε = 9000). MALDI-TOF (Calcd for $C_{80}H_{91}N_4O_8Zn$, $[M-H]^-$): 1299.62, found: M = 1299.76.

## Zn-porphyrin thin-film preparation and characterization

Glass microscope slides were sonicated with glass cleaning detergent and isopropyl alcohol. They were dried with $N_2$ gas followed by UV-ozone treatment. Zn-(Alkyloxycarbonyl)phenylporphyrin solutions of 6 mM strength were made in chlorobenzene under $N_2$ atmosphere and stirred for 24 h. Dopant solution was made by dissolving $C_{60}$ in chlorobenzene and stirred for 24 h. Prior to spin-casting, glass slides were warmed for 20 mins at 70 °C to encourage uniform film formation. The thin films were fabricated by casting the Zn porphyrin solutions at 2000 rpm for 60 s under $N_2$ atmosphere. The $C_{60}$ volume fraction (volume occupied by $C_{60}$ molecules versus blend volume) of 0.06% and 0.2% were calculated using previously reported methods.[40, 43] The Zn porphyrin densities were experimentally determined to be ~ 0.97 g $cm^{-3}$. Emission decay lifetimes of thin films were measured using a laser repetition rate of 1 MHz with excitation at 389 nm. PL(t) data was fit to triple exponential decays using Igor Pro 6.3 software. The PL decays, steady state quenching efficiencies and $v_{\mathrm{frac}}$ were used to obtain exciton diffusion coefficient and exciton diffusion length using Monte Carlo eDiffusion Software simulation.[43]

## 2.3 Results

### 2.3.1 Zn porphyrin thin-film and solution UV-Vis spectra

The UV-Vis absorption properties of Zn porphyrins in solution and thin films have been measured and compared in Figure 2.1.

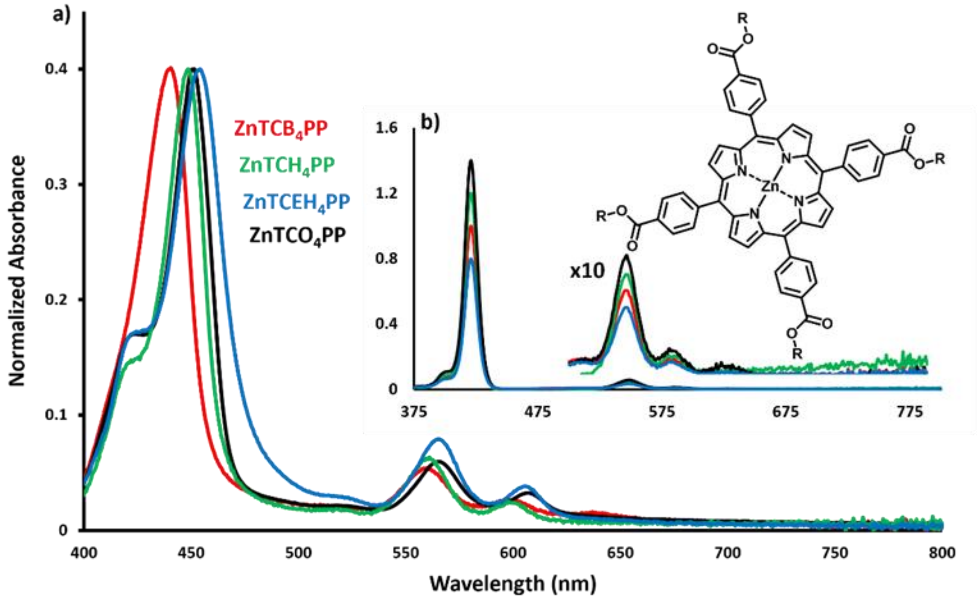

**Figure 2.1.** Normalized absorption spectra of (a) spin-cast thin films and (b) solution of butyl derivative - ZnTCB$_4$PP (-), hexyl derivative - ZnTCH$_4$PP (-), 2-ethylhexyl derivative - ZnTCEH$_4$PP (-) and octyl derivative - ZnTCO$_4$PP (-). Inset: molecular structure of Zn-5,10,15,20-tetrakis(4-carboxyphenyl)porphyrin.

In solution, the metalloporphyrins show identical absorption characteristics with a strong Soret band at 422 nm representing strong $S_0$ - $S_2$ transition. Strong presence of fourth and third Q bands can be seen at 550 nm and 588 nm respectively. Varying the alkoxycarbonyl substituents does not alter the absorption spectra of these derivatives in solution.

The spin-cast films however exhibit a distinct red shift in the absorption spectra compared to their solution spectra. $ZnTCB_4PP$ is least red shifted with the Soret band at 442 nm. Increasing the length of the peripheral alkyl chain resulted in further red shift with $ZnTCH_4PP$ and $ZnTCO_4PP$ now showing their Soret bands at 452 and 454 nm. The branched alkyl chain derivative has the most red shifted Soret band at 455 nm. $ZnTCEH_4PP$ thin film also showed the highest $S_0$ - $S_1$ with the most prominent $Q_4$ band among the four derivatives. The shifts and broadening of the Soret peaks could be attributed to various alkyl chain dependent orientations that the Zn porphyrin molecules assemble in and the resultant π-π macrocyclic interactions.[35, 44, 45] The shift in spectra suggests that the peripheral alkyl chains modulate molecular transition dipole orientation and alignment in thin films and play a strong role in the electronic transitions of these materials. We observed a red shift (~ 25 nm) in the thin films of Zn porphyrins when compared to their free-base counterparts, which is also observed in solution. The addition of the Zn (II) ion in the porphyrin macrocycle increases the planarity of the molecule, which can facilitate intermolecular stacking in thin films. These structural changes also add a higher possibility of strong excitonic coupling of transition dipoles leading to enhanced excited state energy diffusion in thin films.

The peripheral alkyl chain substituents affect the singlet emission lifetime decay as well. In Figure 2.2, singlet emission decay lifetime of solution and thin films have been presented:

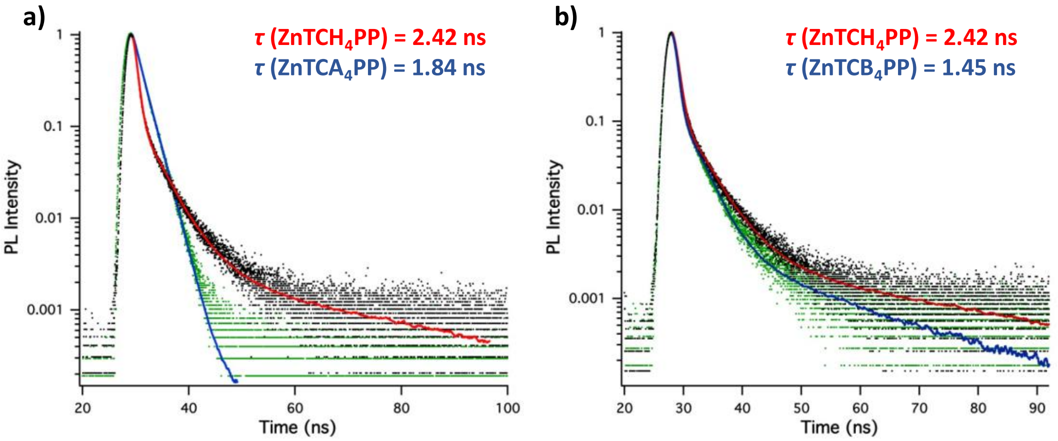

**Figure 2.2.** Singlet emission decay lifetime comparison of (a) thin film of ZnTCH$_4$PP (-) and Zn-5,10,15,20-tetrakis(4-carboxyphenyl)porphyrin solution (-) and (b) thin films of ZnTCB$_4$PP (-) and ZnTCH$_4$PP (-).

The singlet emission decay lifetime for all the metalloporphyrin derivatives in solution is 1.87 ± 0.03 ns and has a monoexponential fit, Figure S2.1. Similar to the absorption spectra, the peripheral alkyl chain substituents have no contribution to the electronic transition properties of the metalloporphyrins in solution. However, in solution-cast thin films, the emission lifetimes vary. The tri-exponential average decay lifetimes of thin films have been provided in Table 2.1. Interestingly, ZnTCH$_4$PP, ZnTCEH$_4$PP and ZnTCO$_4$PP have a longer average singlet emission decay lifetime in thin films than in solution, Figure 2.2(a). In solution, the zinc (II) ion facilitates higher triplet state transition upon interaction with the solvent molecules. Aggregation in solution could also lead to shortening of decay lifetimes. In thin films however, the alkyl chains act as molecular spacers preventing macrocyclic interactions with neighboring molecules. This could lead to longer decay lifetimes in thin films than in solution. The peripheral alkyl groups influence molecular ordering and self-assembly in thin films which affect the singlet decay lifetimes, Figure 2.2(b). In the case of linear alkyl chain substituents, the emission is short lived for smaller alkyl chains (ZnTCB$_4$PP) and increases with chain length. However, after a threshold limit, the lifetimes begin to reduce even upon the addition of further carbon atoms on the alkyl chain. ZnTCH$_4$PP has the longest decay lifetime in thin films closely followed by ZnTCO$_4$PP. The branching in the alkyl chain likely causes the molecules to assemble in an unfavorable arrangement yielding short fluorescence decay lifetimes. The singlet emission decay lifetimes for all the materials are significantly shorter than their free-base counterparts. This is due to the heavy atom effect induced by the addition of the Zn (II) ion in the macrocycle core.

### 2.3.2 Exciton diffusion coefficient (*D*) and diffusion lengths (*L*D)

In organic semiconductors, exciton diffusion is often described by sequential Förster resonance energy transfer.[6, 7] Excitons migrate randomly (diffuse) through the excited states of molecules in thin film akin to hopping. Förster theory indicates that rate of energy transfer is a function of distance between two weakly coupled molecular dipoles and the radius of energy transfer ($R_o$), as shown in the following equations:

$$k_F = \frac{1}{\tau}\left(\frac{Ro}{d}\right)^6,$$

$$R_o = \frac{9\eta_{PL}k^2}{128\pi^5 n^4}\int \lambda^4 F_D(\lambda)\sigma_A(\lambda)d\lambda.$$

The radius of energy transfer ($R_o$) is directly proportional to the orientation of molecular dipole ($k$), PL efficiency ($\eta_{PL}$) and spectral overlap integral where $\lambda$ is wavelength, $F_D$ is normalized fluorescence and $\sigma_A$ is the absorption cross section. Since molecular dipoles play a crucial role in excited state energy transfer in organic thin films, engineering their orientation and strength become a priority in materials designed for optoelectronic applications. Monte Carlo eDiffusion computational simulation was used to determine exciton diffusion coefficient and diffusion lengths in the metalloporphyrin thin films.[43] This simulation method has been used previously for similar molecules, conjugated polymers, and organic dyes.[46-50] To study steady state quenching in thin films, $C_{60}$ was doped in the metalloporphyrin solution in volume fraction 0.06% and 0.2%.[51] The diffusion model simulates a cube of edge length 25 nm and calculates the hopsize before an exciton will collide with a quencher. The model requires singlet lifetime decay, dopant volume fraction and relative quenching efficiency which is calculated as shown in the following equation for input:

$$Q = 1 - \frac{\int PL_{Blend}\, d\lambda}{\int PL_{Pristine}\, d\lambda}$$

The hopping simulation repeats with different hopsizes until it converges with the input parameters. The final resultant exciton hopsize ($s$) is then used to calculate the exciton diffusion coefficient ($D$) and exciton diffusion length ($L_D$) as shown in the following equations:

$$D = \frac{ds^2}{6dt},$$

$$L_D = \sqrt{aD\tau}.$$

Figure 2.3 depicts the photoluminescence emission spectra of pristine films and films doped with volume fraction 0.06% and 0.2% C$_{60}$ quencher molecules.

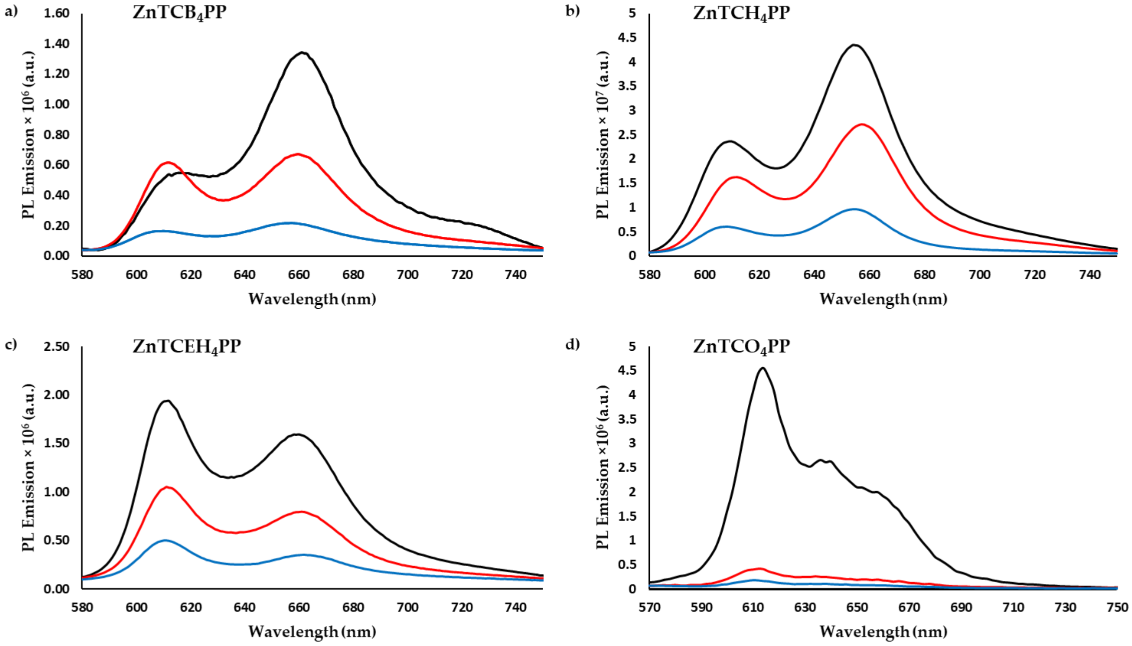

**Figure 2.3.** Photoluminescence emission spectra of spin-cast metalloporphyrins thin films of (a) butyl derivative - ZnTCB$_4$PP, (b) hexyl derivative - ZnTCH$_4$PP, (c) 2-ethylhexyl derivative - ZnTCEH$_4$PP and (d) octyl derivative - ZnTCO$_4$PP. Each plot includes spectra of pristine films (-), films doped with $v_{\text{frac}}$ 0.06% (-) and films doped with $v_{\text{frac}}$ 0.2% (-).

Doping the films with minute amounts of C$_{60}$ quenches the emission of the films since the exciton dissociates when it encounters the electron acceptor molecule at the porphyrin:C$_{60}$ interface. As the dopant concentration increases from $v_{\text{frac}}$ 0.06% to 0.2%, the emission intensity further quenches and exciton diffusion lengths shorten. This is expected as there are now more C$_{60}$ quencher molecules in the film. However, it should be noted that the addition of $C_{60}$ to the porphyrin thin film does not affect their optical absorption characteristics (Figure S2.2). Quenching efficiencies for all the derivatives are provided in Table 2.1.

**Table 2.1.** Alkylated $ZnTCA_4PP$ summary of average singlet lifetime decays ($\tau_{S1}$), relative steady state quenching efficiency ($Q$) for dopant volume fractions 0.06% and 0.2%, exciton diffusion coefficient ($D$) and diffusion length ($L_D$).

| **Material** | **$\tau_{S1}$ (ns)** | **$Q_{0.06\%}$** | **$D$ x$10^{-4}$ (cm$^2$/s)** | **$L_D$ (nm)** | **$Q_{0.2\%}$** | **$L_D$ (nm)** |
|---|---|---|---|---|---|---|
| $ZnTCB_4PP$ | 1.52 ± 0.07 | 0.37 | 1.0 ± 0.3 | 9.42 ± 1.2 | 0.77 | 8.93 ± 0.4 |
| $ZnTCH_4PP$ | 2.30 ± 0.11 | 0.37 | 0.90 ± 0.2 | 11.16 ± 1.2 | 0.78 | 9.31 ± 0.4 |
| $ZnTCEH_4PP$ | 1.88 ± 0.04 | 0.46 | 1.68 ± 0.2 | 13.74 ± 0.7 | 0.73 | 7.38 ± 0.1 |
| $ZnTCO_4PP$ | 2.02 ± 0.05 | 0.89 | 50.20 ± 4.1 | 77.98 ± 3.0 | 0.95 | 28.16 ± 0.8 |

When calculating exciton diffusion length, it is evident that exciton diffusion can be modulated by tuning peripheral alkyl substituents which influences molecular packing and transition dipole orientation in thin films. The longest exciton diffusion length is observed for $ZnTCO_4PP$ measuring at an astounding 80.67 nm. This is one of the highest exciton diffusion lengths observed in similar metalloporphyrin thin films and longer than the exciton diffusion length of its free-base counterpart by over three folds.[35] $ZnTCO_4PP$ also has exciton diffusion coefficient a one order above the other derivatives. The 2-ethylhexyl derivative ($ZnTCEH_4PP$) has an exciton diffusion length of 13 nm and exciton diffusion coefficient of 1.68 x $10^{-4}$ cm$^2$ s$^{-1}$. The butyl and hexyl derivatives have similar steady state quenching efficiency and diffusion coefficient of around 1 x $10^{-4}$ cm$^2$ s$^{-1}$. However, the highest diffusion length for $ZnTCH_4PP$ was measured at 12.26 nm compared to 9.8 nm for ZnTCB$_4$PP. This is because ZnTCH$_4$PP has a higher singlet decay lifetime. Overall, ZnTCO$_4$PP has the highest diffusion coefficient and diffusion length among the four derivatives. Even though the diffusion coefficient is comparable with some of the earlier reported studies, the diffusion length is certainly one of the highest among alkylated metalloporphyrins spin-cast thin films.[52-55]

### 2.3.3 Porphyrin thin-film XRD patterns

Additional molecular organization and thin film structural data was acquired from X-Ray diffraction studies, Figure 2.4.

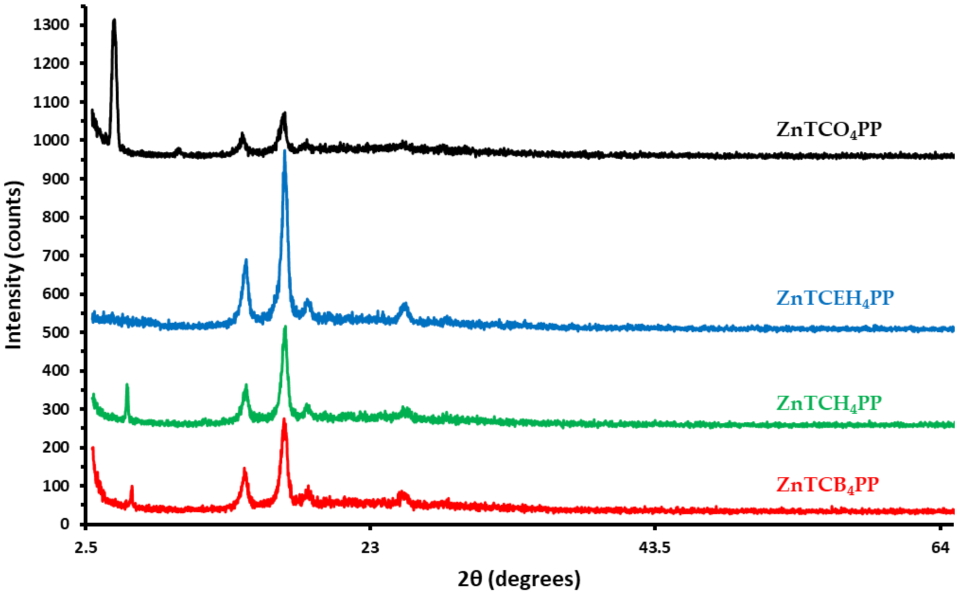

**Figure 2.4.** X-Ray diffraction patterns of solution-cast thin films of ZnTCB$_4$PP (-), ZnTCH$_4$PP (-), ZnTCEH$_4$PP (-) and ZnTCO$_4$PP (-).

The presence of multiple sharp peaks ($2\theta = 14°, 16.85°, 18.50°, 25.45°$) establishes a strong molecular ordering of metalloporphyrin thin films. The diffraction peaks appearing near *2θ* = 5.5° is indicative of out-of-plane self-assembled stacks of metalloporphyrins aligned at an angle with respect to the surface with interplanar distance measuring 15.04 Å for $ZnTCB_4PP$, 16.03 Å for $ZnTCH_4PP$ and 19.15 Å for $ZnTCO_4PP$.[54] The relative intensity of the Bragg peak at *2θ* = 5.5° with respect to the sharp peak at *2θ* = 16.85° grows dramatically with increase in length of linear peripheral alkyl chain length. The metalloporphyrin thin films appear to have higher molecular ordering than their previously reported free-base counterparts as evidenced from the high signal to noise ratio. Interestingly, $ZnTCEH_4PP$ shows an absence of out-of-plane ordering of metalloporphyrins in thin films, contrary to the free-base study. However, the in-plane *2θ* peaks are the most intense for $ZnTCEH_4PP$ among the four derivatives.

## 2.4 Discussion

UV-Vis absorption studies show that all the metalloporphyrin derivatives exhibit identical spectra in solution. The functionalization of the metalloporphyrin with peripheral alkyl groups does not alter the absorption characteristics in solution. The absence of first and second Q bands is typical with Zn porphyrins.[56, 57] When the metalloporphyrin solutions are cast to fabricate thin films, the alkyl chain length and branching influences the self-assembly of the molecules with respect to each other and to the substrate. Thus, the absorption spectra for solution-cast thin films exhibit a distinct red shift. This shift and the broadening of the Soret band is caused by the transition dipole orientation and strong excitonic coupling of the porphyrin macrocycle. $ZnTCEH_4PP$ for example, has the broadest Soret band and an amplified $Q_4$ feature. This could be indicative of strong π-π stacking and nematic ordering of the dipoles along the substrate. A shoulder in the Soret band for $ZnTCH_4PP$, $ZnTCEH_4PP$ and $ZnTCO_4PP$ is further indicative of strong excitonic coupling as seen in previous studies.[58] This was evidenced in the exciton diffusion studies with all the three derivatives having higher diffusion lengths compared to $ZnTCB_4PP$.

The metalloporphyrins have comparable, if not longer, average singlet emission decay lifetime in thin films than in solution. This interesting property likely arises due to the peripheral alkyl chain influenced self-assembly of the molecules in thin films. $ZnTCH_4PP$ exhibits the longest emission decay lifetime followed closely by $ZnTCO_4PP$. The alkyl chains behave as molecular spacers that keep the porphyrin macrocycle apart. With a small spacer, the macrocycles are assembled close to each other which quenches the singlet emission as seen in $ZnTCB_4PP$.

The exciton diffusion simulation results were comparable with previous reports.[41] $ZnTCB_4PP$ has the lowest exciton diffusion length as it has the shortest lifetime decay and low quenching efficiency. $ZnTCH_4PP$ has the longest singlet lifetime decay but did not have long exciton diffusion lengths or high diffusion coefficient due to low quenching efficiency. The decay lifetime and quenching efficiency in $ZnTCEH_4PP$ were modest and hence it has a respectable exciton diffusion length of 13 nm. $ZnTCO_4PP$ however has a remarkable diffusion coefficient and one of the highest diffusion lengths reported in the literature for similar molecules. Clearly, the nature of self-assembly of molecules in thin films has a high impact on exciton diffusion. Modulation of peripheral alkyl groups influences the transition dipole interaction and macrocyclic stacking. High exciton diffusion in $ZnTCO_4PP$, for example, could be a result of highly ordered molecular dipoles and long-range ordering of molecules. The evidence of this ordering was seen in powder X-Ray diffraction studies.

Although all derivatives exhibit high transition dipole ordering, evidenced by peaks $14° < 2\theta < 25.45°$, $ZnTCB_4PP$, $ZnTCH_4PP$ and $ZnTCO_4PP$ have strong relative intensity at peak $2\theta = 5.5°$. This confirmed that the molecules with linear peripheral alkyl chains are preferentially stacked with porphyrin edge-on alignment.[59] The preference for out-of-plane stacking increases with increase in the length of the peripheral alkyl chain length. In the case of $ZnTCO_4PP$, this kind of edge-on molecular arrangement is most dominant. The interplanar distance, Table S3.2.1, for out-of-plane arrangement increases from 15.04 Å in $ZnTCB_4PP$ to 19.15 Å in $ZnTCO_4PP$. This sharp Bragg peak is consistent with previously reported work on similar molecules.[60, 61] Absence of peak at $2\theta = 5.5°$ in case of $ZnTCEH_4PP$ suggests lack of out-of-plane crystalline arrangement of molecules perhaps caused due to the cis-trans branching in the peripheral alkyl chain.[62] This branching is likely why $ZnTCEH_4PP$ does not have strong quenching efficiency. Surprisingly, the 2-ethylhexyl free-base derivative exhibited a sharp Bragg peak at $2\theta = 5.78°$ in the earlier study.[35] The absence of a Bragg peak in the metalloporphyrin could also be a result of the addition of Zn (II) ion and the molecular shape induced effects thereof. However, it should be noted that $ZnTCEH_4PP$ has the strongest in-plane molecular ordering among the four derivatives forming a highly nematic and/or homeotropic arrangement of molecules. Similar nematic ordering is present in thin films of other linear chain derivatives as well. Identical peak intensity for $ZnTCB_4PP$ and $ZnTCH_4PP$ ($14° < 2\theta < 25.45°$) suggest both metalloporphyrins have similar tendency for in-plane molecular self-assembly. The low peak intensity in $ZnTCO_4PP$ ($14° < 2\theta <$

25.45°) reinforces the proposition that the octyl derivative highly prefers edge-on stacking over nematic/homeotropic.

The 29 nm red shift and broadening observed in UV-Vis spectra of metalloporphyrin solution versus thin films is a good indication of the formation of J-aggregates.[63] This is highly desirable for rapid and long exciton diffusion as it has been shown in the past that H-aggregation behaves as an exciton trap and is detrimental for excited state energy transfer.[64, 65] The aggregation exists in large crystalline domains with transition dipoles oriented in different angles with respect to the substrate as discussed earlier. We can observe how the self-assembly affects the directionality of exciton diffusion by comparing the two films with the most dramatic difference in angular orientation of the transition dipoles with respect to the substrate – a) octyl and b) 2-ethylhexyl derivatives (depicted in Figure 2.5).

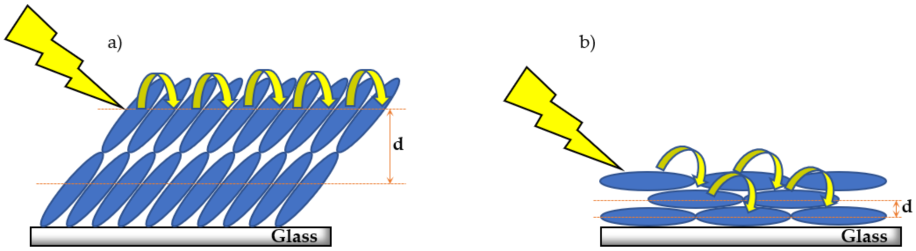

**Figure 2.5.** Proposed dominant molecular domain arrangement and exciton diffusion pathway in a) octyl derivative – $ZnTCO_4PP$ and b) *2-ethylhexyl* derivative - $ZnTCEH_4PP$ of metalloporphyrin thin films.

As mentioned earlier, the strong Bragg peak in the octyl derivative thin film indicates that the transition dipoles are assembled at a large tilt angle with respect to the substrate. Since the Bragg peak is the most dominant feature in the XRD pattern of the octyl derivative, it can be assumed that this tilted angle orientation is the largest domain in the thin films. The large tilt angle between the stack direction and substrate results in long interplanar distance and could lead to short stack height. This large distance and short stack height would make interplanar exciton hopping unlikely. However, given the strong excitonic coupling between the adjacent stack metalloporphyrin macrocycles leading to enhanced π-π interaction, it is reasonable to envision that the exciton diffusion will favor a lateral pathway. The unperturbed lateral diffusion through a well-ordered domain could be one of the reasons behind the impressive exciton diffusion lengths in the octyl derivative. In the 2-ethylhexyl derivative however, the metalloporphyrin transition dipoles are arranged parallel to the substrate. This would lead to shorter interplanar distances and higher molecular stacks. $ZnTCEH_4PP$ also boasts of high excitonic coupling indicating strong π-π macrocyclic interaction. Therefore, we propose that excitons would prefer a perpendicular diffusion pathway with respect to the substrate in these films. These insights into the directionality of exciton diffusion could be very helpful when designing the architecture of an optoelectronic device. Given that the net electrical charge of an exciton is neutral and hence their inoculation to applied potential, it is impressive that self-assembly can be used as a guiding tool to modulate the directionality of excitons in these materials.

This work demonstrates that peripheral alkyl chains and the metal atom in Zn porphyrins influences self-assembly of molecules in thin films. It is also evident from this work that the nature of molecular self-assembly in thin films play a crucial role in excited state energy diffusion. This work would be useful for molecular design and engineering aiming at optoelectronic applications where efficient/rapid exciton diffusion is desired.

## 2.5 Conclusions

We synthesized four (alkyloxycarbonyl)phenyl derivatives of Zn metalloporphyrins with varying alkyl chain lengths. It was found that the peripheral alkyl chain substituents and the Zn (II) ion in the porphyrin macrocycle influence the self-assembly arrangements of molecules in thin films. These molecular arrangements were studied using UV-Vis absorption spectroscopy and X-Ray diffractometry. The effects of these arrangements were ascertained by obtaining average singlet emission lifetime decays using Time Correlated Single Photon Counting. The thin films were doped with $C_{60}$ quencher molecules in volume fractions 0.06% and 0.2% to obtain relative quenching efficiency. The transition dipole orientation with respect to the substrate and to neighboring transition dipoles have an impact on the exciton diffusion in thin films. To establish diffusion coefficient and diffusion lengths, relative quenching efficiency, PL decay and dopant volume fraction were employed in a Monte Carlo simulation as input. The exciton diffusion lengths for $ZnTCB_4PP$, $ZnTCH_4PP$ and $ZnTCEH_4PP$ were found to be consistent with previously reported lengths in the literature. $ZnTCO_4PP$ outshone all the other derivatives with an astounding exciton diffusion length of 80.67 nm. A comparison of exciton diffusion in $ZnTCO_4PP$ and $ZnTCEH_4PP$ thin films was discussed where it was posited that excitons diffuse laterally in the octyl derivative as opposed to perpendicularly with respect to the substrate in the branched 2-ethylhexyl derivative. This work demonstrates that modulation of peripheral alkyl chain lengths and inserting a metal atom in the porphyrin macrocycle core can influence self-assembly of molecules in thin films. The resultant molecular orientation and arrangement affects the electronic, structural and photophysical properties of the materials. Molecular self-assembly can be used as a tool to modulate and direct exciton diffusion in organic thin films engineered for optoelectronic and photonic applications.

# Chapter 3:

## Correlating Structure and Photophysical Properties in Thiazolo[5,4-*d*]thiazole Crystal Derivatives for Use in Solid-State Photonic and Fluorescence-Based Optical Devices

Adapted from Mater. Adv., **2023**, *4*, 6321

### 3.1 Introduction

In the last few decades, small organic molecular dyes have proven to be pivotal for a plethora of optical and photonic applications such as organic light emitting diodes, photovoltaics, sensors, dye mediated phototherapeutics, etc.[66-75] The economies built around these technologies depend heavily on the discovery and development of new dyes for its sustained growth. For example, there is presently a strong demand for organic phosphor-converted (*pc*) white-light-emitting-diodes (*WLED*) in the solid-state lighting industry.[76-79] Ideal candidates for this application would exhibit high fluorescence, high thermal and moisture stability, inexpensive processability and should be free of rare-earth-elements. Thiazolo[5,4-*d*]thiazole (TTz) is a heterocycle moiety which exhibits all these characteristics.[80-83] TTz-based materials are inexpensive and facile to synthesize. Their strong electronegativity renders a high level of oxidative stability. They are thermally stable above 200 ºC and it is easy to functionalize these materials with a broad array of groups to modulate their photophysical properties. Due to their versatile tunability, they have been previously studied in the context of voltage sensitive dyes, solar cells, sensors, and metal-organic framework mediated photon up-conversion.[30, 84-86] However, to our knowledge, no attempts have been made to utilize TTz based materials for organic *pc-WLED* applications. This is arguably because there remains much to be understood regarding excited-state energy (exciton) management in these dyes particularly as symmetrically substituted donor-acceptor-donor (D-A-D) based materials in the solid state.

A variety of TTz-containing polymeric materials have been studied for photocatalysis, electrical conductivity, and solar cell applications showing versatile photophysical properties, strong electron withdrawing capabilities and high charge mobilities.[87-92] Exciton management in small molecule symmetrically substituted D-A-D-based TTzs has however been relatively underexplored. If small molecule symmetrically substituted D-A-D-based TTz dyes are to be integrated in photonic and optical devices on a mass scale, a thorough elucidation of their structure and photophysical properties in the solid state is required. This is a challenging task since aggregation-caused-quenching-effects and many-body-effect complicate the study of exciton dynamics and structure – photophysical property relationships in solid-state materials.[93] Although few groups have reported on this relationship in the past utilizing D-A-D TTzs, a methodical study with a high degree of control over this correlation is yet to be established.[94, 95] To address this gap of knowledge of exciton management in solid-state symmetrically substituted D-A-D TTzs, we strategically synthesized four symmetrically substituted TTz-based materials functionalized with alkyl appendages of varying lengths. Since photophysical properties, such as singlet radiative recombination rates in the solid state, is a function of neighboring transition dipole orientation and distance, it was crucial to resolve the packing in crystals.[96] We have addressed three questions: 1) Will variations in alkyl chain lengths modulate molecular packing in TTz-based crystals? 2) Will modulation of molecular packing influence photophysical properties like exciton recombination lifetime and photoluminescence emission? 3) Can these crystals be utilized for color-tuning and *pc*-white-light emission applications in the solid state? Herein, we report their crystal structures, molecular packing, steady state, and time-resolved photophysical properties. We have also studied crystalline blends of these materials for color-tunability in phosphor-converted light emission applications. Lastly, we report white-light emissive crystalline mixtures utilizing alkoxyphenyl TTz blends.

## 3.2 Experimental

### Materials and Instrumentation

4-n-Alkyloxybenzaldehyde and dithiooxamide were purchased from Sigma-Aldrich and used without further purification. Chloroform ($CHCl_3$), dichloromethane (DCM), pentane, and hexanes were purchased from Alfa Aesar Chemicals and used without further purification. $^1$H-NMR measurements were carried out using JEOL 500-MHz NMR. Mass spectrometry measurements were obtained using a Perceptive Biosystems Voyager MALDI mass spectrometer. UV-Vis absorption spectrometric data for solution was obtained using Cary 300 UV-Vis spectrophotometer. Diffuse reflectance measurements of the crystals were collected using Cary 5000 UV-Vis spectrophotometer. Photoluminescence measurements were carried out on Jobin Yvon-Spex Fluorolog. PL decay lifetimes were obtained using a diode laser with a repetition rate of 1 MHz and excitation wavelengths of 389 nm. 9,10-Diphenylanthracene in cyclohexane was used as standard reference for quantum yield measurements.[97] Solid state quantum yield measurements were carried out using QuantiPhi-2. Density functional theory (DFT) computational analysis was performed using *Spartan '10* and *CrystalExplorer17*, at B3LYP/6-31G(D) and B3LYP/6-31G(d,p) level, respectively. The samples used for micro-Raman experiments were chosen with the aid of an optical microscope (Olympus BX41) interfaced to a Jobin Yvon XploRA PLUS Raman spectrometer, spanning the region 10−1800 $\text{cm}^{-1}$. Excitation wavelength of 785 nm was chosen to avoid fluorescence. Neutral density optical filters were used to minimize the risk of crystal damage. Powder XRD $\theta/2\theta$ patterns were obtained using 'Xcalibur - Gemini ultra' with Ni filtered Cu K$\alpha$ radiation ($\lambda$ = 1.541 Å) at 50 kV, 40 mA. The experiments were performed from 0° to 123.82° with 0.01 step size and a counting time of 1 s per point.

Single crystal X-ray diffractometry data were acquired with an Agilent (now Rigaku) Gemini A Ultra diffractometer. Single crystals of $(MeOPh)_2TTz$ were obtained and isolated after rinsing the reaction product repeatedly with ethanol and deionized water. The crystal structure was compared with previously reported literature and found to be consistent.[98] Single crystals of $(PrOPh)_2TTz$, and $(HepOPh)_2TTz$ were grown via solvent-vapor diffusion technique with hexanes and chloroform. Single crystals of $(BuOPh)_2TTz$ were grown using solvent-liquid-liquid-diffusion method with hexanes and chloroform. Single crystals of suitable size were coated with a thin layer of paratone-N oil, mounted on the diffractometer, and flash cooled to 100 K in the cold stream of the Cryojet XL liquid S55 nitrogen cooling device (Oxford Instruments). The diffractometer was equipped with sealed-tube long fine focus X-ray sources with Mo target ($\lambda$ = 0.71073 Å) and Cu target ($\lambda$ = 1.5418 Å), four-circle kappa goniometer, and CCD detector. Mo target was used to characterize $(MeOPh)_2TTz$. Cu target was used for $(PrOPh)_2TTz$,

$(BuOPh)_2TTz$, and $(HepOPh)_2TTz$ crystals. CrysAlisPro9 software was used to control the diffractometer and perform data reduction. The crystal structure was solved with SHELXS.[99] All non-hydrogen atoms appeared in the E-map of the correct solution. Alternate cycles of model-building in Olex2 and refinement in SHELXL followed.[99, 100] All non-hydrogen atoms were refined anisotropically. All hydrogen atom positions were calculated based on idealized geometry and recalculated after each cycle of least squares. During refinement, hydrogen atom – parent atom vectors were held fixed (riding motion constraint).

**Preparation of Dialkoxyphenyl TTz derivatives**

4-n-Alkyloxybenzaldyde was reacted with dithiooxamide in 10 mL of DMF for 24 h at 150 °C. The resulting precipitate was collected by filtration and rinsed with water and ethanol. The product was purified using silica gel column chromatography, and purity and structure were established using TLC, $^1H$-NMR, and MALDI-TOF mass spectrometry. Corresponding $^1H$-NMR, and MALDI-TOF mass spectra have been provided in Appendix B.

*2,5-Bis(4-methoxyphenyl)thiazolo[5,4-d]thiazole ($(MeOPh)_2TTz$):*

The precipitate mixture was rinsed with ethanol and water repeatedly to yield 0.25 g (61.5%) of orange-red fluorescent needle-like crystals. $^1H$-NMR (500 MHz, $CDCl_3$, TMS, δ): 7.93 (d, $J = 1.98$ Hz, 2H), 6.99 (d, $J = 2.01$ Hz, 2H), 3.88 (s, 3H). UV-Vis $\lambda_{max}$ ($CHCl_3$, $\varepsilon = M^{-1}cm^{-1}$): 375 nm ($\varepsilon = 27816$). MALDI-TOF-MS (Calcd for $C_{18}H_{14}N_2O_2S_2$):

354.44, found: M = 354.66. Quantum yield in $CHCl_3$ ($\lambda_{ex}$ = 375 nm, $\lambda_{em}$ = 375 nm, $\lambda_{em}$ = 435 nm) = 28%.

*2,5-Bis(4-propoxyphenyl)thiazolo[5,4-d]thiazole ((PrOPh)$_2$TTz):*

Column chromatography using hexanes:DCM (1:1) afforded 0.45 g (47%) of product. $^1$H-NMR (500 MHz, $CDCl_3$, TMS, δ): 7.92 (d, *J* = 1.98 Hz, 2H), 6.97 (d, *J* = 1.99 Hz, 2H), 3.99 (t, *J* = 2 Hz, 2H), 1.84 (m, 2H), 1.06 (t, *J* = 2.86 Hz, 3H). UV-Vis $\lambda_{max}$ ($CHCl_3$, ε = $M^{-1}cm^{-1}$): 375 nm (ε = 70183). MALDI-TOF-MS (Calcd for $C_{22}H_{22}N_2O_2S_2$, $[M+H]^+$): 411.11, found: M = 411.06. Quantum yield in $CHCl_3$ ($\lambda_{ex}$ = 370 nm, $\lambda_{em}$ = 437 nm) = 28%.

*2,5-Bis(4-butoxyphenyl)thiazolo[5,4-d]thiazole ((BuOPh)$_2$TTz):*

Column chromatography using pentane:DCM (2:1) afforded 0.11 g (45%) of product. $^1$H-NMR (500 MHz, $CDCl_3$, TMS, δ): 7.92 (d, *J* = 2 Hz, 2H), 6.98 (d, *J* = 2.04 Hz, 2H), 4.03 (t, *J* = 2 Hz, 2H), 1.80 (m, 2H), 1.52 (m, 2H), 0.99 (t, *J* = 3 Hz, 3H). UV-Vis $\lambda_{max}$ ($CHCl_3$, ε = $M^{-1}cm^{-1}$): 375 nm (ε = 2000000). MALDI-TOF-MS (Calcd for $C_{24}H_{26}N_2O_2S_2$, $[M+H]^+$): 439.14, found: M = 439.04. Quantum yield in $CHCl_3$ ($\lambda_{ex}$ = 375 nm, $\lambda_{em}$ = 437 nm) = 28%.

*2,5-Bis(4-heptyloxyphenyl)thiazolo[5,4-d]thiazole ((HepOPh)$_2$TTz):*

Column chromatography using hexanes:$CHCl_3$ (0.5:4.5) afforded 0.20 g (55%) of product. $^1$H-NMR (500 MHz, $CDCl_3$, TMS, δ): 7.93 (d, *J* = 1.96 Hz, 2H), 6.98 (d, *J* = 2 Hz, 2H), 4.02 (t, *J* = 2 Hz, 2H), 1.81 (quint, *J* = 2.17 Hz, 2H), 1.47 (m, 2H), 1.30 (m, 6H), 0.90 (t, *J* = 3.21 Hz, 3H). UV-Vis $\lambda_{max}$ ($CHCl_3$, ε = $M^{-1}cm^{-1}$): 375 nm (ε = 46926).

MALDI-TOF-MS (Calcd for $C_{30}H_{38}N_2O_2S_2$, $[M+H]^+$): 523.24, found: M = 523.00. Quantum yield in $CHCl_3$ ($\lambda_{ex}$ = 373 nm, $\lambda_{em}$ = 437 nm) = 25%.

## Preparation of Crystalline Films

Two sets of symmetrically substituted D-A-D TTz polycrystalline blends were studied for color tuning and all-organic white light emission. The materials were chosen for a wide fluorescence tuning window and discernable PL emission signal. The mixtures were drop casted on pre-cleaned glass substrates the solvent was allowed to evaporate at room temperature.

*Set 1: $(MeOPh)_2TTz$ and $(PrOPh)_2TTz$*

$(MeOPh)_2TTz$ was dispersed in ethanol and sonicated for 1 h to maximize the yellow emission originating from surface defects. 0.1 mg aliquots of the dispersion were dispensed in test tubes. $(PrOPh)_2TTz$ was dissolved in dichloromethane and added to the EtOH $(MeOPh)_2TTz$ suspension in varying weight proportions.

*Set 2: $(MeOPh)_2TTz$ and $(BuOPh)_2TTz$*

$(MeOPh)_2TTz$ and $(BuOPh)_2TTz$ stock solutions were prepared in dichloromethane. To 0.1 mg of $(MeOPh)_2TTz$, varying weight ratios of $(BuOPh)_2TTz$ were added and drop casted on glass substrates.

## Computing CIE Chromaticity Coordinate

The emission of the TTz dyes was characterized by their location on a 2D color space known as chromaticity diagram. The chromaticity diagram is defined by the $\mathbf{x}, \mathbf{y}$ coordinates defined as

$$\mathbf{x} = \frac{\mathbf{X}}{\mathbf{X}+\mathbf{Y}+\mathbf{Z}} \qquad \mathbf{y} = \frac{\mathbf{Y}}{\mathbf{X}+\mathbf{Y}+\mathbf{Z}}$$

where the $\mathbf{X}, \mathbf{Y}, \mathbf{and}\ \mathbf{Z}$ are computed by integrating the product of the emission spectrum of the dye and the appropriate color matching function over visible wavelengths:

$$\mathbf{X} = \int_{\boldsymbol{\lambda}_1}^{\boldsymbol{\lambda}_2} \mathbf{I}(\boldsymbol{\lambda})\ \bar{\mathbf{x}}(\boldsymbol{\lambda})\mathbf{d}\boldsymbol{\lambda}$$

$$\mathbf{Y} = \int_{\boldsymbol{\lambda}_1}^{\boldsymbol{\lambda}_2} \mathbf{I}(\boldsymbol{\lambda})\ \bar{\mathbf{y}}(\boldsymbol{\lambda})\mathbf{d}\boldsymbol{\lambda}$$

$$\mathbf{Z} = \int_{\boldsymbol{\lambda}_1}^{\boldsymbol{\lambda}_2} \mathbf{I}(\boldsymbol{\lambda})\ \bar{\mathbf{z}}(\boldsymbol{\lambda})\mathbf{d}\boldsymbol{\lambda}$$

Where, $\mathbf{I}(\boldsymbol{\lambda})$ denotes the emission spectrum of the dye, $\bar{\mathbf{x}}(\boldsymbol{\lambda}), \bar{\mathbf{y}}(\boldsymbol{\lambda}), \bar{\mathbf{z}}(\boldsymbol{\lambda})$ are the CIE 1931 standard color matching functions, and the integration limits span visible wavelengths, i.e. $\boldsymbol{\lambda}_1 = \mathbf{380\ nm}$ and $\boldsymbol{\lambda}_2 = \mathbf{780\ nm}$.[101] We utilize the WPTherml software package[102] to parse the experimental emission spectra and compute the CIE (x,y) coordinates through Eq. (1) and (2), and the colour[103] software package to render the CIE (x,y) coordinates as colors on the standard CIE chromaticity diagram and color gamut.

### 3.3 Results and Discussion

To study exciton management in D-A-D solid-state TTz-based materials, we functionalized the TTz core with symmetric para-substituted dialkoxyphenyl groups with varying alkyl chain lengths (Figure 3.1).

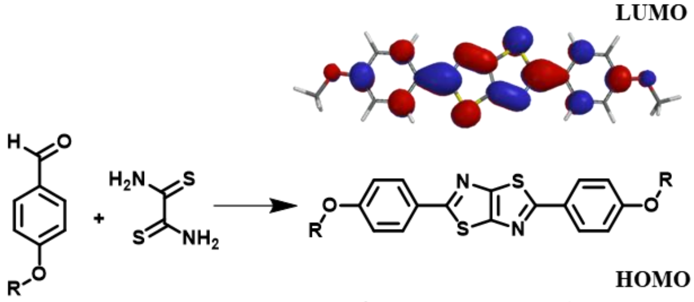

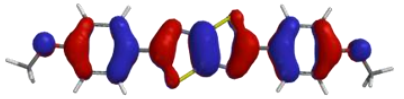

| Alkyl Group | Label |
|---|---|
| Methyl<br>-$CH_3$ | $(MeOPh)_2TTz$ |
| n-Propyl<br>-$(CH_2)_2CH_3$ | $(PrOPh)_2TTz$ |
| n-Butyl<br>-$(CH_2)_3CH_3$ | $(BuOPh)_2TTz$ |
| n-Heptyl<br>-$(CH_2)_6CH_3$ | $(HepOPh)_2TTz$ |

**Figure 3.1.** Schematic for the synthesis of Dialkoxyphenyl thiazolo[5,4-*d*]thiazole is shown above along with electrostatic potential maps of ground state (HOMO) and first singlet excited state (LUMO) emphasizing the D-A-D character.

The π conjugation of the electron acceptor TTz central heterocycle moiety is further extended by the phenyl groups on either side. This extended conjugated backbone broadens the ensemble of excited states into a quasi-continuous 'band' leading to increased probability density of excitons diffused over individual chromophores. This extended excited state band will influence excitonic coupling with neighboring molecules in condensed matter states via non-covalent intermolecular interactions.[93] Alkoxy appendages would serve as electron donor groups (Figure 3.1). Alkyl appendages of varying lengths are remarkable candidates for use as donor groups to explore exciton manipulation.[16, 35, 104-106] Variation in their lengths has negligible effect on the electronics of the molecule. However, they have been previously shown to influence intermolecular packing in the solid state.[14, 15, 107, 108] This unique property of alkyl groups makes them highly suitable electron donors when establishing excitonic characteristics of a central organic moiety in solid-state materials.

## 3.3.1 Structural Studies

### *3.3.1.1 Single Crystal XRD Studies*

Single crystals of $(MeOPh)_2TTz$ were obtained and isolated after rinsing the reaction product repeatedly with ethanol and water. The crystal structure was compared with previously reported literature and found to be consistent.[98] We report crystallographic data for single crystals of $(PrOPh)_2TTz$, $(BuOPh)_2TTz$, and $(HepOPh)_2TTz$ for the first time. Single crystals of $(PrOPh)_2TTz$, and $(HepOPh)_2TTz$ were grown through solvent-vapor diffusion technique with hexanes and chloroform. Single crystals of $(BuOPh)_2TTz$ were grown via solvent-liquid-liquid-diffusion method with hexanes and chloroform. The crystals were characterized using single crystal X-ray diffraction to obtain the molecular packing in these materials. The crystal parameters are summarized in Table S3.1. Significant alkyl chain dependent variations were observed in the packing of these crystals. These variations could strongly influence excitonic behavior in these materials.

The crystals packed in either monoclinic ($P2_1/c$) or triclinic ($P\bar{1}$) unit cell. Interestingly, the crystals that packed in monoclinic type showed a perfect correlation between volume of unit cell and alkyl chain length, (Figure S3.2). Crystallographic data reveals high degree of planarity in all molecules except in the case of $(PrOPh)_2TTz$ where the final carbon atom on the alkyl appendage is turned 113° out of the TTz plane following a trans conformation.

#### *3.3.1.2 Crystal Packing Motifs*

Intermolecular interactions and arrangements typically drive energy fluxes and consequently, photophysical properties of bulk organic crystals. Therefore, insights into crystal packing motifs are useful predictors of excitonic behavior in organic solid-state materials.[109, 110] Figure 3.2 contains the unit cell molecular packing diagram of the four TTz crystal derivatives tilted along *c* axis.

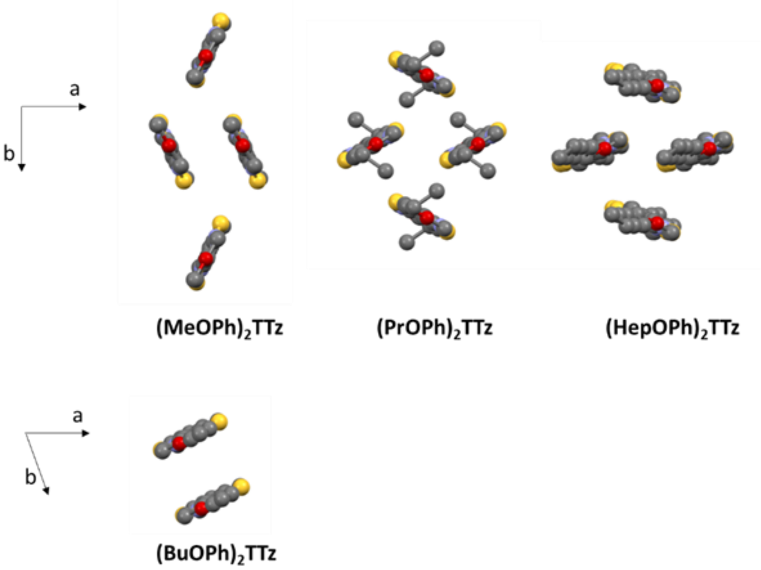

$(MeOPh)_2TTz$ $(PrOPh)_2TTz$ $(HepOPh)_2TTz$

$(BuOPh)_2TTz$

**Figure 3.2.** Crystal packing diagram of $(C_nOPh)_2TTz$ unit cell. Top panel: Herringbone packing mode series; Bottom panel: slipped stack packing mode. H atoms are omitted for clarity.

$(MeOPh)_2TTz$, $(PrOPh)_2TTz$, and $(HepOPh)_2TTz$ arranged in herringbone pattern while $(BuOPh)_2TTz$ arranged in slipped stacks. SC-XRD packing data was used in conjunction with *CrystalExplorer17* software package at B3LYP/6-31G(d,p) level to aid in establishing which intermolecular interactions would influence energy flux in the TTz crystals.[111] Figure S3.3 depicts color-coded geometry-based pictorial representation of interaction energies in TTz crystals with respect to one central reference molecule. Details of these interaction energies have been enumerated in Table S3.2. Based on the experimental and modeling data, molecular pairs of distinct geometric arrangements were extrapolated and have been shown in Figure 3.3 with emphasis on the intermolecular interactions.

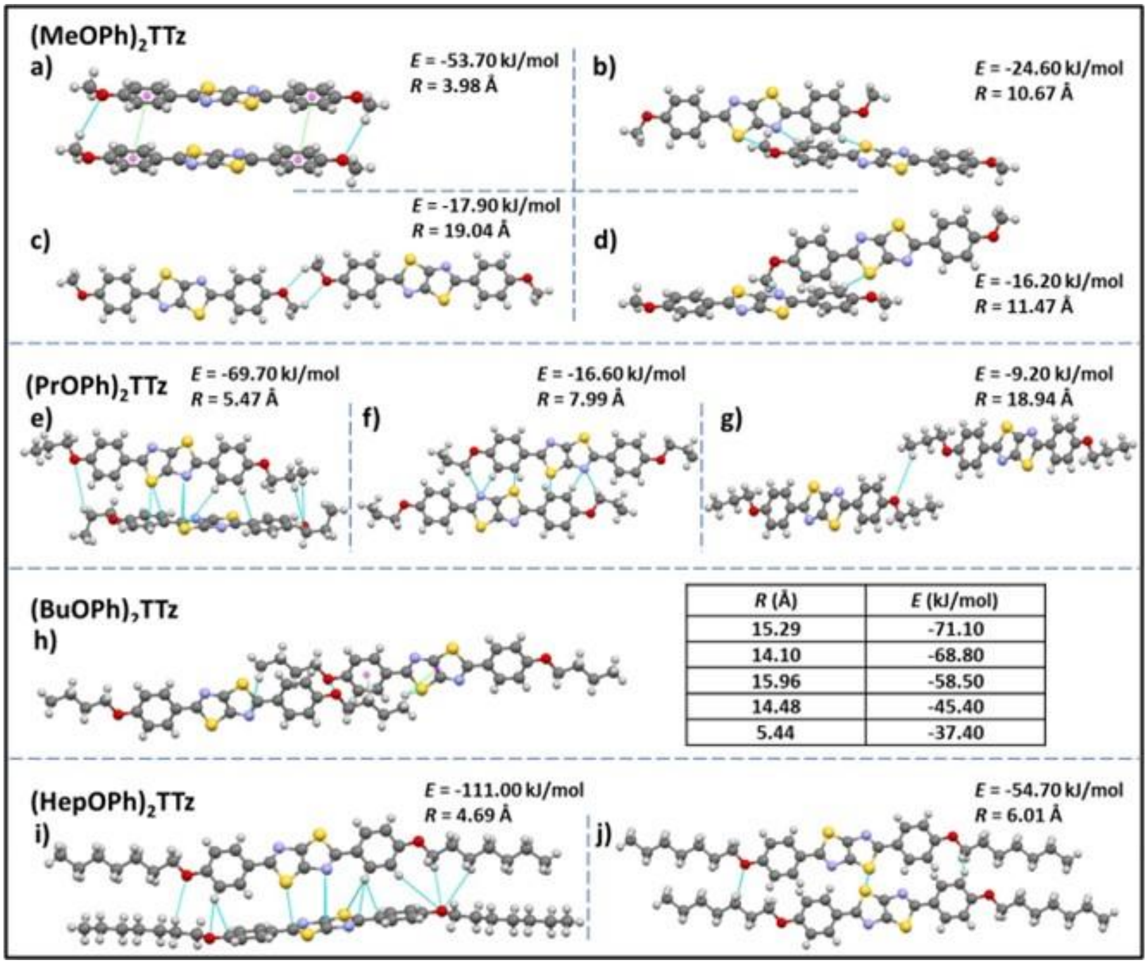

| $R$ (Å) | $E$ (kJ/mol) |
|---|---|
| 15.29 | -71.10 |
| 14.10 | -68.80 |
| 15.96 | -58.50 |
| 14.48 | -45.40 |
| 5.44 | -37.40 |

**Figure 3.3.** Unique intermolecular non-covalent interactions and orientation among ($C_nOPh)_2$TTz extrapolated from crystal packing and modeling studies. *E* is the total energy of interaction among the molecular pairs. The distance between molecular centroids is denoted by *R*. (*cf* Table S3.2, Table S3.3, and Figure S3.3)

All the intermolecular interactions from crystal packing studies have been enumerated and discussed further in Table S3.3. In the case of (MeOPh)$_2$TTz four unique molecular orientations can be observed. The cofacial arrangements (Figure 3.3a, c) have close C-H—O interactions at 2.9 and 2.5 Å, respectively. In Figure 3a, the molecules align similar to an H-type aggregate with a slipping angle of 101.93°. The TTz cores and phenyl rings stack on top of each other in this arrangement. The centroids of the phenyl rings are 3.9 Å apart. The π-π stacking arrangement could be the reason why this pair has the highest total energy of interactions in this crystal (-53.70 kJ/mol) with the highest contribution from dispersion energy component. There are two orthogonal arrangements in the $(MeOPh)_2TTz$ crystal, (Figure 3b, d). In both these arrangements, the alkyl chain and phenyl ring interact with the π conjugated TTz core. In $(PrOPh)_2TTz$ crystal, molecules arrange in three conformations. Among these, the orthogonal orientation (Figure 3e) has the highest number of possible interactions with contacts distributed throughout the molecule. This arrangement also has the highest number of pairs ($N = 4$), and the highest energy of interactions (-69.70 kJ/mol) in this crystal. Most of these contacts are interacting with the TTz core. One of the two cofacial arrangements (Figure 3f) has multiple interactions with the TTz core as well. Also, among the orthogonal (Figure 3e) and cofacial (Figure 3g) arrangements there are multiple C-H—O interactions present. In the case of $(BuOPh)_2TTz$ crystal, the alkyl appendages are responsible for all the interactions. The molecules arrange in J-type cofacial slipped stacks, Figure 3h, with C-H—(O, N, S, $\pi_{\text{phenyl centroid}}$, and $TTz_{\text{centroid}}$) interactions. The proximity of the molecules and the uniform cofacial arrangement results in very similar total energy of interactions among the pairs (-37.40 to -71.10 kJ/mol) with the highest contribution from the dispersion energy. In $(HepOPh)_2TTz$ crystal, the orthogonal arrangement (Figure 3i) is the most stable pair among all the molecular pairs depicted in Figure 3 with total energy of interactions at -111 kJ/mol. This could be because there are multiple interaction sites throughout the molecule pair. $(HepOPh)_2TTz$ also has a cofacial pair with C-H—O and S—S interaction.

It is not enough to establish all the non-covalent intermolecular contacts in a crystal. Intermolecular interactions are inherently competitive. Since the aim of this study is to establish structure-property relationship in TTz crystals, it is important to ascertain which interactions would dominate the crystal packing. To address this problem, we simulated Hirshfeld surfaces of the molecules in the crystal unit cell. Hirshfeld surface simulations quantifies the intermolecular atomic contacts in the crystal using the descriptor $d_{\mathrm{norm}}$. The normalized interatomic contact distance ($d_{\mathrm{norm}}$) accounts for contact distances between nearest atoms present inside ($d_{\mathrm{i}}$) and outside ($d_{\mathrm{e}}$) the simulated surface and is expressed using the following equation.

$$\boldsymbol{d_{norm}} = \frac{\boldsymbol{d_i - r_i^{vdW}}}{\boldsymbol{r_i^{vdW}}} + \frac{\boldsymbol{d_e - r_e^{vdW}}}{\boldsymbol{r_e^{vdW}}}$$

Here, $\boldsymbol{r_i^{vdW}}$ and $\boldsymbol{r_e^{vdW}}$ represent the van der Waals radii of the atoms internal and external to the surface, respectively. The Hirshfeld surface simulations rendered $d_{\mathrm{norm}}$ images with fixed color scale of -0.0955 (red) to 1.1742 (blue), shown in Figure 3.4. The images utilized a red-white-blue color scheme where red highlights the shorter contacts, white is used for interactions around the vdW separation distance, and blue is for longer contact distances. The red spots become brighter and bigger as the internuclear distances decrease.

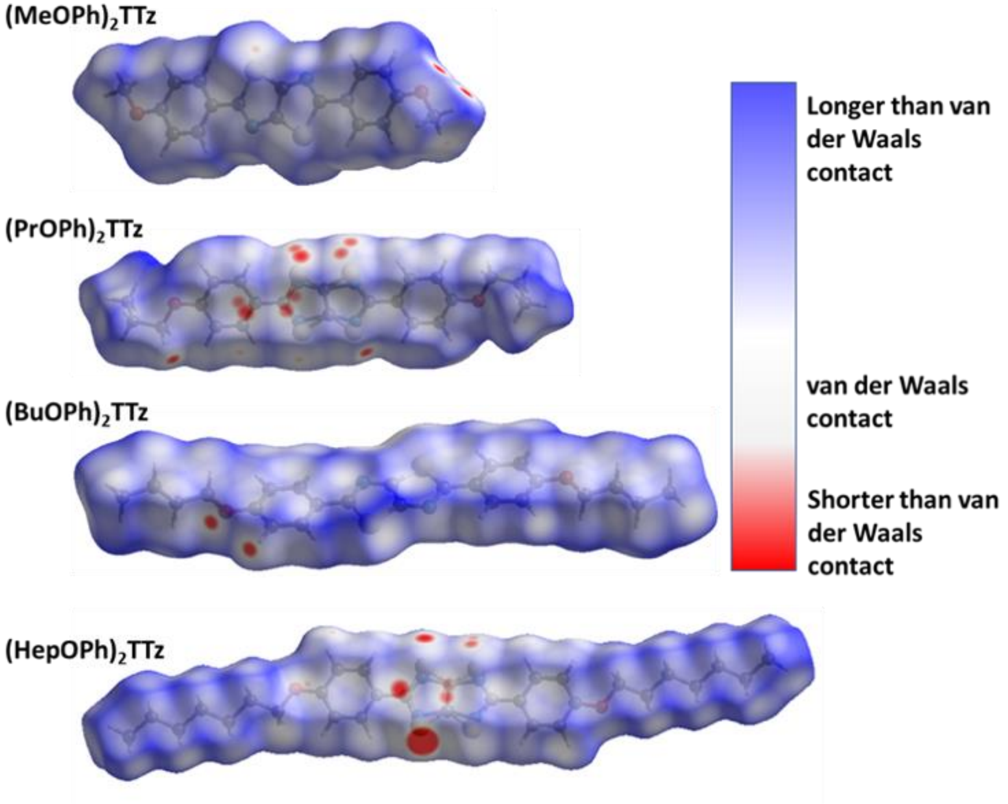

**Figure 3.4.** Normalized $d_{\mathrm{norm}}$ mapping images of the Hirshfeld surface analysis of the TTz crystals.

All the types and distribution of relative contributions of intermolecular contacts to the Hirshfeld surface area for the $(C_nOPh)_2TTz$ crystals have been provided in Figure S3.5. In Figure 4.4a, significant interaction sites near the alkyl appendage and the oxygen atom of the $(MeOPh)_2TTz$ molecule is observed. These sites represent the C-H—O bonding which was depicted in the cofacially arranged molecules in Figure 3.3a, c. There is also a faint interaction site visible at the TTz core. This interaction is caused by the orthogonal arrangements in the crystal. In the case of $(PrOPh)_2TTz$, many interaction sites are visible. Most of these sites are localized around the TTz core and phenyl rings indicating that the π conjugated backbone of the molecule is well connected with other molecules within the crystal. The most dominant interaction in $(BuOPh)_2TTz$ is the C-H—O contact. This interaction is established between the phenyl ring and oxygen atom of neighboring molecules. The TTz core of $(HepOPh)_2TTz$ molecule is strongly interacting with the orthogonal and cofacial molecules. The big red spot on the TTz core is indicative of the many sulfur-based contacts in this crystal.

A salient packing-dependent feature of organic solid-state materials that influences photophysical and excitonic properties is π-π stacking. The *Shape Index* feature of Hirshfeld surfaces was utilized to ascertain the presence of π-π stacking in the $(C_nOPh)_2TTz$ crystals. The results are shown in Figure S3.6. $(MeOPh)_2TTz$ crystals show evidence for π-π stacking around the phenyl rings. The stacking is caused because the phenyl centroids of cofacial $(MeOPh)_2TTz$ molecules interact with each other in a crystal environment. It must be noted that $(MeOPh)_2TTz$ was the only crystal among the four TTz derivatives in this study that exhibited pronounced π-π stacking. $(BuOPh)_2TTz$ exhibited signs of stacking along the alkyl chain. These were caused by C-H—π interactions.

Based on the single-crystal X-ray diffraction experiments and computational modeling, we can arrive at the following conclusions about the crystal packing of $(C_nOPh)_2TTz$ crystals and excitonic property predictions. The cofacial molecular pair in $(MeOPh)_2TTz$ crystal is the most stable intermolecular configuration in this crystal with high dispersion energy. This pair also has significant π-π stacking which could lead to exciton formation diffused over multiple molecules. Such geometry-energy related effects could result in significantly red-shifted PL emission spectra and long singlet lifetimes.[105] The π conjugated backbone of $(PrOPh)_2TTz$ is well connected to other molecules in the crystal. The most stable of these interactions are with orthogonally oriented molecules. This could lead to a broad PL emission spectrum and release of low energy photons. The $(BuOPh)_2TTz$ arranged in J-type cofacial slipped stacks with most interactions limited to the alkoxy appendages. The similar total energy of interactions among the molecular pairs along with the high contribution from dispersion energy component indicates to the possibility of exciton delocalization over multiple molecules and relaxation of excited energy via non-radiative pathways. Therefore, it can be predicted that the PL emission spectral shape and singlet radiative recombination rates of $(BuOPh)_2TTz$ crystal would resemble its solution counterpart while non-radiative pathways could lead to loss of luminescence efficiency. The TTz core of $(HepOPh)_2TTz$ is connected through multiple contacts with neighboring orthogonally oriented molecules. These interactions have the highest total energy among the four TTz crystal derivatives and thus would play the dominant role in excitonic properties of this crystal. The orthogonal orientation would result in a broad ensemble of excited state bands which could encourage exciton delocalization. Such delocalization could result in long exciton lifetimes, broad PL emission profile, and release of low energy photons. Crystallographic studies thus conclusively prove that small variations in alkyl chain length, a rather understated donor group, leads to a wide range of modulation in molecular packing in TTz-based crystals.

### 3.3.2. Photophysical Studies

#### *3.3.2.1 Steady State Photophysical Studies*

In solution state, the alkyl appendages have no effect on the photophysical properties of the TTz derivatives (Inset Figure 3.5). Also, all the derivatives exhibit approximately the same quantum yield in solution state as well ($\Phi_F$ = 25-28%). This is expected since the length of the alkyl chains have negligible contribution to the intrinsic electronic properties of the molecule. However, in the solid state, the alkyl chains strongly modulate the photophysical properties of these derivatives. Figure 3.5 shows the absorption and PL emission characteristics of the crystal derivatives.

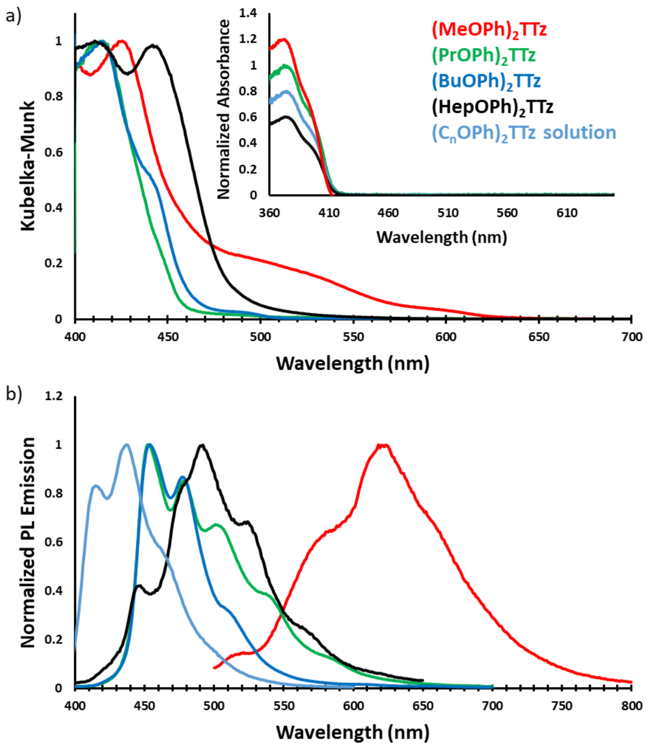

**Figure 3.5.** Steady state photophysical characteristics of symmetrically substituted dialkoxyphenyl TTz crystals. **a)** Absorption spectra of TTz crystals obtained via diffuse reflectance spectroscopy. Inset: UV-Vis absorption spectra of TTzs in solution state. **b)** Photoluminescence spectra of TTz crystals and solution.

TTz-based symmetrically substituted crystals have significantly red-shifted spectra when compared to their solution counterparts. They also exhibit wide variance in their absorption characteristics when compared to each other. These features can be attributed to the unique intermolecular transition dipole orientation and arrangement previously elucidated from crystal packing studies. Since many molecules in a crystal interact with an external field through their local polarizabilities, the energy of each molecular pair established above was considered, Table S3.2. As shown earlier, $(MeOPh)_2TTz$ has 4 unique molecular pair arrangements. The orthogonal pair depicted in Figure 3.3d has the lowest energy, -16.20 kJ/mol. This would explain why $(MeOPh)_2TTz$ crystal has the smallest bandgap. The highest polarization energy in this derivative was represented by the cofacial pair depicted in Figure 3.3a, -53.70 kJ/mol. This wide range of energies exhibited by the molecular pairs of this crystal could explain the broad absorption spectral profile. The three remaining crystal derivatives have at least 1 pair with high energy of > 70 kJ/mol. In the presence of such strongly polarizable pairs, signals from other pairs could be suppressed. Interestingly however, a shoulder in the case of $(BuOPh)_2TTz$ at 443 nm can be observed which could be indicative of strong excitonic coupling within the intermolecular planes. For $(HepOPh)_2TTz$, the peak at 416 nm is caused by the cofacial molecular arrangement depicted in Figure 3.3j. However, it must be noted that the orthogonal arrangement shown in Figure 3.3i is the most energetically stable pair not just in this crystal, but among all the arrangements established in this study, and hence could be responsible for the strong transition at 444 nm leading to the broad spectra and second smallest excitonic bandgap in the TTz crystal series.

Images of the crystals are shown below (Figure 3.6).

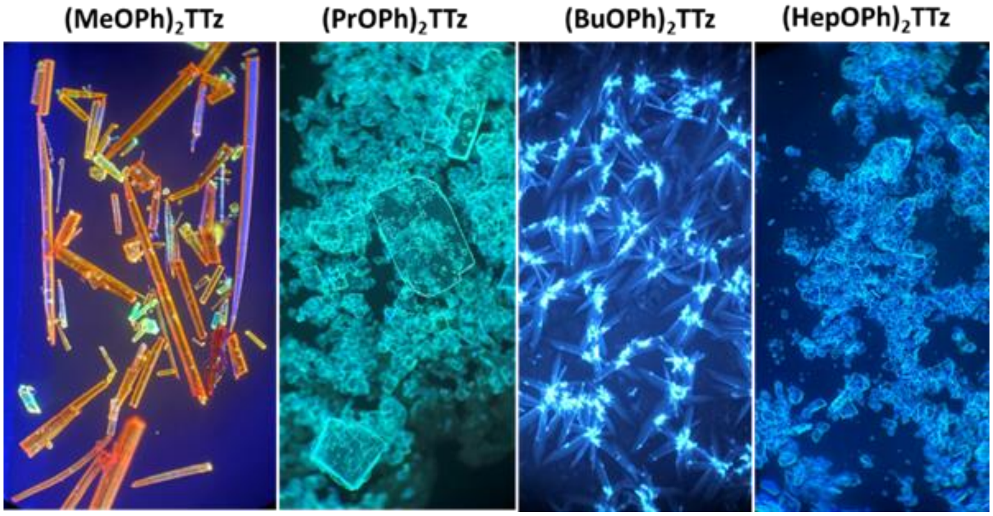

**Figure 3.6.** Images of (CnOPh)$_2$TTz illuminated by UV lamp (400 nm) and viewed under an optical microscope at 10x magnification.

All TTz crystals have red-shifted PL emission when compared to the solution state. (PrOPh)$_2$TTz and (BuOPh)$_2$TTz have the least red-shifted spectra. (BuOPh)$_2$TTz has a relatively sharp emission profile, similar to TTz solution, and hence has blue emission in the solid state. (PrOPh)$_2$TTz has a broad emission profile which renders the crystals cyan fluorescence. The secondary peaks and broad profile could be the result of the low photon energy release from the orthogonal molecular interaction. The effect of the orthogonal interaction is maximized in emission spectra of (HepOPh)$_2$TTz. The transition at 450 nm typically seen among the cofacial pairs in this crystal series is suppressed by the peak at 495 nm. (MeOPh)$_2$TTz has the most red-shifted spectra, and the crystals fluoresce orange-red. This red emission could be due to the weak polarization energy discussed earlier. Among all molecular arrangements established in this study, (MeOPh)$_2$TTz has the most easily polarizable pairs. The orthogonal molecular arrangement depicted in Figure 3.3d could be responsible for the drastic red-shift in this crystal. Recently, Wei et al reported on the origin of red shifted transition in a very similar TTz-based crystal.[112] They propose that the shift is caused mainly due to excitation polarization of unparalleled aggregates. This interpretation would be in congruence with our hypothesis as well. The wide overlap between the absorbance and emission spectrum of $(MeOPh)_2TTz$ could be caused due to anisotropy and is typical with organic crystals.[113] The green emission in the crystal image was maximized by the peak at 525 nm in the emission profile. This is due to surface-to-kernel effect where surface energy perturbs the crystal packing, inducing defects-related-effects. [112, 114]

To further investigate if modulation of molecular packing in crystals would influence the excited state photophysical properties, the TTz crystals were characterized using micro-Raman spectroscopy, Figure 3.7.

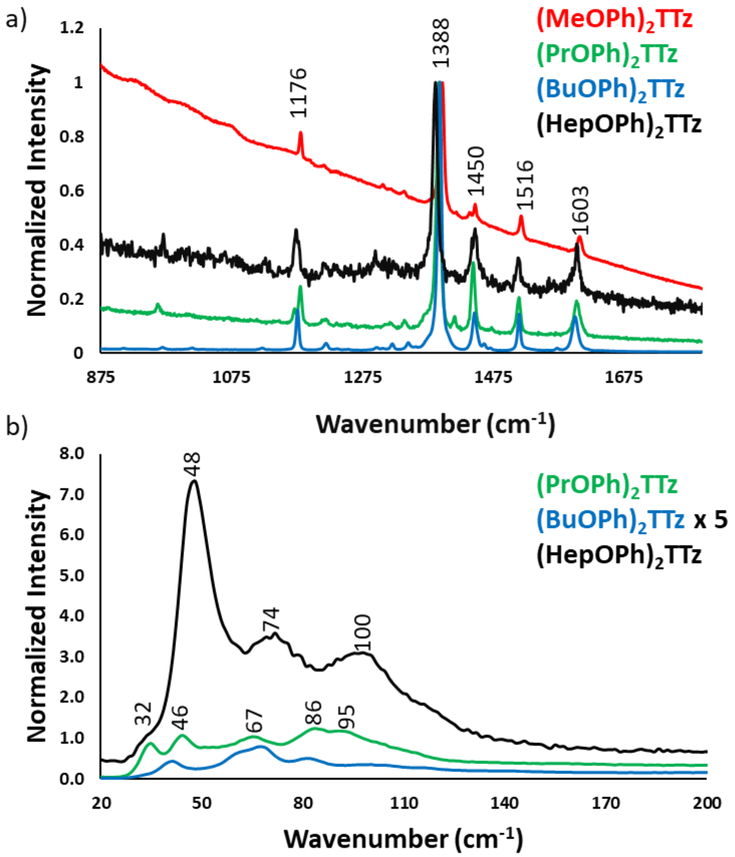

**Figure 3.7.** Micro-Raman Spectra of TTz crystals.

Since the central diphenyl TTz moiety is common in all the derivatives, the spectral signature in the fingerprint region, 875 to 1800 cm$^{-1}$, is the same in all the crystals, Figure 3.7a. The experimental data was verified with DFT simulation and peak assignments have been shown in Figure S3.8. It is, however, interesting to note the difference in the intensity of the spectra. (BuOPh)$_2$TTz exhibited the highest signal to noise ratio with sharp and highly resolved peaks. This was expected since the packing studies revealed that intermolecular interactions are limited to the alkoxy region in this crystal. The crystals that packed in herringbone pattern displayed peaks at much lower intensity.

The region of particular interest lies from 10 to 200 $cm^{-1}$, Figure 7.7b. This region represents lattice-phonon vibration frequencies and has been probed in various studies to identify intermolecular packing dependent effects on photophysical properties in organic crystals.[115-118] The low-energy modes are highly sensitive to molecular packing, which explains the observed difference shown above. All the spectra have been normalized by maintaining the C=N vibration of the thiazole ring at 1388 $cm^{-1}$ constant. Interestingly, $(BuOPh)_2TTz$, which displayed the most intense spectral features in the > 800 $cm^{-1}$ region had highly muted signals in the < 200 $cm^{-1}$ region. The spectrum was amplified by a factor of 5 in the interest of clarity . This further contributes to the packing dependent studies revealing that the intermolecular interactions are localized in the alkoxy appendage. The weak lattice-phonon vibrations juxtaposed against the sharp, unperturbed spectral features from the conjugated backbone would support the prediction that $(BuOPh)_2TTz$ crystal would exhibit excitonic characteristics similar to its solution counterpart. $(HepOPh)_2TTz$ crystal did not exhibit highly sharp features in the > 800 $cm^{-1}$ region. However, it has the strongest lattice vibration in the sub 200 $cm^{-1}$ region with three clear bands. This remarkably intense spectral feature in the weak-energy modes indicates that excited states in this material would prefer to relax via lattice-phonon vibrations leading to low exciton radiative rates and poor fluorescence efficiency. $(PrOPh)_2TTz$ exhibited the second most intense spectral feature in the sub 200 $cm^{-1}$ region. Most of the bands are similar to $(HepOPh)_2TTz$, albeit in different relative ratio. This was expected since both monoclinic crystals pack in herringbone pattern but display subtle differences in intermolecular interaction types and energies. Unfortunately, $(MeOPh)_2TTz$ did not yield any resolvable spectral feature in the lattice vibration region,

Figure S3.9. Nevertheless, it is clear that the alkyl appendages modulate the steady state photophysical properties of these crystals drastically.

### *3.3.2.2 Time-Resolved Photophysical Studies*

The singlet emission lifetime decays of these crystals were measured and shown in Figure 3.8.

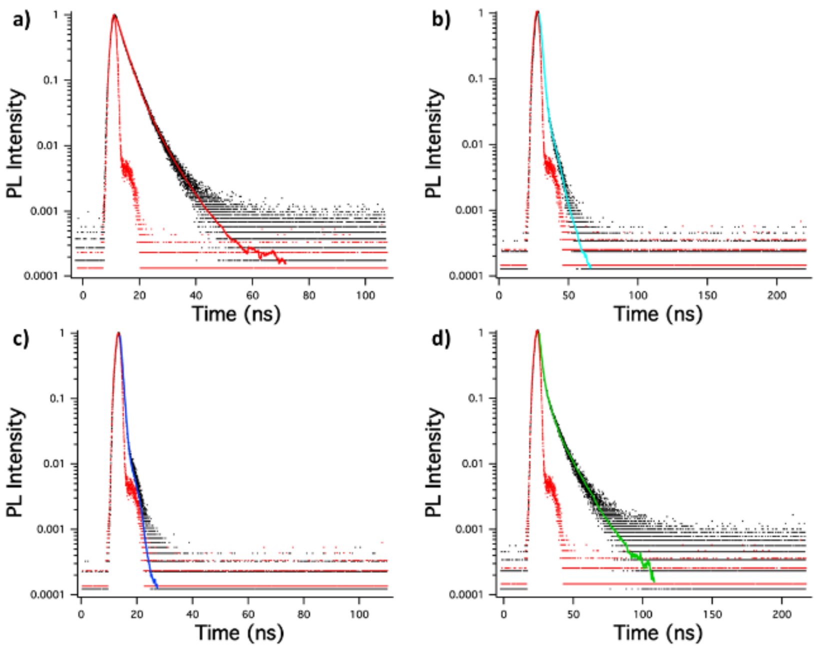

**Figure 3.8.** Singlet emission lifetime decay of a) $(MeOPh)_2TTz$, b) $(PrOPh)_2TTz$, c) $(BuOPh)_2TTz$, d) $(HepOPh)_2TTz$ crystals.

It is interesting to note that the crystals exhibited much longer lifetimes than their solution counterparts. This is expected since bulk organic aggregates require higher reorganization energy than molecular monomers in dilute solutions.[93] The fluorescence decay lifetime of the TTz based crystals was used along with their quantum yield to ascertain luminescence efficiency. This has been shown in Table 3.1 along with excitonic bandgap of the materials derived from absorbance tauc plot.

**Table 3.1.** Excitonic bandgap values, luminescence efficiency data of the symmetrically substituted TTz crystals and solution.

| **Material** | ***Eg* (eV)** | **$\Phi_F$ (%)** | **$\tau_{avg}$ (ns)** | **$k_r$ ($s^{-1}$)** | **$k_{nr}$ ($s^{-1}$)** |
|---|---|---|---|---|---|
| $(MeOPh)_2TTz$ | 2.46 | 10 | 3.35 | $2.99 \times 10^7$ | $2.69 \times 10^8$ |
| $(PrOPh)_2TTz$ | 2.73 | 27 | 1.66 | $1.63 \times 10^8$ | $4.40 \times 10^8$ |
| $(BuOPh)_2TTz$ | 2.74 | 4 | 0.67 | $6.43 \times 10^7$ | $1.43 \times 10^9$ |
| $(HepOPh)_2TTz$ | 2.52 | 0.4 | 2.34 | $1.58 \times 10^6$ | $4.26 \times 10^8$ |
| $(C_nOPh)_2TTz$ (Solution) | 2.98 | 28 | 0.54 | $5.19 \times 10^8$ | $1.33 \times 10^9$ |

$(MeOPh)_2TTz$ crystal exhibited the longest singlet lifetime in the series. This could be because of the pi-pi stacking revealed from the Hirshfeld analysis. Another reason for the long lifetime could be the low polarization energy of the molecular pairs in this crystal. $(HepOPh)_2TTz$ crystal has the second longest singlet lifetime, however, it also has the lowest $\Phi_F$. This could be because the highly energetically stable molecular pairs facilitate exciton delocalization diffused over multiple molecules in the crystal. $(PrOPh)_2TTz$ has the shortest singlet lifetime in the herringbone packing series. However, it has a remarkably high $\Phi_F$. The radiative rate in this crystal is comparable with its solution counterpart which is rare among similar molecular systems. The high radiative rates could be because all the intermolecular interactions in this derivative are centered around the TTz heterocycle. The slipped stacked $(BuOPh)_2TTz$ exhibited radiative decay lifetime similar to its solution state. This could be because of the limited geometry-energy related effects in this derivative. However, the $\Phi_F$ and $k_{nr}$ suggest that the stacking localized around the alkoxy appendages in this J-type aggregate facilitates exciton delocalization.

Clearly, alkyl appendages induced structural modifications in symmetrically substituted D-A-D TTz-based crystals result in predictable modulation of photophysical properties. The change in photophysical properties is a function of molecular packing in these crystals. Having established a correlation between structure and photophysical properties in TTz-based crystals, we demonstrate the relevance of such a pedagogical study by fabricating novel TTz-based crystalline blends for all-organic phosphor-converted color-tuning and white-light emission applications.

### *3.3.3. CIE Engineering*

In the following section, the use of symmetrically substituted D-A-D dialkoxyphenyl TTz crystalline blends for generating a broad range of phosphor-converted light emission is demonstrated. We also prove that these crystalline blends can be used for generating white-light emission.

To determine if the crystalline blends are consistent with the single-crystal structural properties we have established above, the powder X-ray diffractograms of drop cast TTz crystals were compared with the powder diffractograms generated from the SC-XRD studies, (Figure S3.7). Since the XRD pattern of the drop cast crystals were found to be in strong agreement with the single-crystal studies, it stands to reason that they will also exhibit similar photophysical properties. Two sets of parent TTz crystals were chosen based on their diverse PL emission resulting in a potentially wide color-tuning window. The crystallinity of the resultant blends was investigated (Figure 3.9).

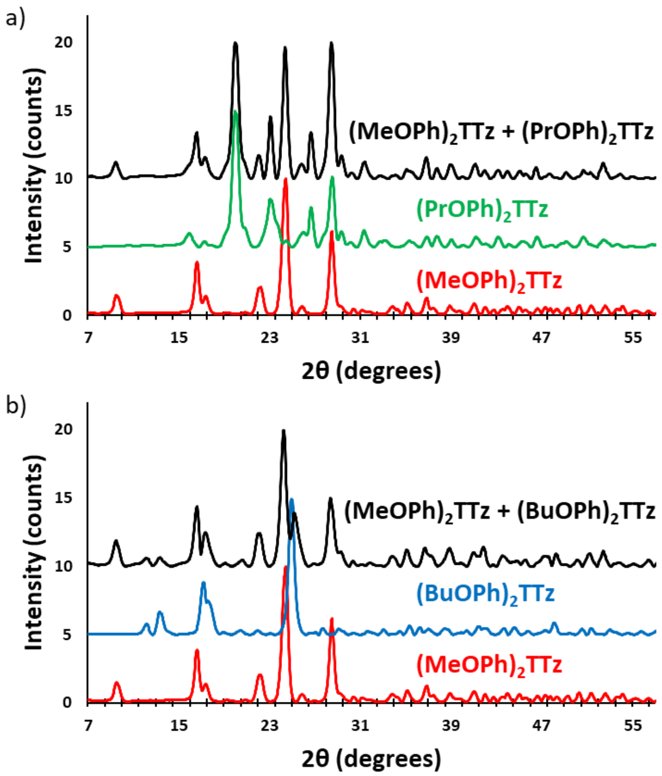

**Figure 3.9.** Powder X-ray diffractograms of parent TTz crystals and their blends. **a)** Set 1: (MeOPh)$_2$TTz, (PrOPh)$_2$TTz, and (MeOPh)$_2$TTz + (PrOPh)$_2$TTz crystalline blend; **b)** Set 2: (MeOPh)$_2$TTz, (BuOPh)$_2$TTz, and (MeOPh)$_2$TTz + (BuOPh)$_2$TTz crystalline blend.

The X-ray diffractograms are conclusive proof that the TTz blends have the crystalline properties of the parent TTz derivatives. Since photophysical properties are a function of crystal packing, excitons can be managed by modulating the parent TTz contribution in the blends. Therefore, the blend proportions were tuned and studied for color-tuning and white-light emission.

Utilizing the multi-fluorochromaticity of the symmetrically substituted dialkoxyphenyl TTz crystals, mixtures of the aggregates were drop cast on glass substrates from saturated DCM solutions with varying proportions by weight, (Figure 3.10). In set 1 (Figure 3.10 (a)), orange-red emissive $(MeOPh)_2TTz$ crystals were mixed with varying proportions of cyan $(PrOPh)_2TTz$ crystal fluorophores. Set 2, (Figure 3.10 (b)), comprised of yellow fluorescent crushed $(MeOPh)_2TTz$ crystals with varying proportions of blue emissive $(BuOPh)_2TTz$ crystals.

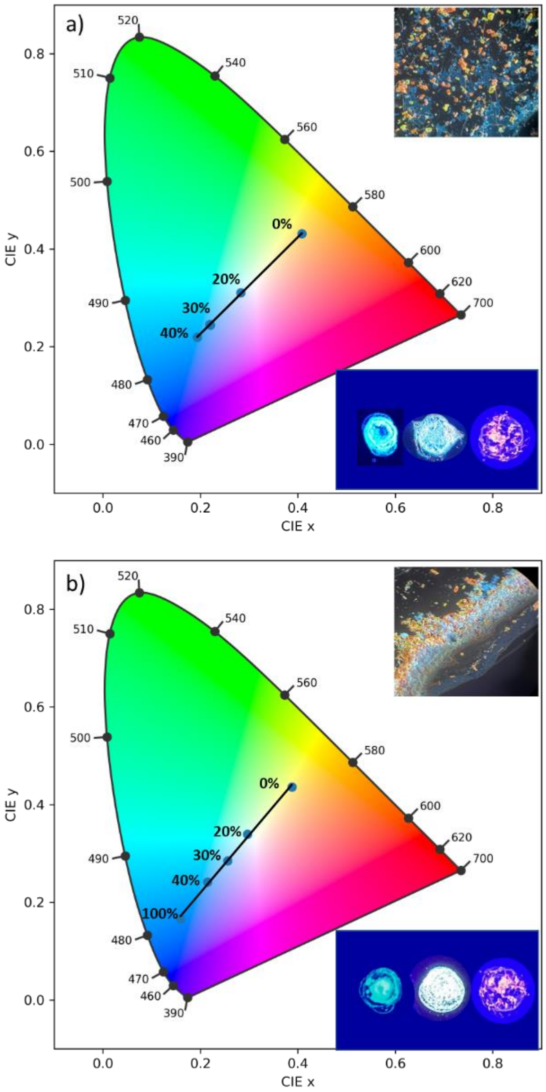

**Figure 3.10.** CIE plot establishing color-tuning capabilities of symmetrically substituted TTz-based dialkoxyphenyl crystals. a) $(MeOPh)_2TTz$ crystals were mixed with $(PrOPh)_2TTz$ crystals at varying weight %. b) Crushed $(MeOPh)_2TTz$ crystals were mixed with $(BuOPh)_2TTz$ crystals were mixed with $(BuOPh)_2TTz$ crystals at varying weight %. Selective weight proportions are plotted for clarity. Top Inset: Optical microscopic image of crystalline admixtures at 4:1 wt% of the symmetrically substituted TTzs illuminated by 400 nm lamp and viewed at 10x. Bottom Inset: Photographs of

$(PrOPh)_2TTz$/$(BuOPh)_2TTz$ (left); $(MeOPh)_2TTz$ (right); and multi-TTz crystalline white-light emissive blend illuminated by 400 nm lamp.

The CIE plots establish that TTz crystals can be utilized for fabrication of multi-fluorochromic mixtures in the solid state. Increasing the contribution of $(PrOPh)_2TTz$ and $(BuOPh)_2TTz$ shifts the emission from $(MeOPh)_2TTz$'s orange-red to blue. This was consistent with our predictions based on the steady state photophysical properties established earlier in this study. The fluorescence of these TTz crystalline blends can be tuned to yield highly contrasting colors by just modulating the crystal concentration. The photostability of these crystals was tested under constant illumination for 5 hours, Figure S3.10. The TTz crystals were found to be highly photostable even in ambient conditions. This additional feature strengthens the case of utilizing TTz-based materials for developing all-organic fluorescent phosphor layers with broad photoluminescence tunability. In both sets, mixtures with 4:1 ratio by weight yielded white-light emissive blends. The simplicity in fabricating these crystalline blends presents a compelling case for utilization of TTz-based materials for photonic and fluorescence-based optical device applications such as *pc*-color-tuning and white-light emission.

## 3.4. Conclusions

TTz-based materials have recently been used for a plethora of optical and optoelectronic applications. Studies utilizing TTz-based materials in the solid state mostly focus on polymeric materials. TTz-based materials have been seldom studied as a small molecule fluorescent dye in the solid state. Arguably this is because there is a significant gap of knowledge in correlating structure with photophysical properties in solid-state symmetrically substituted D-A-D TTz-based materials. In this study, we strategically functionalized TTz-based moiety with varying lengths of alkyl chain appendages. We have established that varying the alkyl chain length modulates the packing mode of these crystalline materials. The variation in packing modes is largely governed by a chorus of synergistic intermolecular non-covalent interactions. We have also established that modulation of crystal packing modes tunes the TTz photophysical properties such as their excitonic bandgap, photoluminescence emission, exciton lifetime, and lattice-phonon vibrational characteristics. The correlation between structure and photophysical properties of symmetrically substituted D-A-D TTz-based materials was then applied to fabricate crystalline blends. We utilized the multi-fluorochromic property of these materials to demonstrate that TTz-based crystals can be used for phosphor-converted color-tuning and white-light-emitting-diode applications. The cost effectiveness, solution processability and environment-friendly features of TTz-based materials present a compelling argument for their incorporation in solid-state photonic and fluorescence-based optical devices. This study will be crucial for the development of photonic materials and devices comprising of TTz-based small molecular fluorescent dyes.

# Chapter 4:

# Managing Photoactivated Enhanced Excimer-like States in Solution-Processable Thiazolo[5,4-*d*]thiazole Films

## 4.1 Introduction

A significant advancement in the field of photochemistry during the mid-20th century was the discovery of excimer states.[120-122] It was found that increasing concentration or temperature of pyrene in solution-state gives rise to an unstructured and broad spectral feature in the fluorescence spectra with pronounced red-shift. Since no corresponding change was observed in the absorption spectrum, it was deduced that the new spectral component must be ascribed to a species formed only after the absorption of light in the excited state. It was proposed that in solutions with higher probability of collision between two molecules (or monomers), a monomer in the excited state forms a complex with a monomer in the ground state. The formation of this new excited state dimer (or excimer) complex is energetically favorable and thus rather stable. Upon relaxation, the excimer dissociates and releases a low energy photon with a large Stokes-shift.

For many subsequent decades, it was widely accepted that excimers have poor photoluminescence (PL) efficiency.[123-126] The large number of monomeric collisions and dimeric aggregation would inevitably result in the relaxation of excited state energy via non-radiative pathways, leading to low fluorescence quantum yield (QY). Notwithstanding, excimers found its relevance in a wide range of applications where a large Stokes-shift was favorable; for example, fluorescence-based sensing and bioimaging.[127-132] In 2003, Antonietti group published a seminal study where they employed mesoporous silica nanospheres to study the effect of confinement on the formation of pyrene excimers.[133] The results demonstrated that excimer formation equilibrium and relaxation kinetics can be modulated by tuning the nanosphere pore sizes. This implied that realization of highly fluorescent excimers was possible contingent on the regulation of excimer formation-relaxation dynamics and modulation of inter-monomeric distances. Building on this work, several other groups reported PL enhancement in pyrene excimers.[134, 135] However, reports on PLQY enhancement due to excimer formation are remarkably rare in the literature.[136, 137] Rarer still, are reports of such phenomena that utilize organic luminophores other than polycyclic aromatic hydrocarbons (PAHs) such as pyrene.[138, 139] This renders a significant gap of knowledge: how to manage excimers and excimer-like states in non-PAH organic luminophores in order to yield enhanced luminescence efficiency.

To address this gap of knowledge, we chose to study an asymmetric thiazolo[5,4-*d*]thiazole (TTz) derivative built on the *D-π-A* architecture. Asymmetric TTz derivatives have been shown previously to be highly fluorescent with near unity PLQY in favorable solvents and polymer-dye blend spin-cast films.[85, 86] Asymmetric TTz dyes exhibit a push-pull effect due to their electron-donating and -withdrawing functional groups. This effect renders a partial positive and negative charge across the molecule which could be favorable for excimer formation and stabilization. TTz is a highly rigid and planar moiety, similar to PAHs. The planarity and restricted intramolecular motions would also be favorable characteristics to promote $S_1 \rightarrow S_0$ radiative decay and modulate excimer formation and radiative relaxation.[137] In this study, we have answered 4 questions: 1) Can asymmetric TTz form excimers in the solution state? 2) Can formation and relaxation of excimer-like states be conserved in polymer-dye blend films? 3) Can formation and relaxation of excimer-like states be regulated to achieve enhancement in luminescence efficiency in films? 4) Can regulating formation and relaxation kinetics of excimer-like states lead to the fabrication of a novel fluorescence-based optical device? We have found that the asymmetric TTz, (which we shall refer to as EHOPhTTzPy here onward) readily forms excimers in solution, albeit exhibiting the typical low luminescence efficiency. Excimer-like emission was found to be conserved in solution processable polymer:dye drop cast films. We use the term 'excimer-like' since the EHOPhTTzPy molecules in these films also interact in their ground state, unlike conventional excimers.[140] Formation and relaxation kinetics of excimer-like states in polymer-dye blend films was dependent on the type of polymer matrix and method of film fabrication. Formation of excimer-like states can be highly controlled as they are strongly dependent on photoexcitation. The strongly coupled excimer-like states yield in highly fluorescent films ($\Phi = 61\%$). Excimer-like emission resulted in enhanced PLQY relative to monomeric emission by over a factor of 8. We have also utilized the excimer-like properties of EHOPhTTzPy films to fabricate a novel stimuli-responsive fluorescent optical device which can be used for anti-counterfeiting and steganographic applications.

## 4.2 Experimental

### Materials and Instrumentation

4-Pyridinecarboxaldehyde, dithiooxamide were purchased from Sigma-Aldrich and used without further purification. 4-(2-Ethylhexyl)oxybenzaldehyde was synthesized using a previously reported procedure. Solvents were purchased from Alfa Aesar Chemicals and used without further purification. $^1$H-NMR measurements were carried out using JEOL 500 MHz NMR. Mass spectrometry measurements were obtained using a Perceptive Biosystems Voyager MALDI mass spectrometer. UV-Vis absorption spectrometric data was obtained using Cary 300 UV-Vis spectrophotometer. Photoluminescence measurements were carried out on Jobin Yvon-Spex Fluorolog. PL decay lifetimes were obtained using a diode laser with a repetition rate of 1 MHz and excitation wavelength of 406 nm. 9,10-Diphenylanthracene in cyclohexane was used as standard reference for quantum yield measurements.[97] Solid state quantum yield measurements were carried out using QuantiPhi-2. Density functional theory (DFT) computational analysis was performed using Spartan '10.

### Preparation of 2-(4-(2-ethylhexyl)oxyphenyl)-5-(4-pyridyl)thiazolo[5,4-*d*]thiazole (EHOPhTTzPy)

4-Pyridinecarboxaldehyde (0.84 g, 7.8 mmol) and 4-(2-ethylhexyl)oxybenzaldehyde (1.83 g, 7.8 mmol) was reacted with dithooxamide (0.85 g, 7.06 mmol) in 10 mL n-propanol and refluxed for 70 h. The crude product was gravity filtered and washed with excess cold n-propanol. It was then purified via column chromatography using a mixture of chloroform and hexanes (10:1). The reaction yielded

1.79 g, 60% product. Sample purity was confirmed using $^{1}$H-NMR (Figure S3.1) and MALDI-TOF MS (Figure S3.2).

$^{1}$H-NMR (500 MHz, $CDCl_3$, TMS, $\delta$): 8.75 (d, $J = 2.07$, 2H), 7.95 (dd, $J = 3.66$, 4H), 7.01 (d, $J = 1.75$, 2H), 3.92 (d, $J = 2.0$, 2H), 1.76 (m, 1H), 1.59 (m, 6H), 0.92 (m, 8H). UV-Vis $\lambda_{max}$ (Toluene, $\varepsilon = M^{-1}\ cm^{-1}$): 374 nm ($\varepsilon = 1766$). MALDI-TOF-MS (calcd. for $C_{23}H_{25}N_3OS_2$, $[M + H]^+$): 424. 59, found: $M = 424.62$. Quantum yield in toluene

($\lambda_{ex} = 374$ nm, $\lambda_{em} = 436$ nm) = 99%.

## 4.3 Results

### 4.3.1 Solution-based studies

#### 4.3.1.1 Solvatofluorochromism

Excimers are formed when two monomers are brought in close proximity to each other. Asymmetric TTz functionalized with an electron-withdrawing and -donating group exhibits a difference in electron density distribution along the monomer. This difference could facilitate and encourage formation and stabilization of excimers. A typical result of the push-pull effect in TTz-based materials is solvatofluorochromism. Therefore, to investigate if EHOPhTTzPy is a suitable candidate for excimer formation, solvatofluorochromic studies were conducted, Figure 4.1.

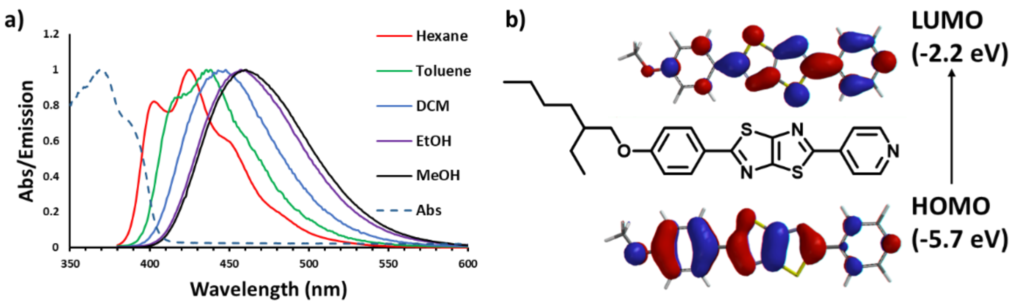

**Figure 4.1.** EHOPhTTzPy exhibiting a) solvatofluorochromism and b) push-pull effect.

From the absorption and emission spectra, it is clearly evident that EHOPhTTzPy exhibits solvatofluorochromism. The fluorescence spectra red-shifts with increasing solvent polarity whilst no change is observed in the absorption spectra. Table S4.1 contains further optical spectrophotometric details of EHOPhTTzPy in different solvents. The push-pull effect was modeled and pictorial representation of HOMO and LUMO states have been shown. This difference in the electron density distribution will render a partial change in electrostatic charge on the monomer which could facilitate intermonomeric interactions leading to formation of dimers.

To further characterize the excited state properties of the EHOPhTTzPy in solution, the Lippert-Mataga equation was employed (eq 1),

$$\nu_a - \nu_f = \frac{(\mu^* - \mu)^2}{4\pi\varepsilon_0 hca^3}\Delta f + const\ ;\ \Delta f = \left(\frac{\varepsilon - 1}{2\varepsilon + 1} - \frac{\eta^2 - 1}{2\eta^2 + 1}\right) \qquad (eq\ 1)$$

where $\nu_a$ and $\nu_f$ are the wavenumbers of the absorption and emission peaks in cm$^{-1}$, respectively. The dipole moment of ground and excited state are denoted by $\mu$ and $\mu^*$. Vacuum permittivity is denoted by $\varepsilon_o$; $h$ is Plank's constant; $c$ is the speed of light; $a$ is the Onsager cavity radius; $\Delta f$ is the orientation polarizability; $\varepsilon$ is the relative permittivity;

and $\eta$ is the refractive index. The ground state dipole and the Onsager cavity radius were measured using Spartan 16 software. The Lippert-Mataga plot has been shown in Figure 4.2.

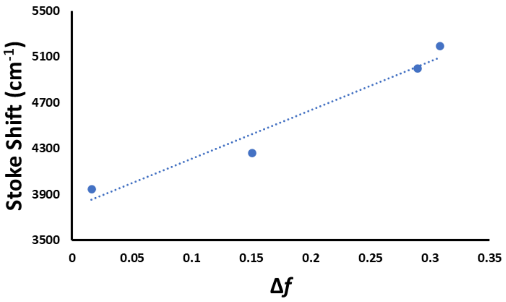

**Figure 4.2.** Lippert-Mataga plot of EHOPhTTzPy

From the slopes of the Lippert-Mataga plot shown above, the change between the dipole moments of the ground and excited states was determined. Even though the Lippert-Mataga equation assumes no specific solvent−solute interactions (e.g., hydrogen bonding) and ignores solute polarizability, a high degree of linearity suggests the estimation of the excited-state dipole is reliable. The Onsager radius was measured to be 7.17 Å. The ground and excited state dipoles are 5.30 D and 17.79 D respectively. Thus, the change in dipole is 12.49 D. Similar dipole moments have been previously reported for TTz based materials exhibiting strong intramolecular charge transfer characteristics.[85, 86]. The high difference in the dipole moment between the ground and excited states supports the proposition that upon photoexcitation, EHOPhTTzPy can form excimers.

### 4.3.1.2 Excimer Formation in Solution

Modulation of photophysical properties of organic luminophores in the solid state has always been a challenging task. A reasonable proposition to address would be to first establish whether the asymmetric TTz can form excimers in the solution state. Since excimer formation is dependent on a higher statistical probability of monomeric collisions, concentration and temperature dependent studies are widely used to probe the nature of excimers in solution-based studies.

#### 4.3.1.2.1 Concentration Dependent Studies

Excimer formation and relaxation kinetics of the asymmetric TTz were probed by decreasing the concentration of the monomers, Figure 4.3.

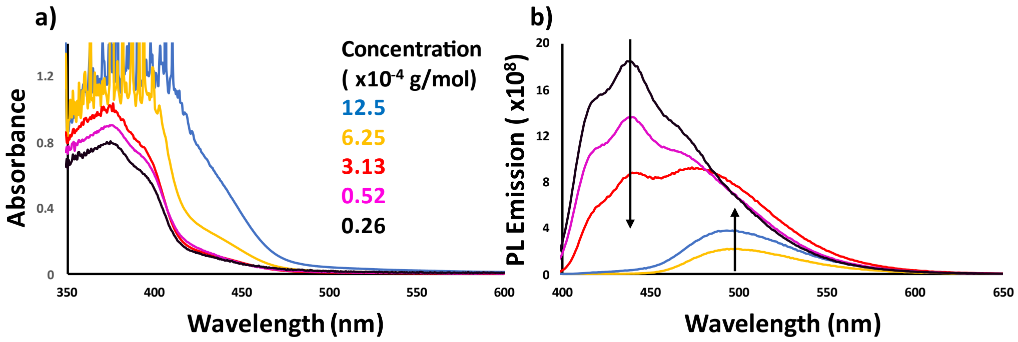

**Figure 4.3.** a) UV-Vis absorption and b) PL emission spectra of EHOPhTTzPy as a function of concentration.

Highly concentrated samples were made where inner-filter effects were evident, and no resolvable absorption spectral feature could be obtained at the absorption maxima. At these high concentrations, excimer formation is represented by a broad, unstructured, and red-shifted peak in the PL spectra at 500 nm. As the sample is serially diluted, the excimer emission intensity is decreased and the monomeric emission increases indicating clear vibronic bands. There is no change in the absorption spectrum other than the width of the peak which is expected with variation in concentration. If the red-shift in the PL emission spectra was caused due to conventional aggregation, it would have been evident in the absorption spectra. Moreover, it can be deduced that the red-shift in the PL emission spectra is caused by species that is formed only after the absorption of energy. This is strong evidence for the formation of excimers in highly concentration solutions of EHOPhTTzPy. Similar concentration dependent studies were also conducted using the two disubstituted byproducts of the TTz reaction. Neither of the disubstituted TTz-based materials yielded in excimer formation. This adds to the validation of the initial hypothesis that the electrostatic difference due to the push-pull effect is crucial for formation of excimers.

#### 4.3.1.2.2 Temperature Dependent Studies

A dilute solution of EHOPhTTzPy at 2.05 x $10^{-5}$ g/mol concentration was made and temperature dependent studies were conducted. Although no noticeable excimer emission was visible in steady-state PL emission spectra, time-resolved studies provided strong support for the presence of excimers. The line of best-fit of the decay spectra at 450 nm has been shown in Figure 4.4.

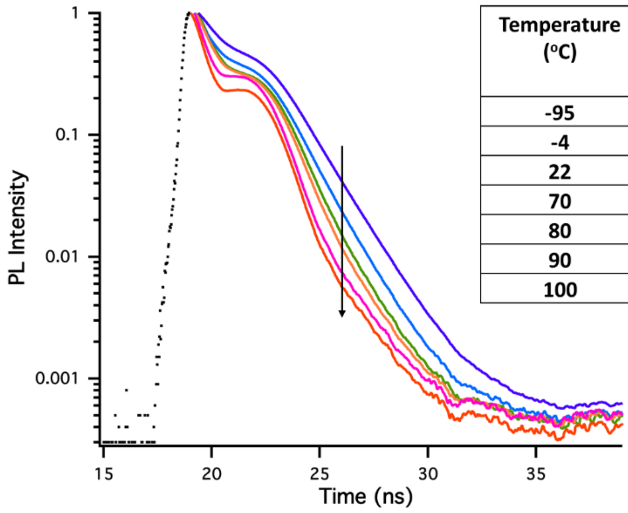

| Temperature (°C) | Average lifetime (ns) monomer [450 nm] | Average lifetime (ns) monomer + excimer [500 nm] |
|---|---|---|
| **-95** | **1.26** | **1.38** |
| **-4** | **0.95** | **0.93** |
| **22** | **0.7** | **0.93** |
| **70** | **0.7** | **1.59** |
| **80** | **0.57** | **1.71** |
| **90** | **0.5** | **2.72** |
| **100** | **0.44** | **3.06** |

**Figure 4.4.** Line of best-fit of time-resolved PL decay curves at different concentrations collected at the monomer maxima (450 nm). Inset: Table listing the temperature, monomer PL decay lifetime at 450 nm and monomer + excimer decay lifetime at 500 nm.

At the monomer maxima, the PL decay is longest when the solvent surrounding the monomers have frozen. As the temperature increases, the monomeric emission lifetime decreases progressively. On the other hand, at excimer emission maxima (500 nm) the PL decay lifetime increases with increase in temperature. At 100 ºC, the excimer lifetime is significantly longer than the monomeric emission. Since excimers are characterized by longer emission decay lifetimes than the corresponding monomers, temperature dependent studies reveal another supporting evidence for the formation of excimers in EHOPhTTzPy solutions.

Having established that EHOPhTTzPy can form excimers in solutions, we shall now proceed with understanding and modulating excimer formation and relaxation kinetics in confined films.

### 4.3.2 Modulation of Excimer-like States in Films

As mentioned earlier, formation and relaxation kinetics of excimer-like states have been previously shown to be controllable in confined spaces. However, most of these reports have utilized supramolecular complexes, mesoporous nanoparticles, or micellar assemblies.[141, 142] A substantially simpler method to confine an organic luminophore is embedding it in a neutral polymer matrix. Embedding organic luminophores in polymers increases the solution processability of the dye while also advancing the capability of the technology by capitalizing on the unique and well-established properties of the polymer matrices. Also, in most polymer-dye blends, the composition of the dye ranges from 0.1 – 2 wt.%, making this method remarkably economical and environmentally friendly. Due to such advantages, studies that incorporate organic luminophores in polymer matrices are highly ubiquitous in the literature. However, there have been very few reports that probe the nature of formation and relaxation kinetics of excimer-like states in polymer-dye blend films.

In the following sections, we demonstrate that excimer formation and relaxation kinetics in EHOPhTTzPy can be conserved and modulated in polymer-dye blend films.

#### 4.3.2.1 Controlling Excimers-like States by Modulating the Excitation Energy

Polymer-dye blends containing 1 wt.% EHOPhTTzPy in poly(methyl methacrylate) (PMMA) matrix dissolved in toluene were used to fabricate drop-cast films on pre-cleaned glass substrates. Since excitation of monomers is essential for excimer formation, we chose to irradiate the films with UV light of 405 nm maxima. It was found that upon irradiation with UV light the absorption and emission profiles of the films changed. The films were therefore subjected to 30 s of periodical UV light exposure and the absorption and emission spectra are shown in Figure 4.5.

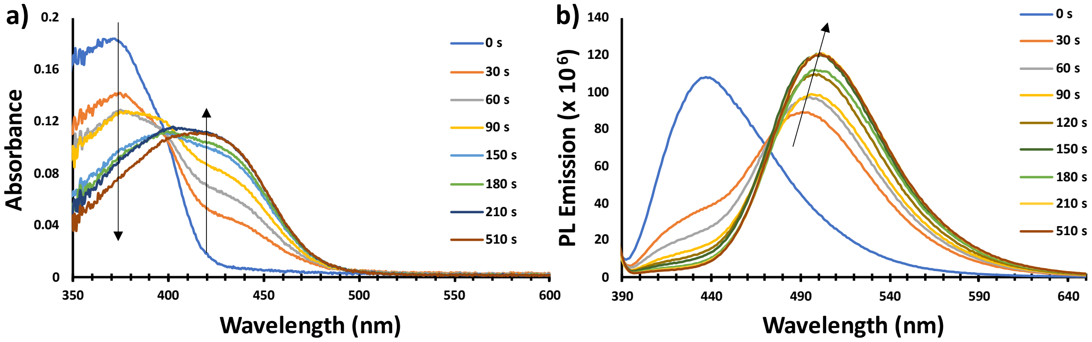

**Figure 4.5.** a) UV-Vis Absorption, and b) PL emission spectra of 1 wt.% EHOPhTTzPy in PMMA matrix upon irradiation with UV light.

The pristine film exhibited absorption and emission behavior resembling the monomeric dye characteristics in solution as discussed earlier in this study. The absorption peak maxima at 372 nm rendered a colorless/transparent film while an emission maxima at 440 nm made the film fluoresce at the edge of violet and royal blue. After 30 s of irradiation with UV light, the monomeric absorption and emission spectral signature of EHOPhOTTzPy have substantially reduced. At the same time, the presence of another species is observed that absorbs at 435 nm and emits at 493 nm. With further UV irradiation, the absorbance of this new peak progressively increases as the monomeric absorption diminishes. A similar pattern is observed in the PL emission spectra where, as the irradiation is continued, the monomeric emission subsides and a pronounced broad, unstructured peak increases in intensity with a large Stokes-shift. Since the absorbance of this new species is lower than the monomers in intensity and energy, it can be deduced that this species is a highly stable, strongly coupled complex. The PL emission spectral profile is remarkably similar to the excimer emission observed in Figure 4.3. In both cases, the emission peak is at 500 nm and the profile is broad, unstructured, and no clear vibronic bands are present. This is a compelling argument to ascribe this new species as a strongly coupled excimer-like state. From the PL emission spectra, it is clearly evident that upon irradiation, the strongly coupled excimer-like states lead to substantial PL enhancement in confined films.

Photographs of the films are shown in Figure 4.6.

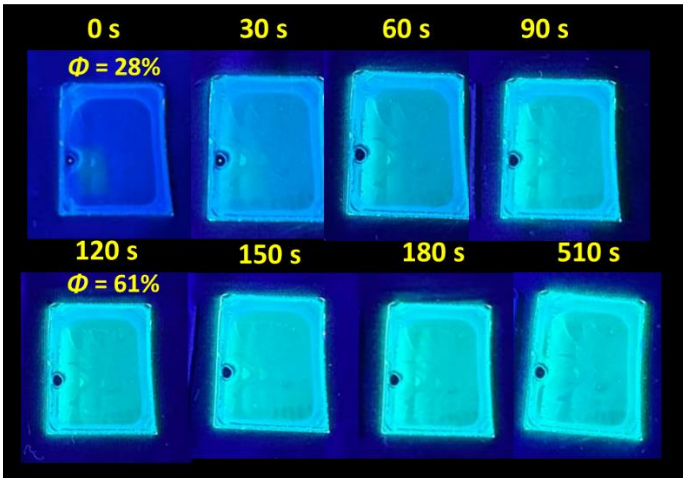

**Figure 4.6.** Photographs of EHOPhTTzPy films irradiated with UV light.

The pristine film fluoresces at the edge of violet and royal blue ($\lambda_{max}$ = 440 nm). It is evident that when the films are irradiated with UV light, the fluorescence changes. The fluorescence change is due to the formation of strongly coupled excimer-like states. This implies strongly coupled excimer-like states can be formed with an astonishingly high level of control. Also, the fluorescence of the films can be tuned by modulating the monomer and excimer-like states contribution in solution processable films.

The absolute quantum yield of the films was measured. The pristine films exhibited respectable luminescence efficiency at 28%. All-organic dye films displaying such high quantum yield in the violet/royal blue edge is rare. Rarer still, is the increase in luminescence efficiency upon the formation of excimer-like states. As mentioned earlier, excimers are notorious for plummeting the fluorescence quantum yield of an organic luminophore. Here, however, we observe an increase in PLQY by over a factor of 2. Confining the strongly coupled excimer-like states in a neutral polymer matrix restricts intramolecular rotations which promotes radiative recombination of excitons. Increase in PLQY due to excimer-like states is an extremely rare occurrence and deserves further investigations. These investigations have been discussed below.

### 4.3.2.2 Dependence of Formation of Excimer-like States on Film Fabrication Method

In the previous section, we presented evidence that strongly coupled excimer-like states are formed in EHOPhTTzPy:PMMA drop cast films. The formation of excimer-like states results in PL emission enhancement and an increase in the PLQY by over a factor of 2. Excimer-like emission resulting in enhancement of luminescence efficiency is an extremely rare occurrence. A simpler explanation for the red-shift and PLQY enhancement could be ascribed to a chemical process between the dye, polymer, and the solvent. To investigate this further, we compared two methods of film fabrication: drop cast and spin cast. Both films were irradiated with UV light for periodic intervals. The PL emission spectra has been shown in Figure 4.7.

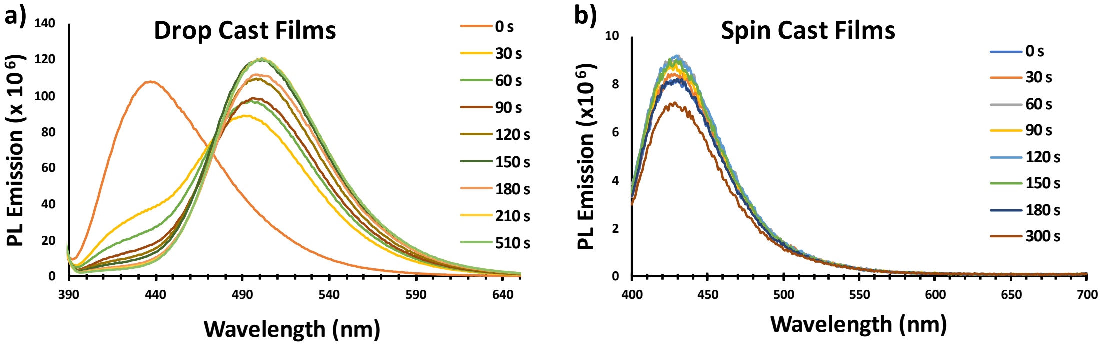

**Figure 4.7.** PL emission spectra of films of EHOPhTTzPy 1 wt.% in PMMA fabricated via two methods: a) Drop cast slow-evaporation, and b) Spin cast method.

In the case of films fabricated via the drop cast method, the solvent was allowed to evaporate slowly at room temperature. In the spin cast films, the solution was dispensed slowly on a substrate already spinning at 2500 rpm. The high shear stress on the monomers would mitigate the possibility of dimer formation on the substrate, thus serving as a control against aggregation-induced effects.

In drop cast films, we observe the decrease in monomeric emission and enhancement in PL emission upon irradiation with UV light. However, in spin cast films, only monomeric emission is visible. Irradiating the spin cast films with UV light neither changes the monomeric PL emission, nor exhibits any presence of excimer-like emission. This leads us to draw the following conclusions: 1) The red-shift in PL emission and PLQY enhancement is not caused by a chemical process. Both the films were cast using the same solution. If the red-shift and PLQY enhancement was caused by a chemical process, like protonation of the pyridyl group, the effect would be evident in the spin cast films as well. 2) The red-shift and PLQY enhancement is caused by a physical process. Since the change in optical characteristics of the film is not caused by a chemical process, it must be caused by a physical process. The only difference between the two methods of film fabrication was the decreasing degrees of freedom imposed on the dye monomers by the slowly evaporating solvent. It is reasonable to envision that as the solvent evaporates, the dye molecules form weakly coupled dimers which still fluoresce as the monomers. 3) There are no dimers formed in the solution. The effect of any dimers formed in the solution would have been evident in spin cast films. Since there is no sign of excimer-like emission in spin cast films, it can be deduced that no dimers are formed in the solution. This bodes well for the processability and upscaling of the polymer-dye system.

From the comparative study of drop cast versus spin cast films, it is clear that the emission is caused by excimer-like states. But the role of UV irradiation is still unclear in the PL shift and PLQY enhancement. The following section elucidates the role of UV irradiation in the formation of excimer-like states and the subsequent increase in the luminescence efficiency.

#### 4.3.2.3 Role of Irradiation towards Formation of Excimer-like States

In the earlier sections we have demonstrated a remarkable property in these polymer-dye blend films: high level of control over formation of excimer-like states via UV irradiation. To investigate the role of irradiation further, we fabricated drop cast films of 1 wt.% in PMMA matrix and irradiated them for 5 mins with different light sources. The films were encased in petri-dishes and kept at a 15 cm distance from the light source to control for any heating related photophysical effects. The subsequent absorption and emission spectra are shown in Figure 4.8.

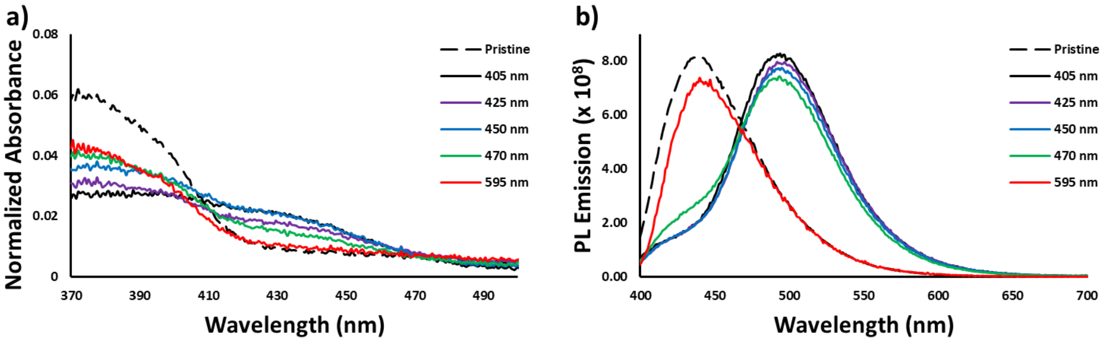

**Figure 4.8.** Steady state a) UV-Vis absorption and b) PL emission spectra of EHOPhTTzPy:PMMA drop cast films after irradiation with different light sources for 5 mins.

As expected, the light source at 405 nm led to the formation of excimer-like states. In fact, any light source with $\lambda_{max} > 435$ nm resulted in the formation of excimer-like states. In the case of light sources with emission maxima at 450 nm and 475 nm, there is an overlap over the 435 nm region, Figure S4.3. This overlap is significant in light source with $\lambda_{max} = 450$ nm. However, the overlap is limited for the 475 nm light source. This explains why the monomer emission has not completely subsided and formation of excimer-like states is limited in this case. In the case of amber light source ($\lambda_{max} = 595$ nm), there is no change in the absorbance or PL emission. This proves that the observed red-shift and PLQY enhancement is contingent on the absorption of light. This was a fundamental premise that led to the discovery of excimers as discussed by Förster. Excimers are only formed when light is absorbed. Without the absorption of light, as in the case of light source with $\lambda_{max} = 595$ nm, no excimer-like states are formed. This result adds to the already existing pool of compelling evidence that the observed red-shift and PLQY enhancement is indeed due to the controlled formation and relaxation of excimer-like states. Irradiation of films with a light source is critical for formation of excimer-like states. However, it must be noted that once a strongly coupled excimer-like state has been formed, further irradiation has a minimal role to play in modulation of the excimer-like emission. The strongly coupled excimer-like states are highly stable and further irradiation does not reduce or change the inter-monomeric distances. If that were the case, such variations would lead to the formation of a new photophysical species which would exhibit even more red-shifted spectral features than $\lambda_{ab}$ = 435 nm and $\lambda_{em}$ = 500 nm. However, we observe that longer irradiation time does not result in the evolution of a new photophysical species, but an increase in the existing excimer-like signal intensity. The role of irradiation is to just create excimer-like complexes. The longer a film is irradiated, the higher the number of excimer-like states are formed.

#### 4.3.2.4 Dependence of Excimer-like States on Concentration

The formation of excimer-like states is a function of concentration. In this section, we investigated the effect of concentration on the PL emission and luminescence efficiency in EHOPhTTzPy:PMMA drop cast films. In Figure 4.9, PL emission profiles and intensities are compared for films with varying wt.% of EHOPhTTzPy.

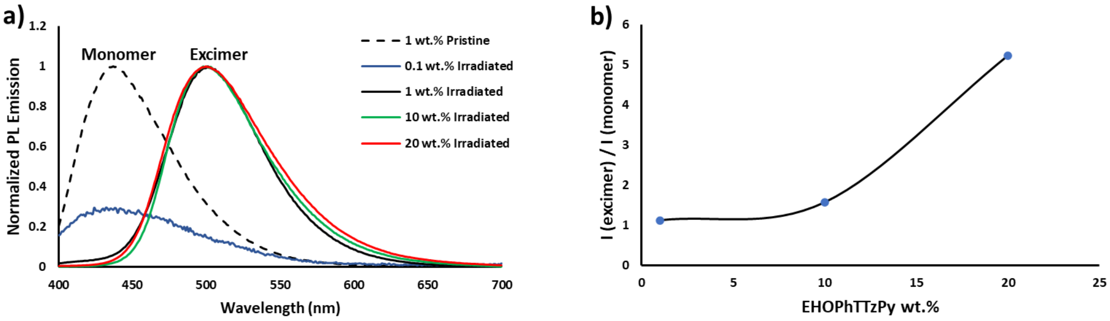

**Figure 4.9.** PL emission characteristics of EHOPhTTzPy:PMMA drop cast films with varying wt.% of the luminophore. a) Fluorescence emission spectra of pristine and UV irradiated films are compared; b) the ratio of monomer (pristine) and excimer-like (post-irradiation) emission maxima of the corresponding films are plotted as a function of dye concentration.

In films with low dye concentration, such as 0.1 wt.%, there is no formation of excimer-like states observed after irradiation with UV light. The formation of excimer-like states is increased with increase in concentration. The emission maxima of pristine and irradiated films were compared, and their ratio has been plotted as a function of dye concentration. The emission intensity exhibits an exponential increase with increasing dye concentration.

The luminescence efficiency of the films was measured and has been shown in Table 4.1.

**Table 4.1.** PLQY of films with varying wt.% of EHOPhTTzPy.

| **EHOPhTTzPy wt.%** | **$PLQY_{Pristine}$** | **$PLQY_{Irradiated}$** | **$PLQY_{Irradiated}/PLQY_{Pristine}$** |
|---|---|---|---|
| 0.1% | 27.43% | 27.37% | 0.99 |
| 1% | 27.83% | 61.01% | 2.19 |
| 10% | 4.01% | 20.18% | 5.03 |
| 20% | 1.24% | 10.15% | 8.19 |

There is no difference in the PLQY of the film where no excimer-like states are formed. A remarkable increase in the PLQY of 1 wt.% films has been shown. As the dye concentration increases, aggregation-caused-quenching effects arise. This is evident from the decrease in the PLQY of pristine films. However, the increasing PLQY due to formation of excimer-like states is a matter of utmost significance. As mentioned earlier, excimers are notorious for reducing the luminescence efficiency of a system. Here however, we demonstrate an 8-fold increase in the PLQY led by the formation of excimer-like states in solution processable films. Such an increase in luminescence efficiency due to excimer-like states is an extremely rare phenomenon. The high-level of control over the formation and relaxation kinetics of excimer-like states, paired with the increasing luminescence efficiency in solution processable films makes asymmetric TTz-based dyes a rather unique and novel candidate for photonic and optical devices based on excimer-like states.

Having elucidated the dynamics of excimer-like states in PMMA films as function of film fabrication method, excitation energy, and dye concentration, we shall now investigate the effect of the polymer matrix that surrounds the dye molecules and the role it plays in the formation and relaxation kinetics of EHOPhTTzPy excimer-like states.

#### 4.3.2.5 Role of Polymer Matrix in Dynamics of EHOPhTTzPy Excimer-like States

Previously we have discussed the effect of confinement on the formation and relaxation kinetics of excimer-like states. Excimers, which are notorious for facilitating relaxation of excited-state energy through deleterious pathways, can be encouraged to yield high luminescence quantum yield if they can be effectively confined. The polymer matrix in these polymer-dye blends serves the function of confinement. However, polymer matrices do not truly confine or restrict the intramolecular rotations at the molecular level. A helpful analogy to describe the role of polymer matrices in these blends is that of a net.[140] Based on the rigidity of the matrix, intra- and intermolecular interactions can be modulated. A reliable measure of the rigidity of a polymer is represented by its Young's modulus. Since a central thesis of this work is that high PLQY from EHOPhTTzPy films is due to confinement and restriction of the excimer-like states, we tested excimer-dynamics in two more polymer matrices with rather different Young's modulus. At the lower end of rigidity, we chose Styrene-butadiene-styrene (SBS) co-block polymer which has a bulk Young's modulus of 73 MPa.[143] We chose Polystyrene (PS) along with the already discussed PMMA polymer to represent polymer matrices with higher bulk Young's modulus; 3.37 GPa, and 3.9 GPa respectively.[144, 145] Films containing 1 wt.% EHOPhTTzPy in 10 mg/mL polymer solution were drop-casted. The steady state characteristics of the films are shown in Figure 4.10, pre and post irradiation for 5 mins.

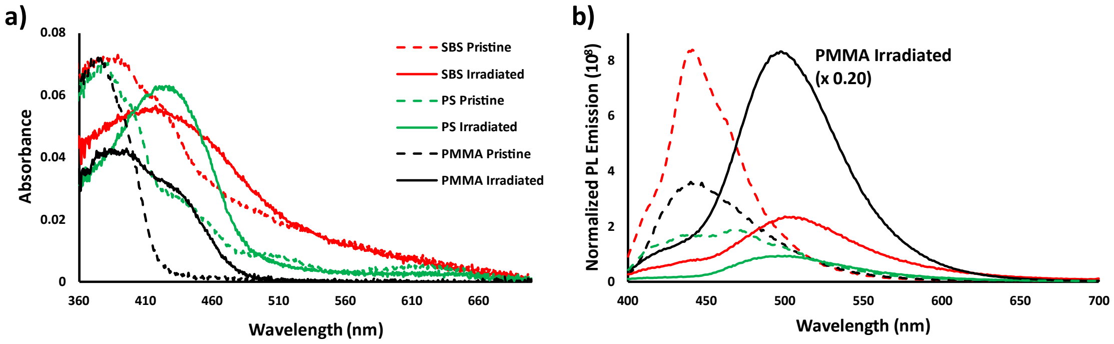

**Figure 4.10.** The formation and relaxation kinetics of excimer-like states is a function of the surrounding polymer matrix. Steady-state spectra. a) absorption and b) PL emission profiles of films cast with different polymer matrices.

At the outset, it is evident that in all three polymers, excimer-like states are formed upon irradiation. This was expected since the formation of EHOPhTTzPy excimer-like states are dependent on film fabrication method and not on the type of polymer matrix used. However, the polymer matrix does tune the properties of the films and the excimer-like states. For example, SBS rendered a fuzzy film upon curing which is denoted from the broad absorption spectra.

The PL emission spectra shows clear transition from monomer to excimer-like emission in all three systems post irradiation with UV light for 5 mins. However, the intensity of the excimer-like emission varies drastically. In case of PMMA film, the excimer-like emission had to be scaled down by a factor of 0.20 for sake of clarity. The excimer-like emission in SBS film reduced dramatically compared to the monomeric emission. This was expected since SBS is not a rigid polymer and hence it is unable to confine the excimer-like states efficiently.

To quantify the luminescence efficiency of the films pre and post irradiation, solid state fluorescence quantum yield was measured and has been shown in Table 4.2.

**Table 4.2.** Solid state fluorescence quantum yield of films pre and post UV irradiation.

| **Polymer** | $\mathbf{PLQY}_{\mathbf{Pristine}}$ | $\mathbf{PLQY}_{\mathbf{Irradiated}}$ | $\mathbf{PLQY}_{\mathbf{Irradiated}}/\mathbf{PLQY}_{\mathbf{Pristine}}$ |
|---|---|---|---|
| **SBS** | 4.58% | 3.24% | 0.71 |
| **PS** | 9.00% | 14.18% | 1.58 |
| **PMMA** | 27.83% | 61.01% | 2.19 |

As expected, increase in luminescence efficiency in films due to excimer-like states can be observed only in films that utilize a polymer matrix with high Young's modulus. Since SBS is not a rigid polymer matrix, the excimer-like states relax via non-radiative pathways. This results in lowering of the PLQY. Therefore, it can be concluded that embedding the dye in a rigid polymer matrix with high Young's modulus is crucial for obtaining enhanced luminescence from excimer-like states.

### 4.3.3 Development of a Novel Optical Device based on Excimer-like States

We have demonstrated that excimer-like states with high luminescence efficiency can be formed, and their relaxation kinetics can be controlled via confinement in polymer matrices. In this section, we have utilized the above stated properties to fabricate a novel optical device based on the dynamics of the excimer-like states.

As mentioned earlier, upon irradiation with an appropriate light source, pre-associated weakly coupled dimers arrange in a strongly coupled excimer-like arrangement. Aggregation of matter is a thermodynamically driven process. Therefore, we hypothesized that if energy is introduced to the system, the dimers can be disaggregated, and monomeric emission can be recovered. To test this hypothesis, we fabricated a EHOPhTTzPy:PMMA film containing 1 wt.% dye via drop cast method. This film was irradiated to generate excimers. Then the film was annealed at 200 °C which is the melting point of PMMA. The PL emission spectra and photograph of the film through different stages are shown in Figure 4.11.

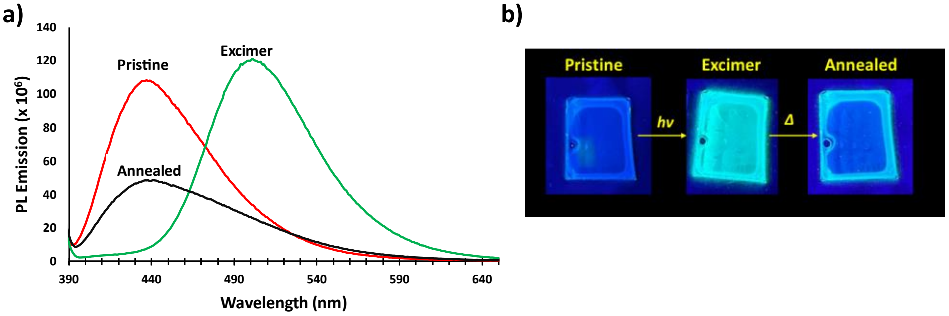

**Figure 4.11.** Fabrication of a novel optical device based on dynamics of excimer-like states. a) PL emission spectra of pristine, irradiated, and annealed films showing recovery of monomer emission in films. b) Photographs of the films.

The pristine film exhibits the monomeric violet/royal-blue emission. Upon irradiation for 5 minutes with UV light, the excimer-like emission has been maximized. As expected, upon annealing, the strongly coupled dimers can be disaggregated and the monomeric emission can be recovered. The controlled coupling of dimers and the stimuli-responsive character in these films leverages the system to be used in anti-counterfeiting and steganography among other applications.

### 4.4 Discussion

We have probed the formation and relaxation kinetics of EHOPhTTzPy excimer-like states in polymer-dye blend films. We have also reported that these excimer-like states can be leveraged to form highly luminescent solution processable films. High PLQY of excimer-like states is a rare phenomenon and therefore deserves an explanation of the underlying photophysical mechanism, Figure 4.12.

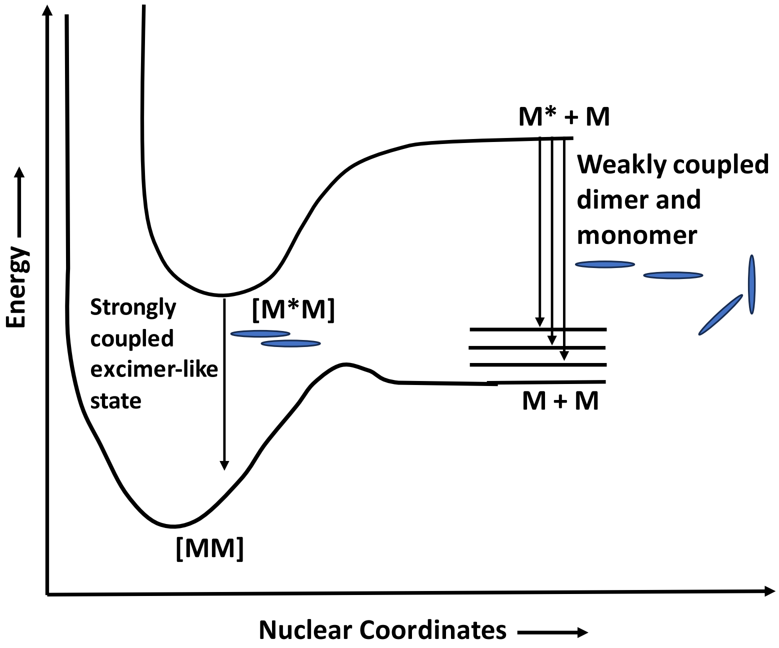

**Figure 4.12.** Proposed mechanism of EHOPhTTzPy excimer formation in films.

In the ground state, the electron density is concentrated at the donor group of EHOPhTTz. This renders a difference in the electrostatic charge distribution along the monomer, (M). When the films are cured, the difference in the electrostatic charge distribution facilitates the formation of weakly coupled pre-associated dimers, M+M. When one of the monomers in these dimers absorb light, the electron density shifts to the acceptor pyridyl group, M*+M. This shift in electron density causes the dimers embedded in the netlike polymer matrix to rearrange in a conformation that encourages strong excitonic coupling resulting in the formation of an excimer-like state, [M*M]. As this excimer-like state relaxes, it emits the photon of 2.48 eV, [MM]. It should be noted that once a dimer with strong excitonic coupling is formed in films, it does not dissociate back to the weakly coupled dimer state after relaxation of the excited state energy. This indicates that the strongly coupled dimer is highly energetically stable even in the ground state. The stable dimers dissociated only after melting the polymer matrix, at which point the monomeric (or weakly coupled dimeric) emission was recovered.

The high level of control over formation of excimer-like states, and their relaxation kinetics was possible because of the intramolecular charge transfer along the individual monomers. This leads us to envision the possibility that high PLQY in films with confined excimer-like states can be realized with other organic luminophores that exhibit a push-pull effect. This study could increase the functionalities of organic push-pull luminophores tremendously.

## 4.5 Conclusion

It is a widely accepted notion that excimers decrease the PLQY of an organic luminophore. However, if the formation equilibrium and relaxation kinetics of excimer-like states can be confined, they can result in PLQY enhancement. In this work, we have synthesized a new TTz based material (EHOPhTTzPy) and showed that it can form excimers in concentrated solution or solution with increased temperature. EHOPhTTzPy was then embedded in various polymer matrices to fabricate films. It was found that excimer-like states in films can be photocontrolled and are highly stable. These excimer-like states are a function of concentration, film fabrication method, rigidity of the polymer matrix, and photoexcitation. By irradiating with light of appropriate energy, the formation of excimer-like states can be controlled with high level of precision which can render films of tunable fluorescence. Confining the excimer-like states in films resulted in highly fluorescent films (PLQY = 61%) and relative increase in PLQY(excimer:monomer) of over 8 folds.  Excimer-like emission can be reversed back to monomeric emission by disaggregating the strongly coupled dimers. We have carried out this disaggregation by annealing the polymer matrix and letting it cure slowly. In doing so, we have fabricated an excimer-like emission-based optical device that can be used for anti-counterfeiting and steganography, among other applications. Since the formation of excimer-like states is a result of the electron-donating and -withdrawing (push-pull) effect, it is reasonable to envision that such high level of photocontrolled excimer-led PLQY enhancement phenomena can also be observed in other similar organic luminophores. Therefore, this study will be crucial in expanding the scope of managing excimer-like states in condensed matter states resulting in the proliferation of a new class of optical and photonic coatings and devices with high luminescence efficiency.

# Chapter 5:

# Conclusion

Efficient management of excitons in organic chromophores in the solid state is a crucial parameter for various optical and photonic applications. However, the neutral electrical charge of an exciton and the excited-state energy continuum bands along which excitons can diffuse in solid-state materials complicates their controlled manipulation. Nevertheless, management of excitons in organic chromophores has been pursued via multiple approaches. In this work, I have utilized self-assembly as a tool to manipulate molecular packing in the solid state. Manipulation of the molecular packing influences the energetics in solid-state materials such as thin films and crystals. The effects of structure-energy modulation have then been traced in the photophysical properties of the organic chromophores via various spectroscopic methods.

Two families of chromophores have been studied in this dissertation: metalloporphyrins and thiazolo[5,4-*d*]thiazole (TTz). Both of these chromophores have been widely reported in the literature and present unique structural and photophysical characteristics which have been utilized in various contexts. Metalloporphyrins are ubiquitous and are even found in nature as chlorophyll and hemoglobin. They exist as a large planar macrocycle with rich $\pi$-conjugation. Metalloporphyrins can form elaborate three dimensional structures along which excitons can diffuse, such as in thylakoids. Porphyrins and metalloporphyrins-based nature-inspired solar cells have been widely reported in the literature. This makes establishing the modulation of excitons in metalloporphyrin films a pressing issue and one that is relevant to a wide spectrum of scientists. TTzs are also planar and highly conjugated. However, unlike metalloporphyrins, these heterocycles prefer $S_1$ to $S_0$ radiative recombination of excitons making them suitable candidates for a variety of fluorescence-based applications. TTzs also boast easy synthetic tunability and high oxidative stability. Thus, TTzs have received significant attention particularly in the last couple of decades with the rise in organic-materials-dependent optical and photonic technologies.

In chapter 2, a new library of solution-processable Zn-(carboalkoxycarbonyl)phenylporphyrins containing butyl ($ZnTCB_4PP$), hexyl ($ZnTCH_4PP$), 2-ethylhexyl ($ZnTCEH_4PP$) and octyl ($ZnTCO_4PP$) alkyl groups was synthesized. It was established that variation in the length of the peripheral alkyl appendages on the metalloporphyrin macrocycle resulted in preferential orientation and molecular self-assembly in solution-processed thin films. The resultant arrangement of molecules consequently affects the electronic and photophysical characteristics of the metalloporphyrin thin films. The various molecular arrangements in the porphyrin thin films and their resultant impact were determined using UV-Vis absorption spectroscopy, steady-state and time-resolved fluorescence spectroscopy, and X-Ray diffractometry. The films were doped with $C_{60}$ exciton quenchers and the change in fluorescence was measured to derive a relative quenching efficiency. Using singlet fluorescence emission decay lifetime, relative quenching efficiency, and $C_{60}$ dopant volume fraction as input, insights on exciton diffusion coefficient and exciton diffusion lengths were obtained from a Monte Carlo simulation. $ZnTCO_4PP$ exhibited the strongest relative fluorescence quenching and therefore the highest exciton diffusion coefficient ($5.29 \text{ x}10^{-3}$ $cm^2$ $s^{-1}$) and longest exciton diffusion length (~ 81 nm). It also showed the strongest out-of-plane stacking among the metalloporphyrins studied. This work demonstrates how molecular self-assembly can be used to modulate and direct exciton diffusion in solution-processable metalloporphyrin thin films engineered for optoelectronic and photonic applications.

In chapter 3, four alkoxyphenyl TTz-based materials were functionalized with alkyl appendages of varying carbon chain lengths. High quality single crystals of the materials were grown, three of which were previously unknown. The crystals were characterized using single-crystal X-ray diffractometry and their molecular-packing modes were studied in conjunction with high-level computational simulation. It was established that the self-assembled molecular arrangements in TTz-based crystals are largely governed by a chorus of synergistic intermolecular non-covalent interactions. Three crystals packed in herringbone mode and one crystal packed in slipped stacks proving that alkyl appendages modulate structural organization in TTz-based materials. The structure-energy effects on the photophysical properties of the TTz-based materials were studied via steady state and time-resolved optical and vibrational spectroscopy. The crystals fluoresce from orange-red to blue spanning through the whole gamut of the visible spectrum. It was established that the photophysical properties are a function of crystal packing in the symmetrically substituted TTz-based materials. This correlation was then utilized to fabricate crystalline blends which can be used for phosphor-converted color-tuning and white-light emission. Given the cost effectiveness, ease of synthesis and now a structure – photophysics correlation, we present a compelling case for the adoption of TTz-based materials in solid-state photonic and fluorescence-based optical devices.

In chapter 4, a widely accepted notion in the photophysics community has been challenged through the controlled self-assembly of 2-(4-(2-ethylhexyl)oxyphenyl)-5-(4-pyridyl)thiazolo[5,4-*d*]thiazole (EHOPhTTzPy) in solution-processable thin films. Since its discovery in the late 1960s, excited-state dimers, or excimers, have been widely understood to plummet the luminescence efficiency (PLQY) of a system. Recently, it has been reported that controlled formation and relaxation kinetics of excimers can result in high PLQY. However, these studies focus on pyrene and other polyaromatic hydrocarbons. In this work, a new TTz based material, EHOPhTTzPy, was synthesized and first tested for successful formation of excimers in the solution state. The formation of excimer-like states was then studied in solution-processable polymer-dye blend films. It was found that the formation of excimer-like states can be photocontrolled. The formation of excimer-like states can also be controlled via modulation of concentration of dye in the polymer-dye blend and by adjusting the film fabrication method. The relaxation kinetics was found to be directly influenced by effective confinement by the neutral polymer matrix. Under effective control over the formation and relaxation kinetics of TTz-based excimer-like states, PLQY of 61% was achieved along with relative increase in PLQY of over a factor of 8 in solution-processable films. PLQY enhancement was found to be observed only in rigid polymer matrices with high Young's modulus. Excimer-like emission can be reversed back to monomeric emission by disaggregating the strongly coupled dimers. The disaggregation was carried out by annealing the polymer matrix and allowing it to cure slowly. This fluorescence-based optical device can be used for anti-counterfeiting and steganography, among other applications. This study will be crucial in expanding the scope of managing excimer-like states in condensed matter states resulting in the proliferation of a new class of optical and photonic coatings and devices with high luminescence efficiency.

The work discussed in this dissertation provides significant insights into the manipulation of exciton behavior in organic chromophores through self-assembly techniques. By influencing molecular packing in the solid state, the energetics and photophysical properties of the chromophores can be effectively controlled, opening up avenues for advanced optical and photonic applications. The successful modulation of exciton diffusion in metalloporphyrin thin films and the establishment of a structure-photophysics correlation in TTz-based materials demonstrate the potential of this approach. Furthermore, the controlled formation and relaxation kinetics of excimer-like states in EHOPhTTzPy films offer a novel route to achieving high luminescence efficiency, paving the way for a new generation of optical and photonic devices. These findings highlight the importance of self-assembly as a powerful tool for tailoring the behavior of excitons in organic chromophores, leading to significant advancements in various fields.

# Appendix A: Supplementary Information (Chapter 2)

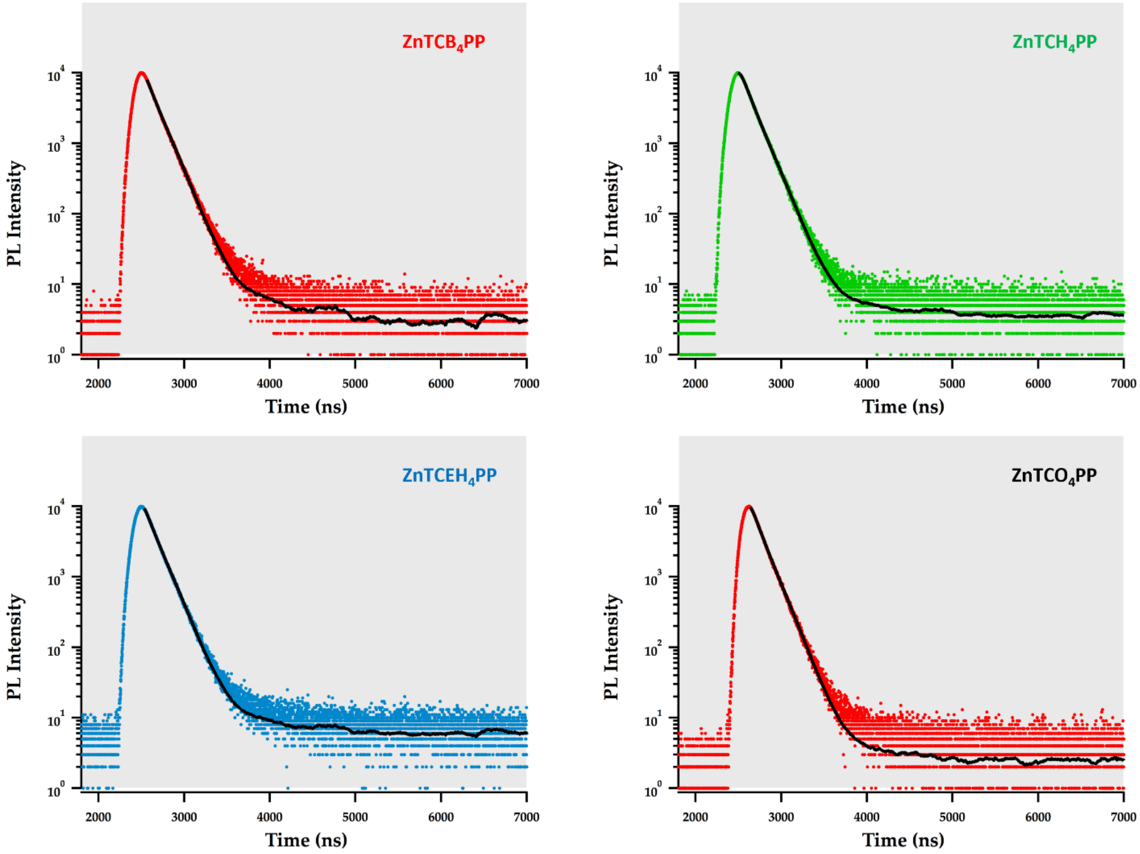

**Figure S2.1.** Time-resolved fluorescence spectra and first order fitting of a) ZnTCB$_4$PP, b) ZnTCH$_4$PP, c) ZnTCEH$_4$PP and d) ZnTCO$_4$PP.

| **Metalloporphyrin** | ZnTCB$_4$PP | ZnTCH$_4$PP | ZnTCEH$_4$PP | ZnTCO$_4$PP |
|---|---|---|---|---|
| **$\tau_{S1}$ (ns)** | 1.89 | 1.89 | 1.89 | 1.85 |

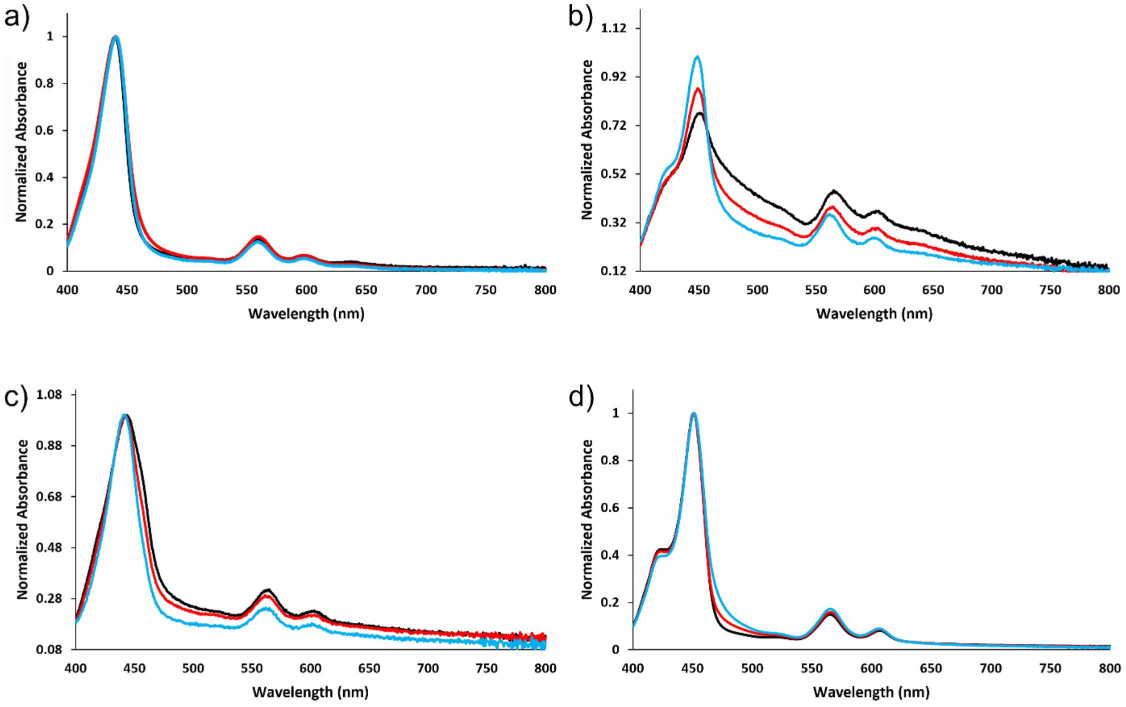

**Figure S2.2.** UV-Vis absorption spectra of spin-cast metalloporphyrins thin films of (a)ZnTCB$_4$PP, (b) ZnTCH$_4$PP, (c) ZnTCEH$_4$PP and (d) ZnTCO$_4$PP. Each plot includes spectra of pristine films (-), films doped with $v_{\text{frac}}$ 0.06% (-) and films doped with $v_{\text{frac}}$ 0.2% (-)

**Table S2.1.** XRD Diffraction Data for ZnTCB$_4$PP, ZnTCH$_4$PP, ZnTCEH$_4$PP and ZnTCO$_4$PP (Cu Kα radiation of λ = 1.541 Å).

| **Material** | **Peak (*2θ*)** | **d-spacing (*Å*)** | **Intensity** | **Rel Intensity** |
|---|---|---|---|---|
| **ZnTCB$_4$PP** | 5.87 | 15.05 | 77 | 0.31 |
| | 13.95 | 6.34 | 122 | 0.49 |
| | 16.81 | 5.27 | 250 | 1.00 |
| | 18.73 | 4.74 | 62 | 0.25 |
| | 25.45 | 3.50 | 57 | 0.23 |
| | | | | |
| **ZnTCH$_4$PP** | 5.51 | 16.03 | 155 | 0.58 |
| | 14.09 | 6.28 | 114 | 0.43 |
| | 16.91 | 5.24 | 265 | 1.00 |
| | 18.43 | 4.81 | 64 | 0.24 |
| | 25.35 | 3.51 | 57 | 0.22 |
| | | | | |
| **ZnTCO$_4$PP** | 4.61 | 19.16 | 365 | 2.97 |
| | 9.21 | 9.60 | 30 | 0.24 |
| | 13.87 | 6.38 | 64 | 0.52 |
| | 16.87 | 5.25 | 123 | 1.00 |
| | 18.45 | 4.81 | 52 | 0.42 |
| | 25.33 | 3.51 | 49 | 0.40 |
| | | | | |
| **ZnTCEH$_4$PP** | 14.07 | 6.29 | 188 | 0.40 |
| | 16.85 | 5.26 | 474 | 1.00 |
| | 18.47 | 4.80 | 87 | 0.18 |
| | 25.57 | 3.48 | 77 | 0.16 |

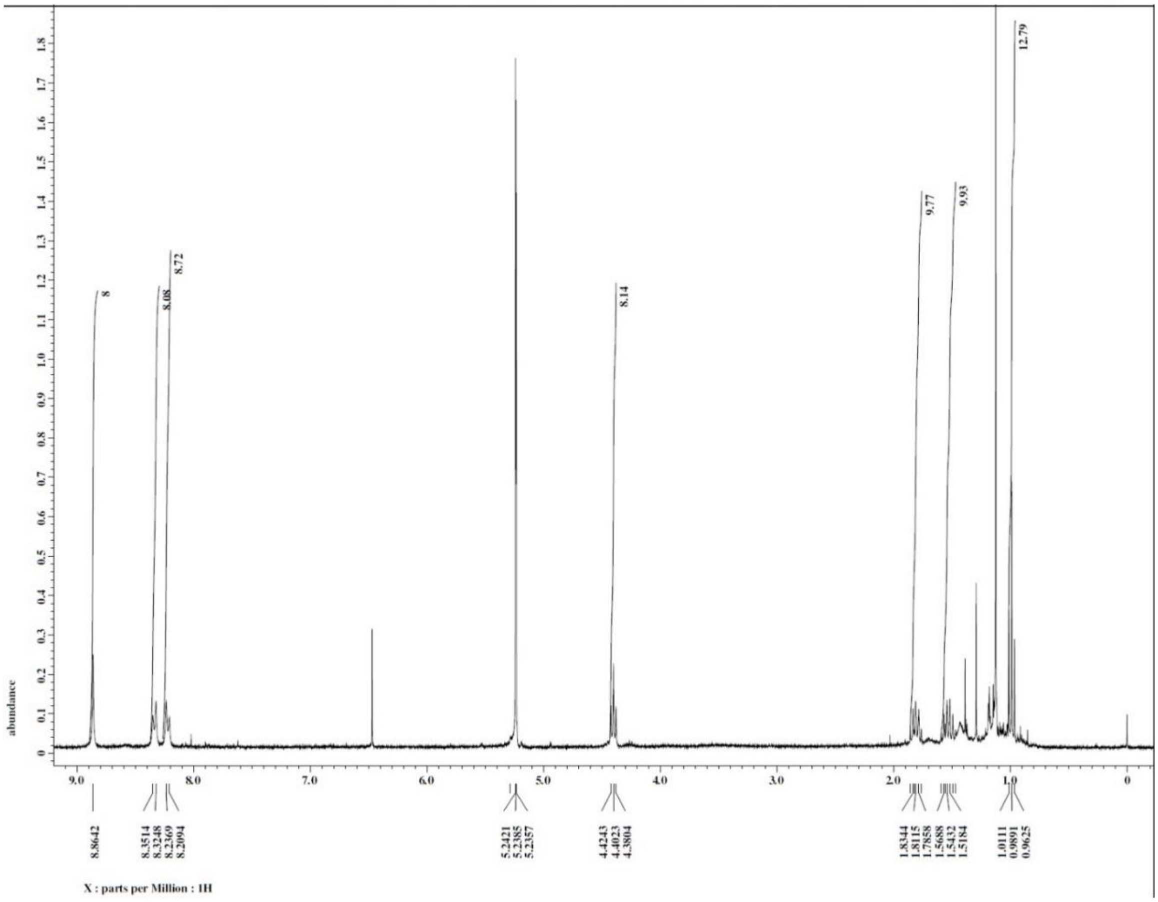

**Figure S2.3.** $^1$H-NMR of ZnTCB$_4$PP

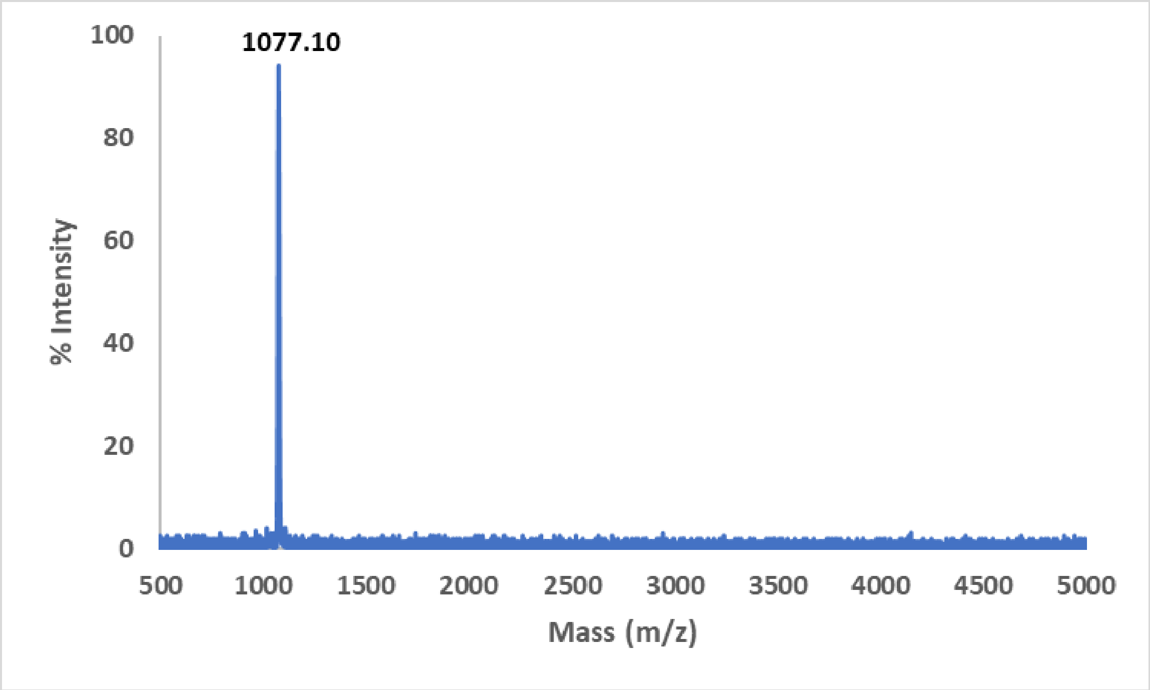

**Figure S2.4.** MALDI-TOF Mass Spectra of $ZnTCB_4PP$

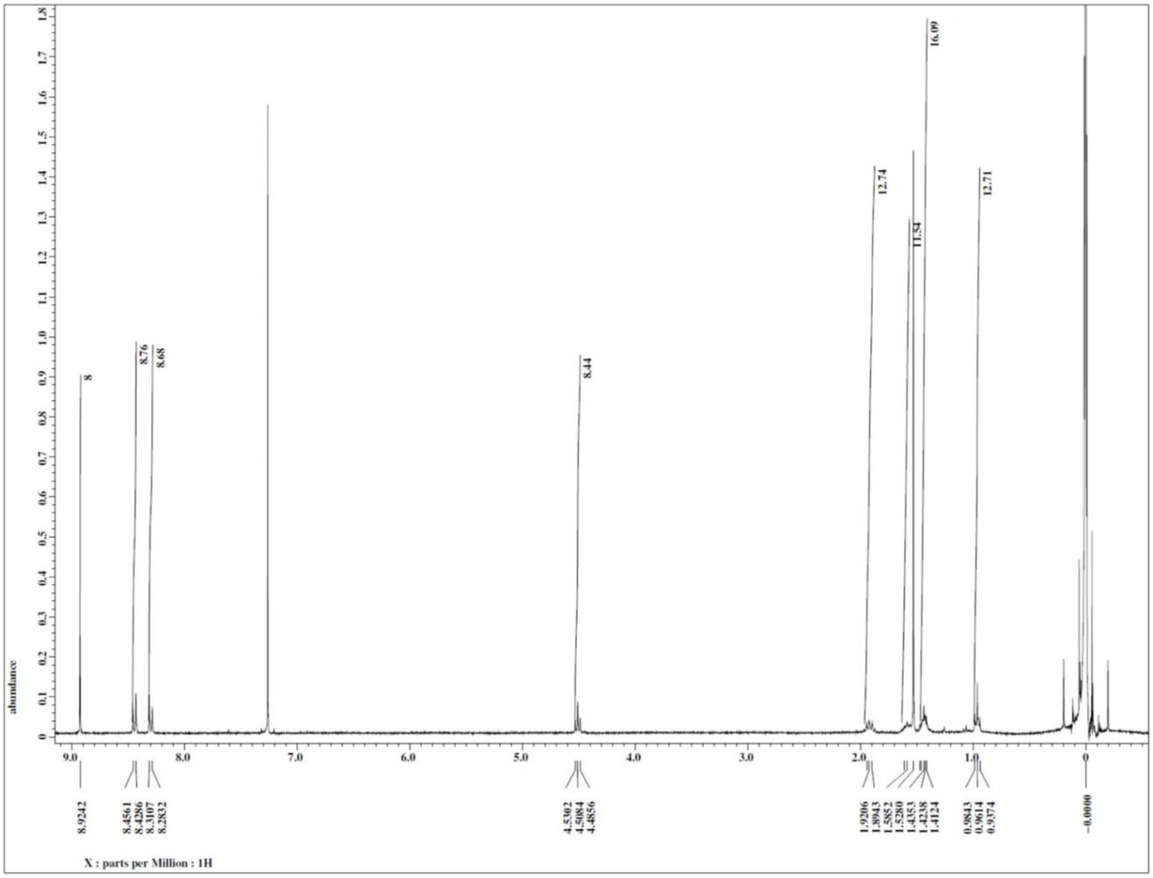

**Figure S2.5.** $^1$H-NMR of $ZnTCH_4PP$

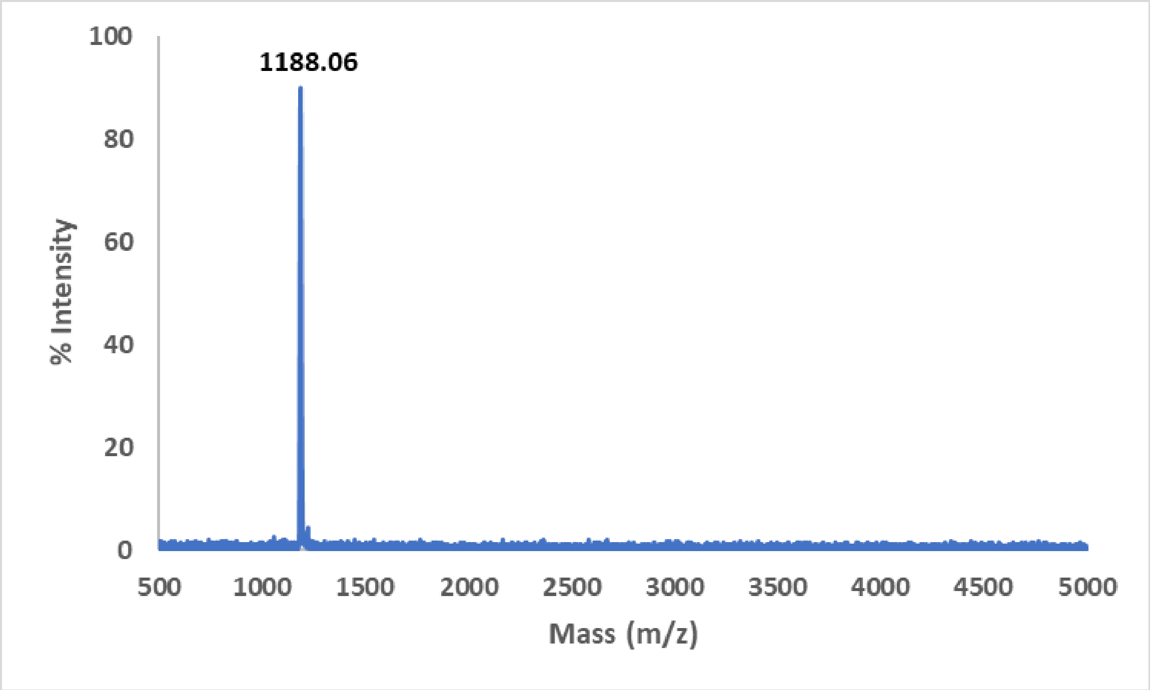

**Figure S2.6.** MALDI-TOF Spectra of $ZnTCH_4PP$

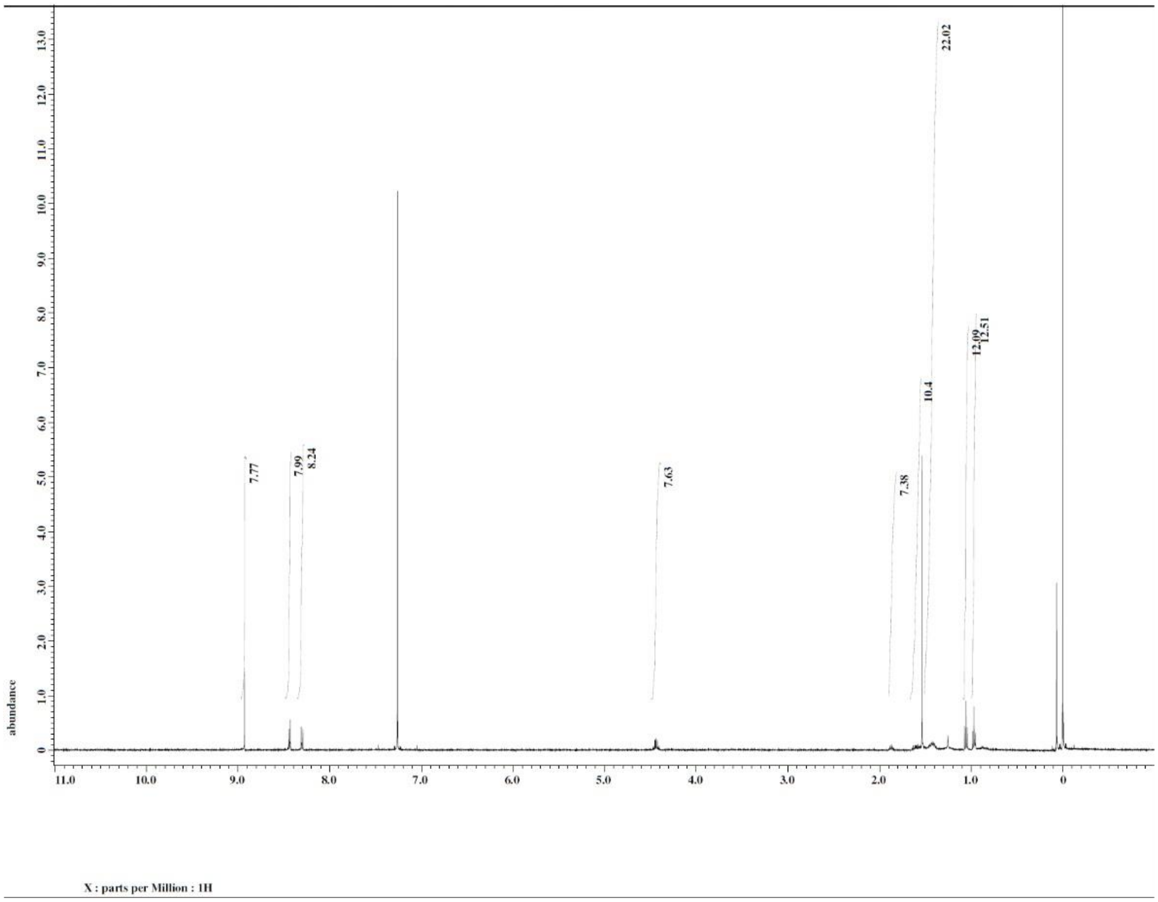

**Figure S2.7.** $^1$H-NMR of ZnTCEH$_4$PP

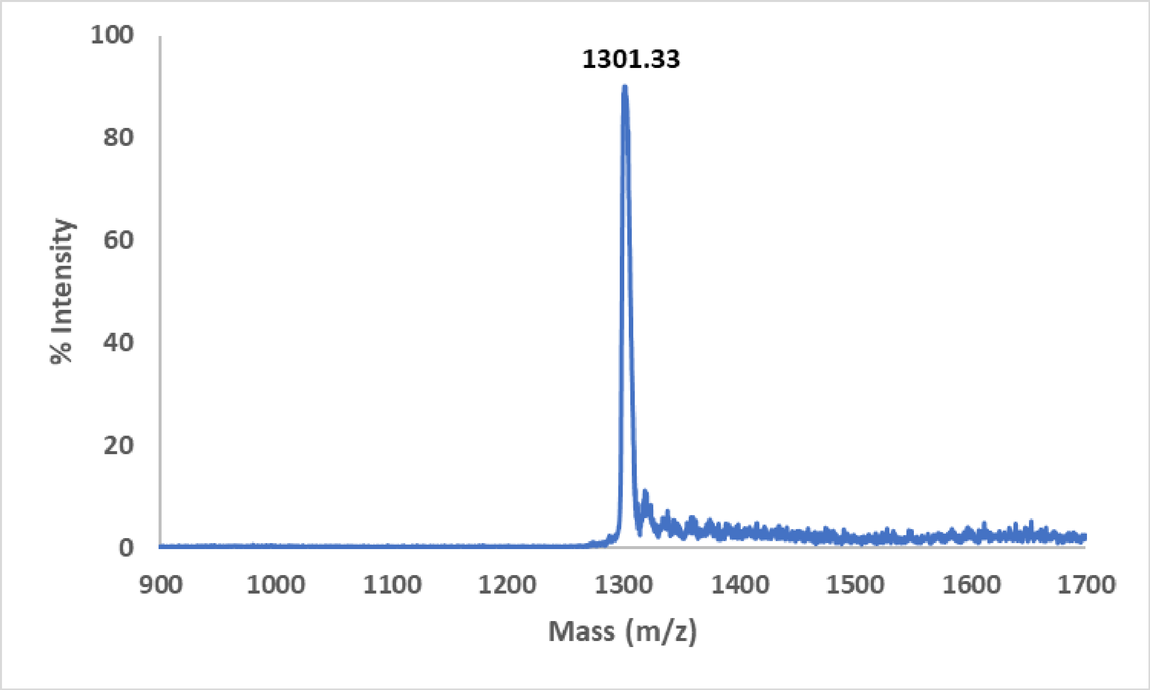

**Figure S2.8.** MALDI-TOF Mass Spectra of $ZnTCEH_4PP$

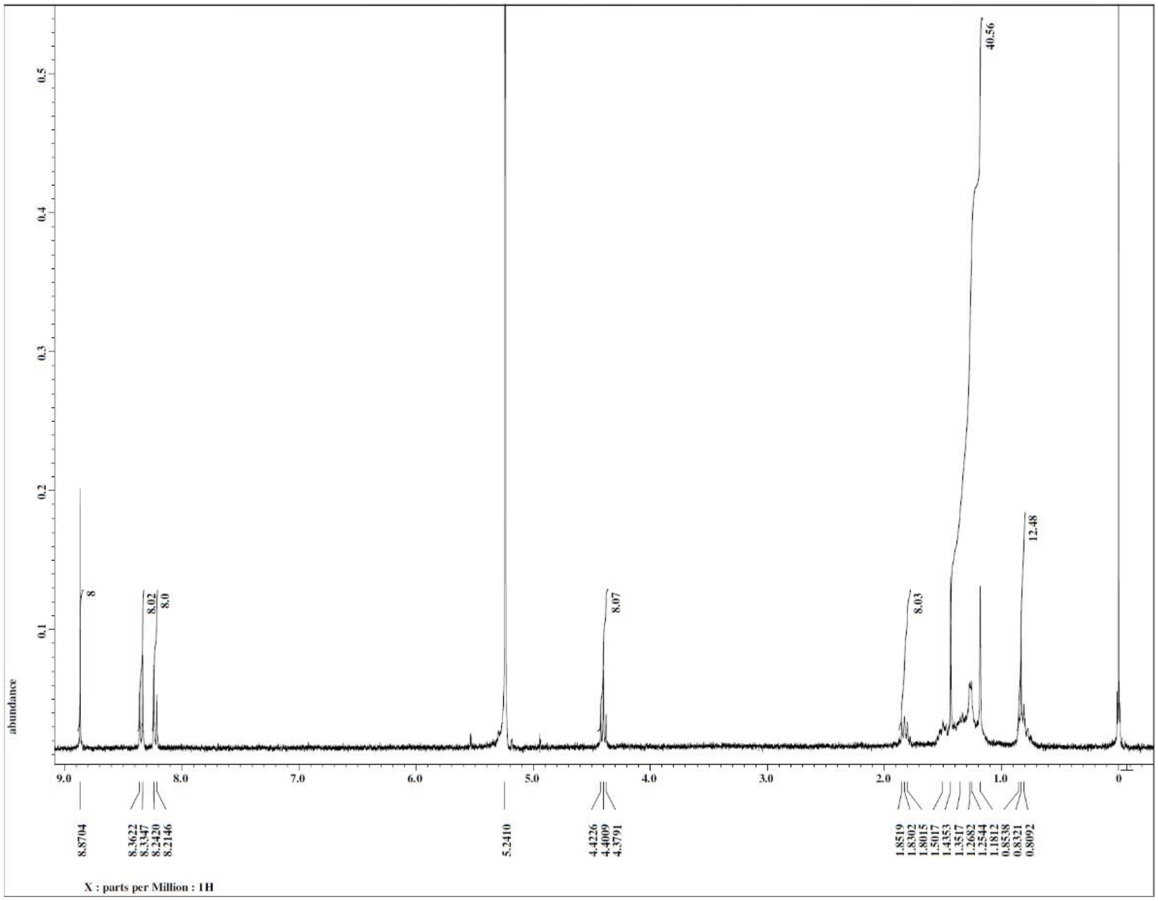

**Figure S2.9.** $^1$H-NMR of ZnTCO$_4$PP

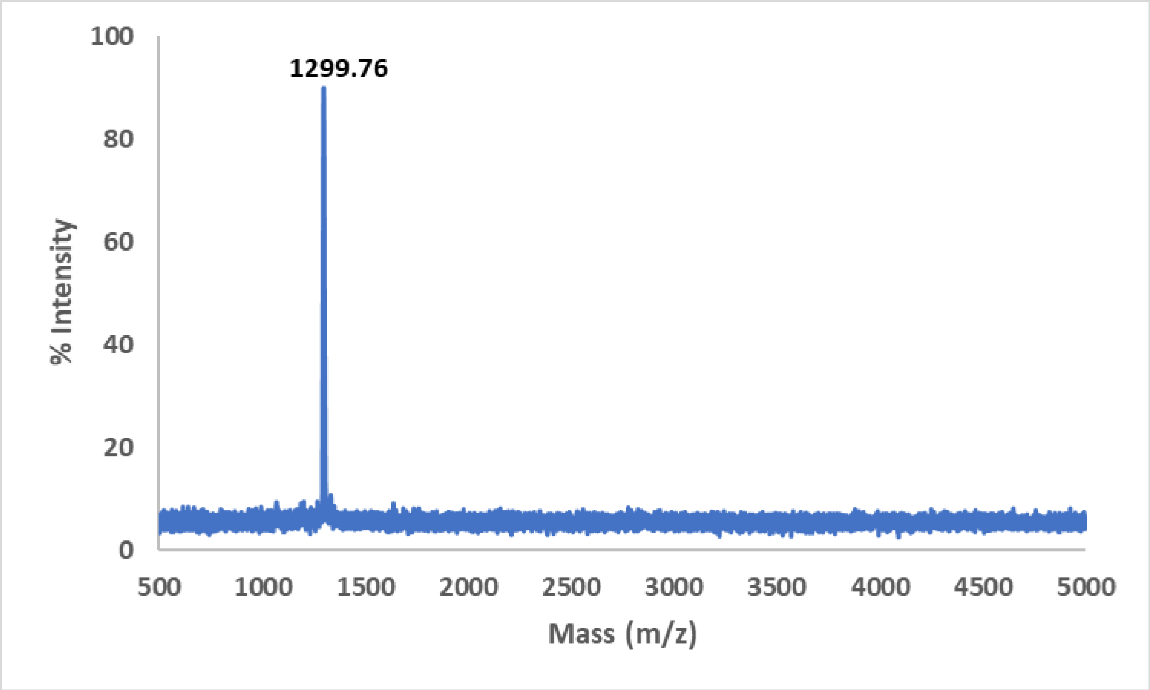

**Figure S2.10.** MALDI-TOF Mass Spectra of $ZnTCO_4PP$

# Appendix B: Supplementary Information (Chapter 3)

## Section3.1: Spectra Characterization

### Section 3.1.1: $^1$*H-NMR Spectra*

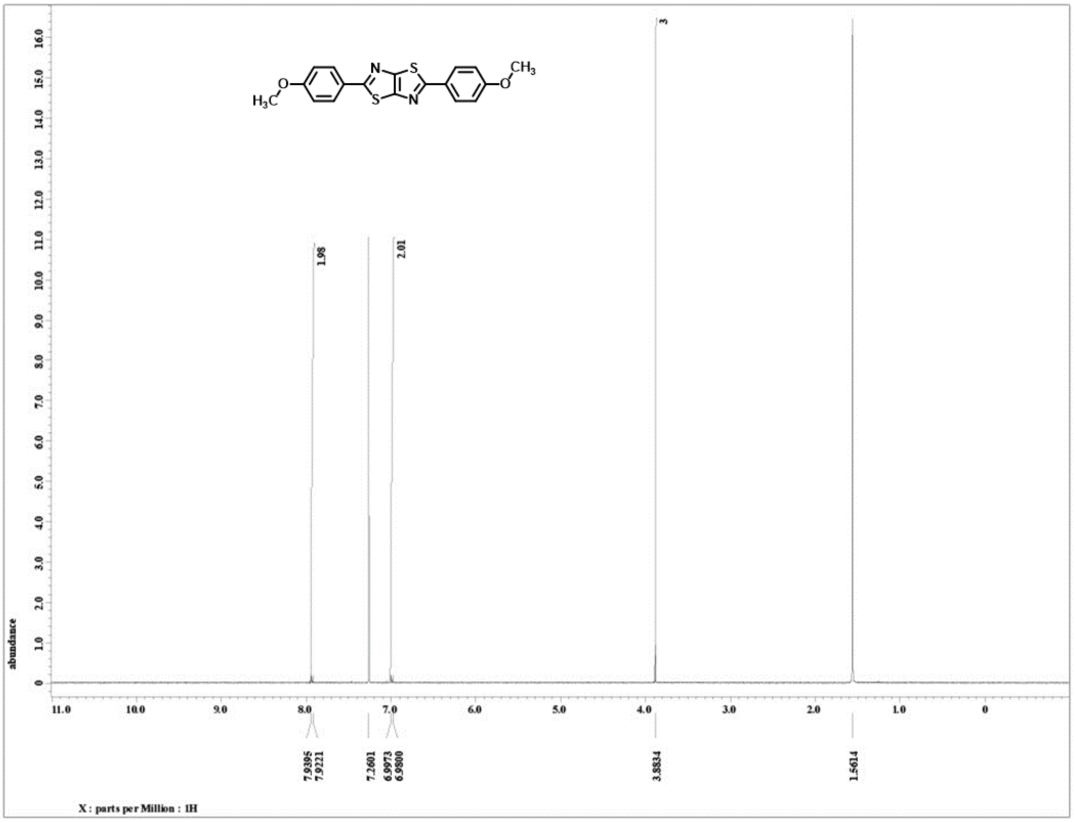

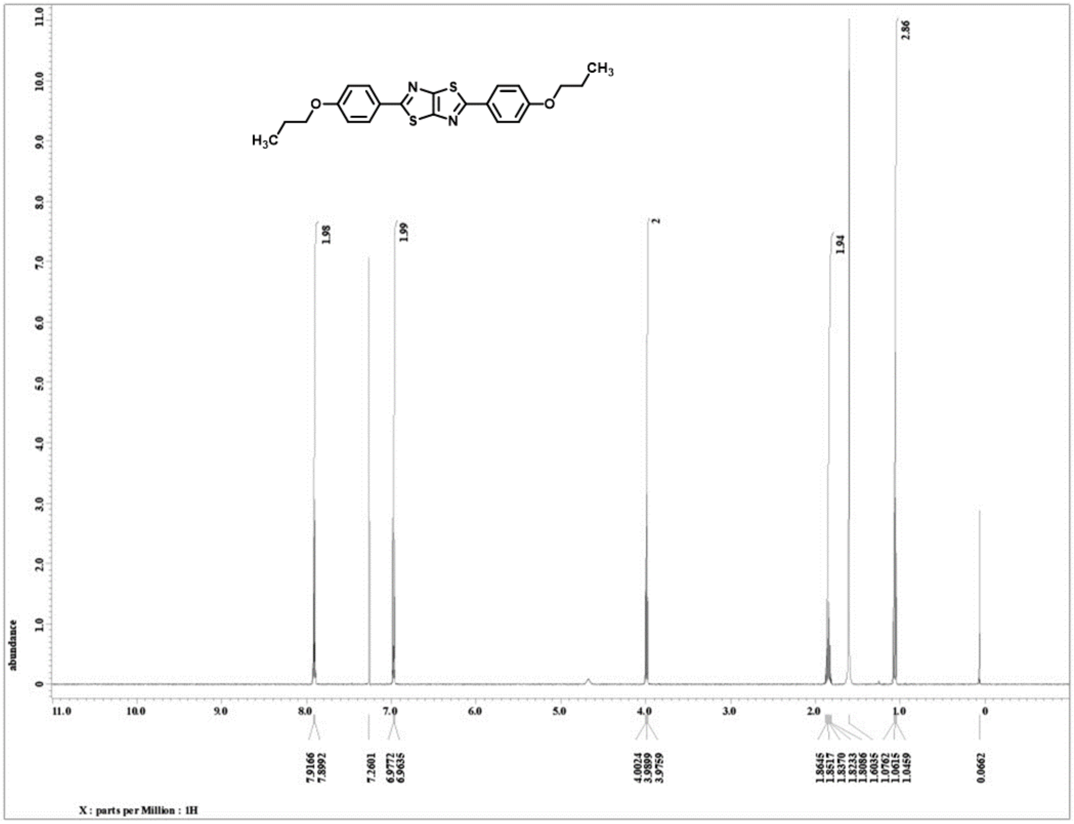
CH3
H3C
O
N
S
abundance
11.0
10.0
9.0
8.0
7.0
6.0
5.0
4.0
3.0
2.0
1.0
0
1.98
1.99
2
1.94
2.86
7.9166
7.8992
7.2601
6.9772
6.9635
4.0024
3.9899
3.9759
1.8645
1.8517
1.8370
1.8233
1.8086
1.6035
1.0762
1.0615
1.0459
0.0662
X : parts per Million : 1H

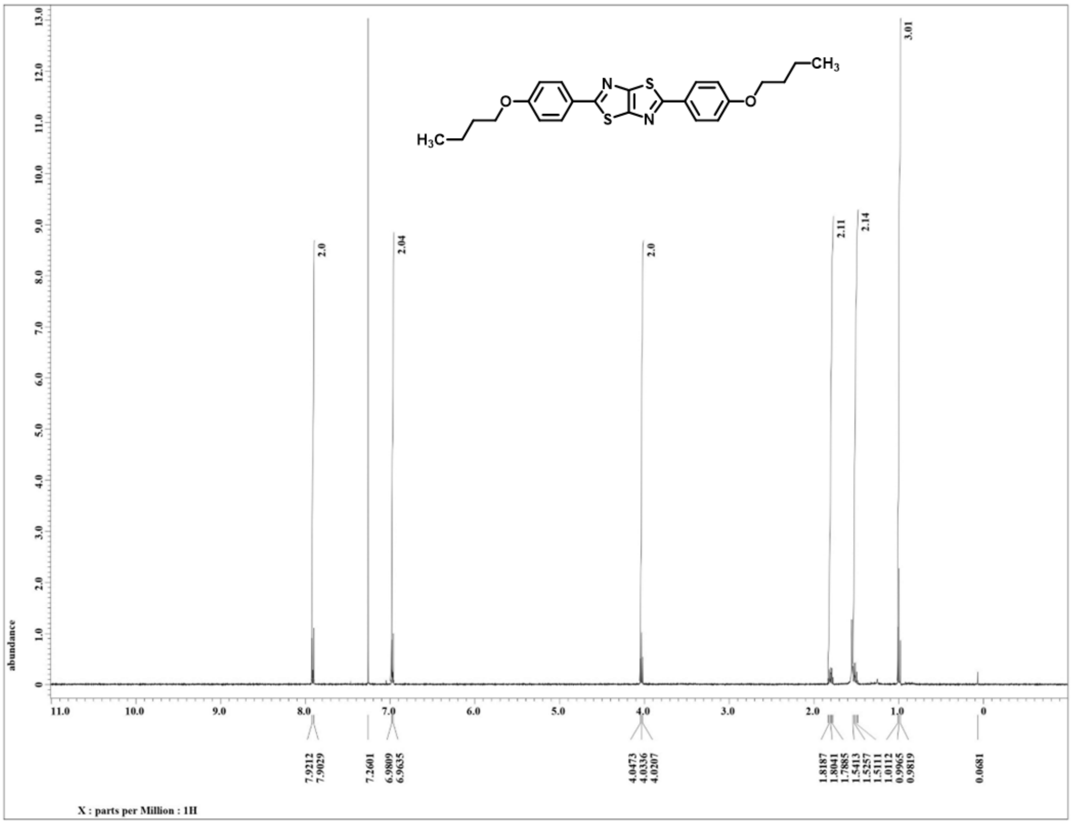
H3C
O
N
S
S
N
O
CH3
abundance
13.0
12.0
11.0
10.0
9.0
8.0
7.0
6.0
5.0
4.0
3.0
2.0
1.0
0
2.0
2.04
2.0
2.11
2.14
3.01
11.0
10.0
9.0
8.0
7.0
6.0
5.0
4.0
3.0
2.0
1.0
0
7.9212
7.9029
7.2601
6.9809
6.9635
4.0473
4.0336
4.0207
1.8187
1.8041
1.7885
1.5413
1.5257
1.5111
1.0112
0.9965
0.9819
0.0681
X : parts per Million : 1H

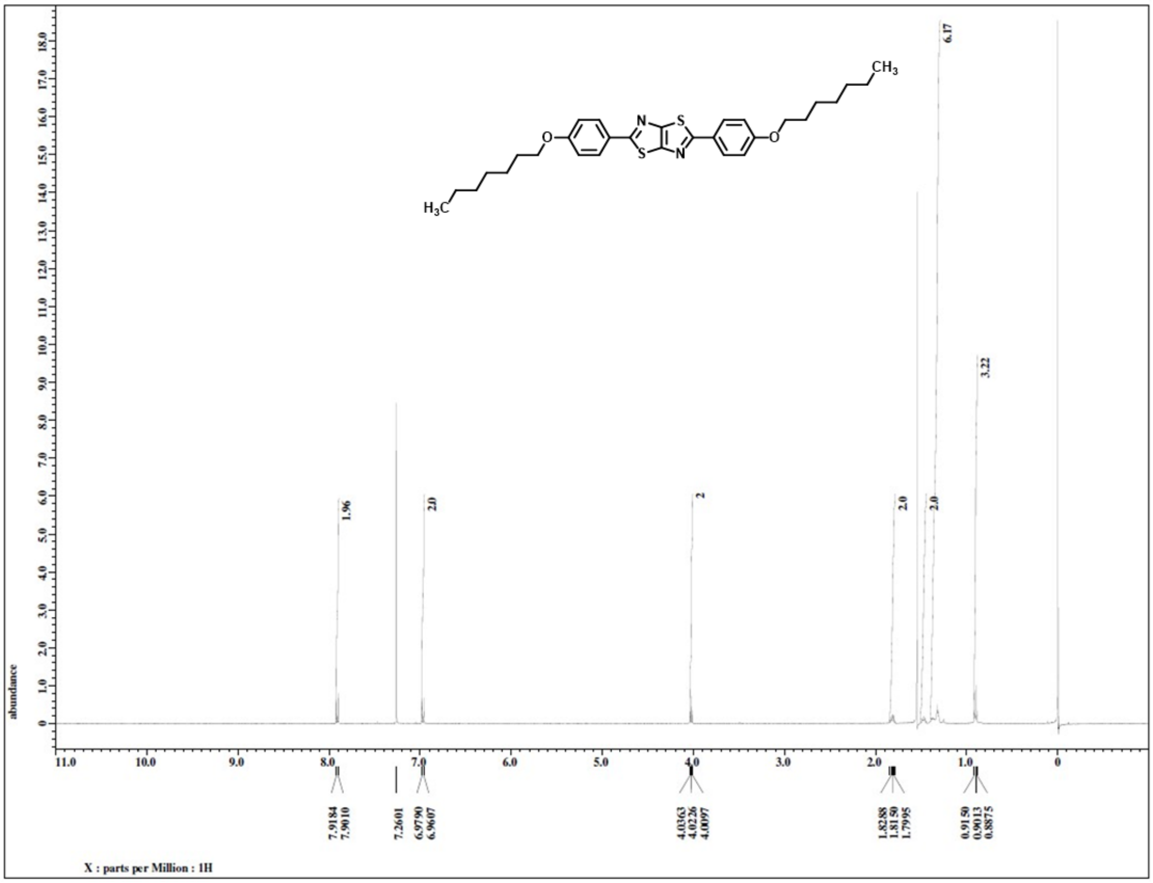
abundance
0
1.0
2.0
3.0
4.0
5.0
6.0
7.0
8.0
9.0
10.0
11.0
12.0
13.0
14.0
15.0
16.0
17.0
18.0
H$_3$C
O
N
S
S
N
O
CH$_3$
1.96
2.0
2
2.0
2.0
6.17
3.22
11.0
10.0
9.0
8.0
7.0
6.0
5.0
4.0
3.0
2.0
1.0
0
7.9184
7.9010
7.2601
6.9790
6.9607
4.0363
4.0226
4.0097
1.8288
1.8150
1.7995
0.9150
0.9013
0.8875
X : parts per Million : 1H

## Section 3.1.2: *MALDI-TOF-MS*

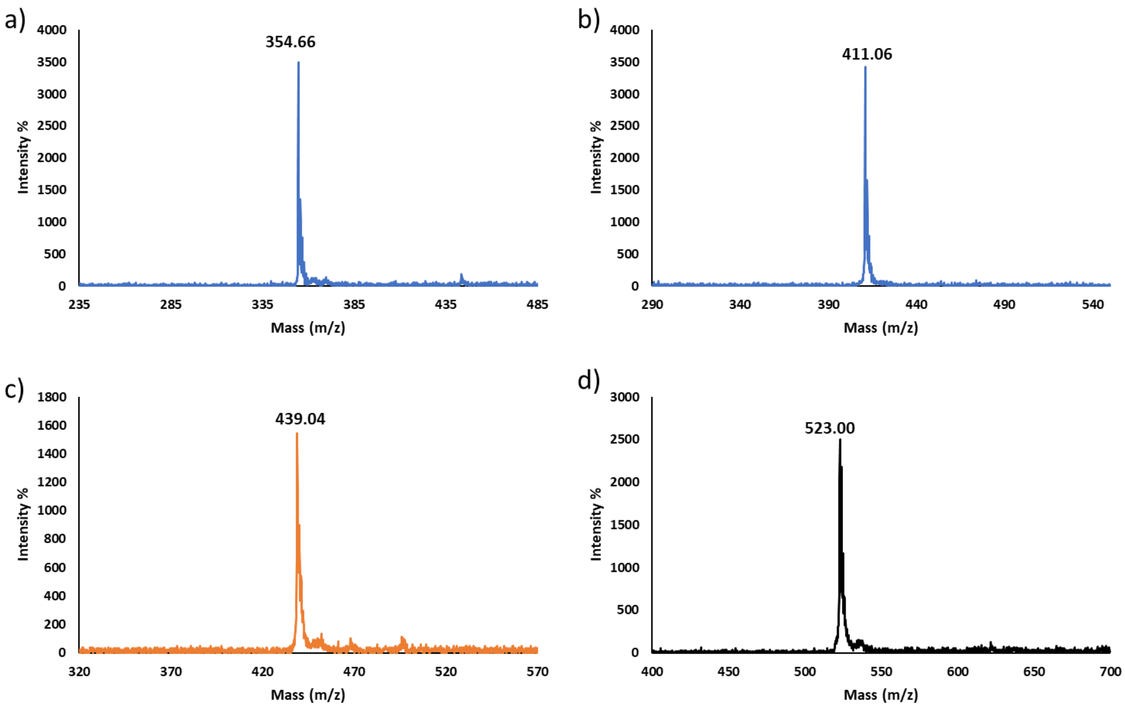

**Figure S3.1.** Maldi-TOF-MS Spectra of a) $(MeOPh)_2TTz$, b) $(PrOPh)_2TTz$, c) $(BuOPh)_2TTz$, and d) $(HepOPh)_2TTz$

## Section 3.2: X-Ray Characterization

### Section 3.2.1: *Single Crystal Structure Data and Refinement*

**Table S3.1.** Summary of crystallographic data of dialkoxyphenyl TTzs

| | **$(PrOPh)_2$TTz** | **$(BuOPh)_2$TTz** | **$(HepOPh)_2$TTz** |
|---|---|---|---|
| **CSD Deposition Number** | **2257069** | **2257068** | **2257067** |
| **Empirical formula** | **$C_{22}H_{22}N_2O_2S_2$** | **$C_{24}H_{26}N_2O_2S_2$** | **$C_{30}H_{38}N_2O_2S_2$** |
| **Formula weight** | **410.564** | **438.618** | **522.781** |
| **Temperature/K** | **100.00(10)** | **100.00(10)** | **100.00(10)** |
| **Crystal system** | **monoclinic** | **triclinic** | **monoclinic** |
| **Space group** | **$P2_1/c$** | **P-1** | **$P2_1/c$** |
| **a/Å** | **16.2976(4)** | **5.4441(5)** | **31.0223(11)** |
| **b/Å** | **7.46099(19)** | **7.4759(7)** | **7.1900(3)** |
| **c/Å** | **7.9920(2)** | **14.1023(13)** | **6.0107(2)** |
| **α/°** | **90** | **84.330(8)** | **90** |
| **β/°** | **96.418(2)** | **82.922(8)** | **91.400(3)** |
| **γ/°** | **90** | **70.044(8)** | **90** |
| **Volume/Å$^3$** | **965.71(4)** | **534.39(9)** | **1340.29(9)** |
| **Z** | **2** | **1** | **2** |
| **$\rho_{calc}$g/cm$^3$** | **1.412** | **1.363** | **1.295** |
| **μ/mm$^{-1}$** | **2.669** | **2.446** | **2.032** |
| **F(000)** | **434.6** | **233.3** | **562.9** |
| **Crystal size/mm$^3$** | **0.378 × 0.364 × 0.197** | **0.565 × 0.511 × 0.036** | **0.165 × 0.141 × 0.035** |
| **Radiation** | **Cu Kα (λ = 1.54184)** | **Cu Kα (λ = 1.54184)** | **Cu Kα (λ = 1.54184)** |
| **2Θ range for data collection/°** | **10.92 to 133.34** | **12.62 to 133.6** | **8.56 to 133.84** |
| **Index ranges** | **$-19 \le h \le 19$, $-7 \le k \le 8$, $-9 \le l \le 8$** | **$-6 \le h \le 5$, $-8 \le k \le 6$, $-16 \le l \le 16$** | **$-36 \le h \le 36$, $-8 \le k \le 7$, $-6 \le l \le 7$** |
| **Reflections collected** | **8742** | **4008** | **12196** |
| **Independent reflections** | **1698 [$R_{int}$ = 0.0335, $R_{sigma}$ = 0.0206]** | **1873 [$R_{int}$ = 0.0374, $R_{sigma}$ = 0.0367]** | **2371 [$R_{int}$ = 0.0772, $R_{sigma}$ = 0.0466]** |
| **Data/restraints/parameters** | **1698/0/141** | **1873/0/137** | **2371/0/176** |

| | | | |
|---|---|---|---|
| **Goodness-of-fit on $F^2$** | **1.075** | **1.075** | **1.103** |
| **Final R indexes [I>=2σ (I)]** | **$R_1$ = 0.0300, $wR_2$ = 0.0733** | **$R_1$ = 0.0366, $wR_2$ = 0.0945** | **$R_1$ = 0.0744, $wR_2$ = 0.2012** |
| **Final R indexes [all data]** | **$R_1$ = 0.0358, $wR_2$ = 0.0780** | **$R_1$ = 0.0431, $wR_2$ = 0.1008** | **$R_1$ = 0.0971, $wR_2$ = 0.2214** |
| **Largest diff. peak/hole / e Å$^{-3}$** | **0.22/-0.28** | **0.40/-0.28** | **0.82/-0.43** |

## Section 3.2.2: *Correlation between Volume of Unit Cell and Alkyl Chain Length*

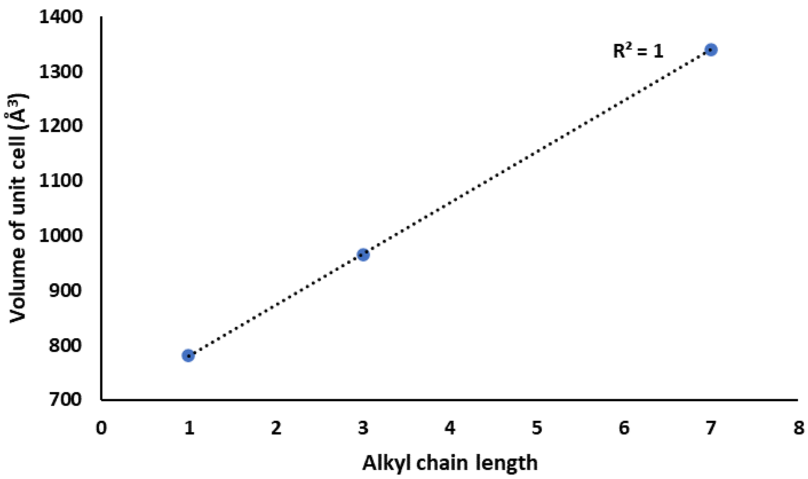

**Figure S3.2.** Crystals packed in monoclinic crystal system showed a perfect correlation between volume of unit cell and alkyl chain length.

### Section 3.2.3: Pictorial representation of interaction energies in TTz crystals

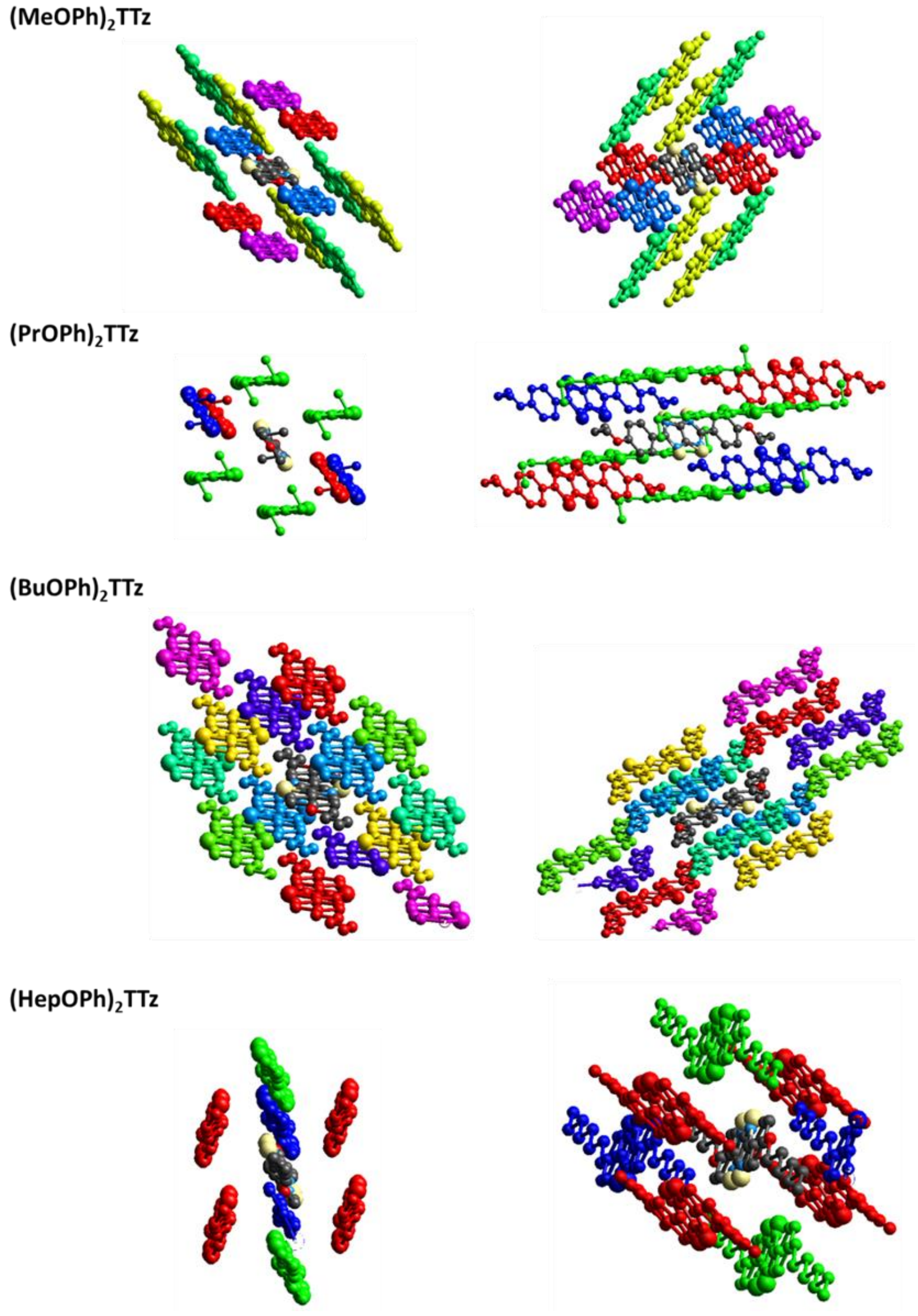

**Figure S3.3.** Color-coded pictorial representation of interaction energy in TTz crystals with respect to one central reference molecule.

## Section 3.2.4: Intermolecular interaction energies in TTz crystals

**Table S3.2.** Details of intermolecular interaction energies in TTz crystals

| | Pair label (*cf* Fig 3) | Orientation | Color | N | R (Å) | $E_{ele}$ | $E_{pol}$ | $E_{dis}$ | $E_{rep}$ | $E_{tot}$ |
|---|---|---|---|---|---|---|---|---|---|---|
| (MeOPh)$_2$TTz | a) | Cofacial | Red | 2 | 3.98 | -6.98 | -2.44 | -80.74 | 36.34 | -53.70 |
| | b) | Orthogonal | Green | 4 | 10.67 | -11.73 | -1.48 | -25.69 | 14.28 | -24.60 |
| | c) | Parallel | Blue | 2 | 19.04 | -7.82 | -1.18 | -8.80 | 0.00 | -17.90 |
| | d) | Orthogonal | Yellow | 4 | 11.47 | -5.60 | -0.89 | -16.03 | 6.30 | -16.20 |
| | | Cofacial | Purple | 2 | 18.52 | 3.28 | -0.37 | -5.75 | 0.00 | -2.80 |
| (PrOPh)$_2$TTz | e) | Orthogonal | Green | 4 | 5.47 | -54.65 | -7.03 | -101.65 | 93.75 | -69.70 |
| | f) | Cofacial | Blue | 2 | 7.99 | -28.12 | -5.25 | -58.62 | 75.52 | -16.60 |
| | g) | Cofacial | Red | 2 | 18.94 | -0.11 | -0.07 | -8.97 | 0.00 | -9.20 |
| (BuOPh)$_2$TTz | h) | Cofacial | Red | 2 | 15.29 | -11.20 | -1.41 | -58.53 | 0.00 | -71.10 |
| | | Cofacial | Blue | 2 | 14.1 | 1.16 | -1.70 | -68.29 | 0.00 | -68.80 |
| | | Cofacial | Green | 2 | 15.96 | -29.81 | -1.26 | -27.35 | 0.00 | -58.50 |
| | | Cofacial | Teal | 2 | 14.48 | -10.36 | -2.00 | -33.01 | 0.00 | -45.40 |
| | | Cofacial | Yellow | 2 | 5.44 | -10.36 | -5.25 | -44.68 | 22.93 | -37.40 |
| | | Cofacial | Purple | 2 | 28.46 | 0.85 | 0.00 | -4.88 | 0.00 | -4.00 |
| | | Cofacial | Pink | 2 | 28.8 | 0.11 | 0.00 | -0.70 | 0.00 | -0.60 |

| | | | | | | | | | | |
|---|---|---|---|---|---|---|---|---|---|---|
| **(HepOPh)$_2$TTz** | **i)** | **Orthogonal** | **Red** | **4** | **4.69** | **-72.51** | **0.00** | **-137.88** | **99.37** | **-111.00** |
| | **j)** | **Cofacial** | **Green** | **2** | **6.01** | **-79.06** | **-7.62** | **-78.39** | **110.44** | **-54.70** |
| | | **Cofacial** | **Blue** | **2** | **33.54** | **0.21** | **0.00** | **-7.06** | **0.00** | **-6.80** |

$E_{tot}$ kJ/mol=$E_{ele}$ kJ/mol + $E_{pol}$ kJ/mol + $E_{dis}$ kJ/mol + $E_{rep}$ kJ/mol

Where,

$E_{ele}$ = classical electrostatic energy of interaction between monomer charge distributions

$E_{rep}$ = exchange–repulsion energy

$E_{dis}$ = dispersion energy

$E_{pol}$ = Polarization energy

Since $k_BT$ = 2.5 kJ/mol and the error to which the sublimation enthalpy can be measured is approximately 5 kJ/mol for organic compounds, molecular pairs with $E_{tot} \sim 5$ kJ/mol should be ignored.

## Section 3.2.5: List of contacts from crystal packing data of $(C_nOPh)_2TTz$ crystals

**Table S3.3.** $(C_nOPh)_2TTz$ crystal packing data with emphasis on interchromophoric interactions. For atom labelling sequence *cf.* Figure S3.4. Interatomic distances has been denoted by *d* (Å); Frequency of Interaction has been denoted by *I*; Number of molecules has been denoted by *M*.

| | **Pair label (*cf* Fig 3)** | **Orientation** | **Color** | **Interaction** | ***d*, (Å)** | **Angle, (deg)** | ***I*** | ***M*** | **Total** |
|---|---|---|---|---|---|---|---|---|---|
| **$(MeOPh)_2TTz$** | **a)** | **Cofacial** | **Red** | **$C_9$-H—$O_1$** | **2.935** | **149.48** | **2** | **2** | **4** |
| | | | | **$\pi$-$\pi_{\text{phenyl centroid}}$** | **3.985** | | **2** | **2** | **4** |
| | **b)** | **Orthogonal** | **Green** | **$C_5$-H—$S_1$** | **3.519** | **120.35** | **1** | **4** | **4** |
| | | | | **$C_5$-H—$N_1$** | **2.964** | **178.48** | **1** | **4** | **4** |
| | | | | **$C_9$—$S_1$** | **3.468** | **173.66** | **1** | **4** | **4** |
| | **c)** | | **Yellow** | **$C_9$-H—$N_1$** | **2.912** | **161.62** | **1** | **4** | **4** |
| | | | | **$C_7$-H—$S_1$** | **3.851** | **169.5** | **1** | **4** | **4** |
| | **d)** | **Parallel** | **Blue** | **$C_9$-H—$O_1$** | **2.537** | **144.74** | **2** | **2** | **4** |
| **$(PrOPh)_2TTz$** | **e)** | **Orthogonal** | **Green** | **$C_8$-H—$S_1$** | **3.839** | | **1** | **4** | **4** |
| | | | | **$C_{10}$-H—$O_1$** | **3.249** | **127.93** | **1** | **4** | **4** |
| | | | | **$C_{11}$-H—$O_1$** | **3.44** | **122.36** | **1** | **4** | **4** |
| | | | | **$C_{10}$-H—$O_1$** | **3.922** | **135.47** | **1** | **4** | **4** |
| | | | | **$C_2$—$S_1$** | **3.38** | | **1** | **4** | **4** |
| | | | | **S—S** | **3.488** | | **1** | **4** | **4** |

| | | | | | | | | | |
|---|---|---|---|---|---|---|---|---|---|
| | | | | **$C_7$-H—$C_3$** | **2.88** | **136.06** | **1** | **4** | **4** |
| | | | | **$S_1$—$C_3$** | **3.327** | | **1** | **4** | **4** |
| | | | | **$C_4$—$S_1$** | **3.379** | | **1** | **4** | **4** |
| | **f)** | **Cofacial** | **Blue** | **$C_7$-H—$N_1$** | **3.35** | **126.41** | **2** | **2** | **4** |
| | | | | **$C_9$-H—$N_1$** | **2.986** | **72.88** | **2** | **2** | **4** |
| | | | | **$C_8$—$S_1$** | **3.456** | | **2** | **2** | **4** |
| | **g)** | **Cofacial** | **Red** | **$C_{11}$-H—$O_1$** | **3.799** | **142.93** | **2** | **2** | **4** |
| **$(BuOPh)_2TTz$** | **h)** | **Cofacial** | **Red** | **$C_{12}$-H—$S_1$** | **3.266** | **123.54** | **2** | **14** | **28** |
| | | | | **$C_9$-H—$O_1$** | **3.321** | **124.83** | **2** | **14** | **28** |
| | | | | **$C_{12}$-H—$N_1$** | **3.255** | **170.66** | **2** | **14** | **28** |
| | | | | **$C_{10}$-H—$\pi_{\text{phenyl centroid}}$** | **2.856** | **138.1** | **2** | **14** | **28** |
| | | | | **$C_{11}$-H—$\pi_{\text{phenyl centroid}}$** | **3.591** | | **2** | **14** | **28** |
| | | | | **$C_{12}$-H—$TTz_{\text{centroid}}$** | **3.601** | **142.8** | **2** | **14** | **28** |
| **$(HepOPh)_2TTz$** | **i)** | **Orthogonal** | **Red** | **$C_{10}$-H—$O_1$** | **3.11** | **141.73** | **1** | **4** | **4** |
| | | | | **$C_5$-H—$O_1$** | **3.893** | **147.75** | **1** | **4** | **4** |
| | | | | **$C_{11}$-H—$O_1$** | **3.519** | **131.74** | **1** | **4** | **4** |
| | | | | **$C_9$-H—$O_1$** | **3.016** | **144.94** | **1** | **4** | **4** |
| | | | | **$C_4$-H—$S_1$** | **3.599** | **123.69** | **1** | **4** | **4** |
| | | | | **$C_7$-H—$C_6$** | **2.826** | **124.37** | **1** | **4** | **4** |
| | | | | **$S_1$—$C_2$** | **3.311** | | **1** | **4** | **4** |

| | | | | | | | | | |
|---|---|---|---|---|---|---|---|---|---|
| | | | | **$S_1$—$C_1$** | **3.392** | | **1** | **4** | **4** |
| | | | | **$C_4$-H—$C_3$** | **2.895** | **124.17** | **1** | **4** | **4** |
| | | | | **$C_4$-H—$C_2$** | **2.892** | **144.2** | **1** | **4** | **4** |
| | **j)** | **Cofacial** | **Green** | **$C_{11}$-H—O1** | **3.062** | **170.29** | **2** | **2** | **4** |
| | | | | **$C_7$-H—H-$C_9$** | **2.345** | **157.81** | **2** | **2** | **4** |
| | | | | **S—S** | **3.118** | | **1** | **2** | **2** |

## Section 3.2.6: Atom labelling sequence

**The atom labelling sequence of $(HepOPh)_2TTz$ is shown in Figure S3.3. Truncated labelling sequence can be used for other TTz derivatives.**

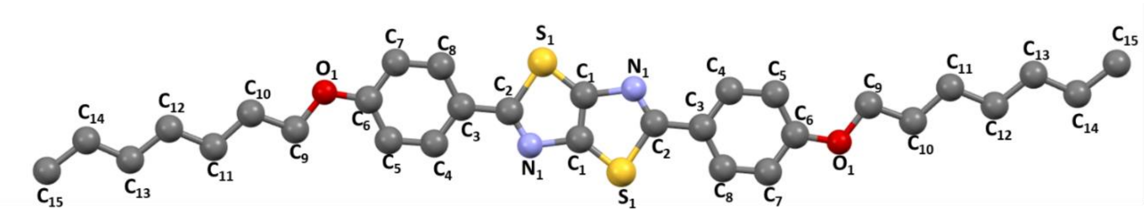

**Figure S3.4.** $(HepOPh)_2TTz$ with labelled non-hydrogen atoms.

## Section 3.2.7: Distribution of intermolecular contacts to Hirshfeld surface area

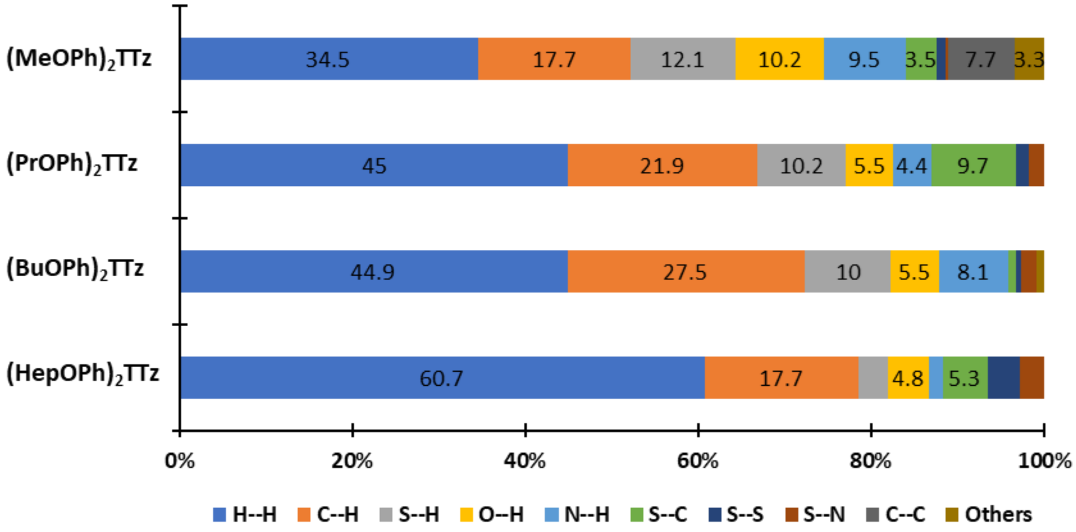

**Figure S3.5.** Relative contribution of the intermolecular contacts to the Hirshfeld surface area for (CnOPh)2TTz crystals.

### Section 3.2.8: Shape index of the Hirshfeld surfaces

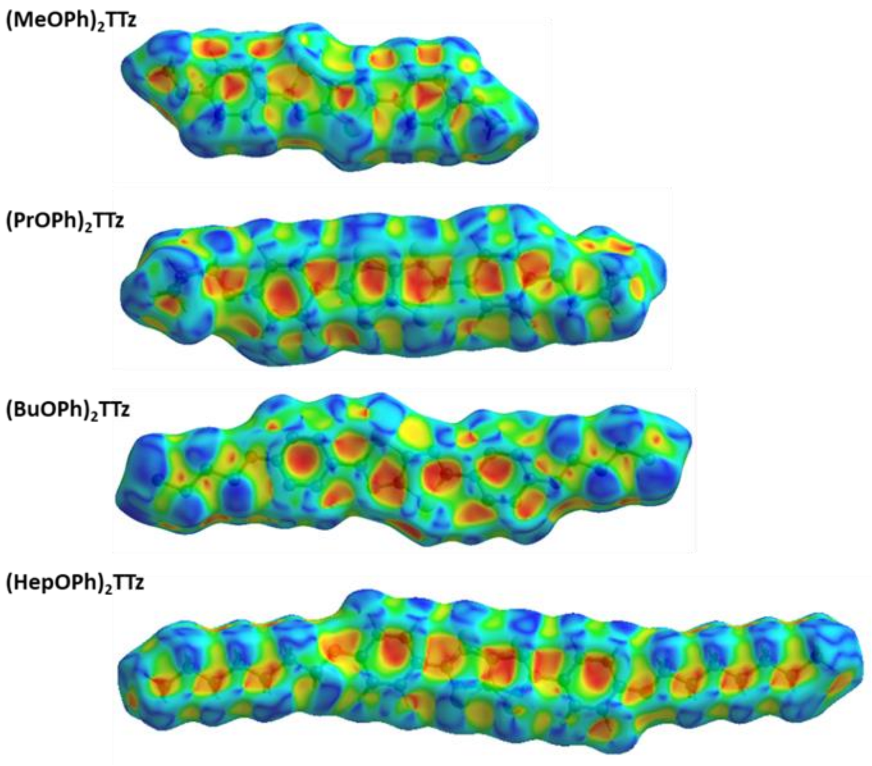

**Figure S3.6.** Shape index of the Hirshfeld surfaces of the $(C_nOPh)_2TTz$ crystals. π- π orbital overlap is represented by adjacent red and blue triangles on the Hirshfeld surface. The absence of adjacent red and blue triangles is indicative of lack of π- π orbital overlap.[119]

## Section 3.2.9: *Powder X-Ray Diffractograms of TTz Crystals*

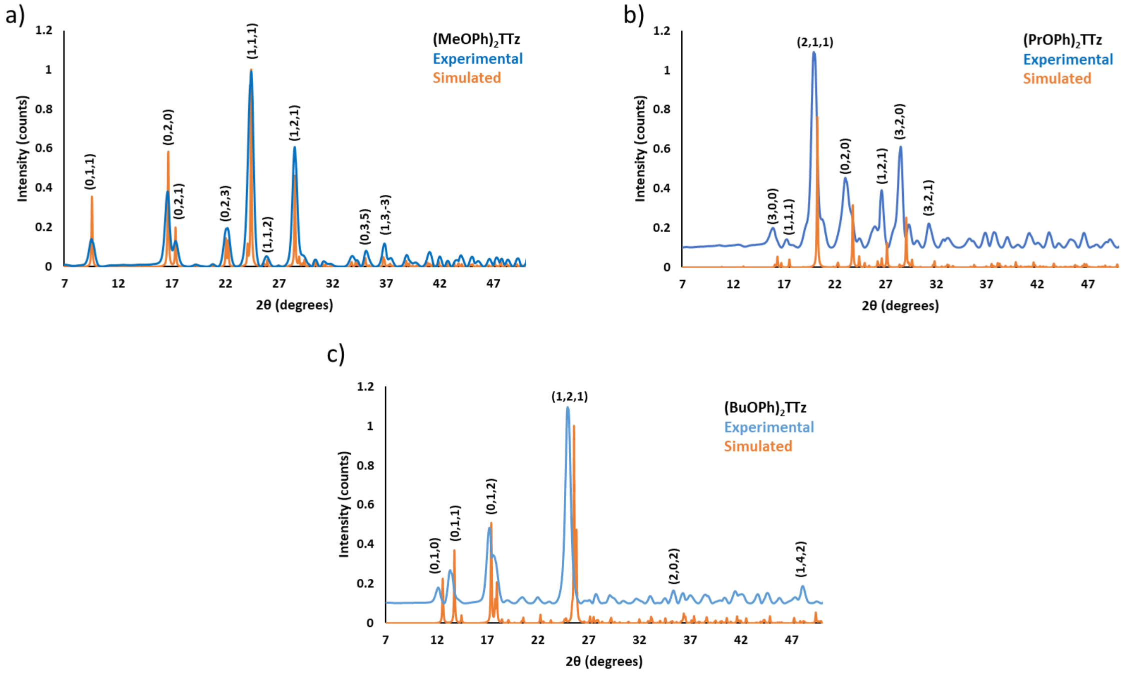

**Figure S3.7.** Comparison of experimental and simulated powder XRD patterns of a) $(MeOPh)_2TTz$, b) $(PrOPh)_2TTz$, c) $(BuOPh)_2TTz$.

## Section 3.3: Photophysical Characterization

### Section 3.3.1: DFT Simulated Raman Spectra

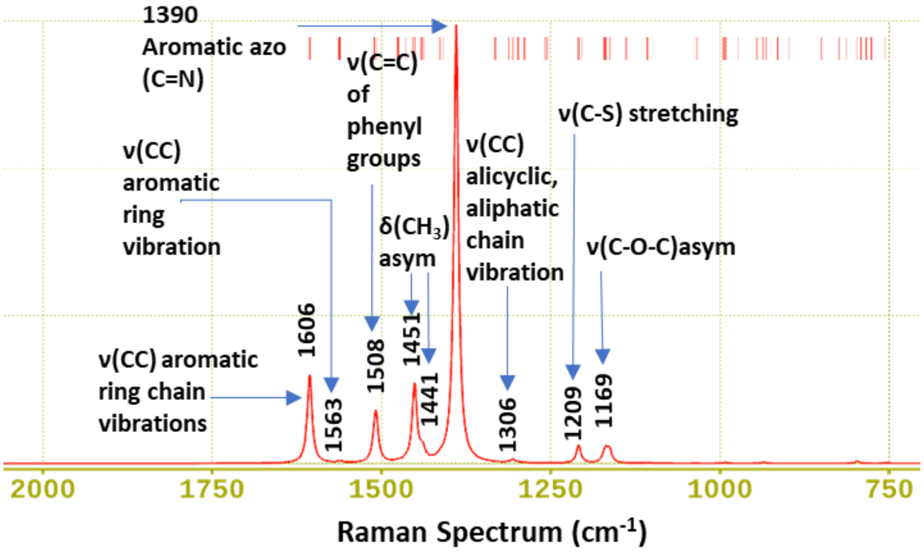

**Figure S3.8.** DFT Simulated Raman Spectra with peak assignments.

### Section 3.3.2: Lattice-Phonon Raman Spectra of TTz Crystals

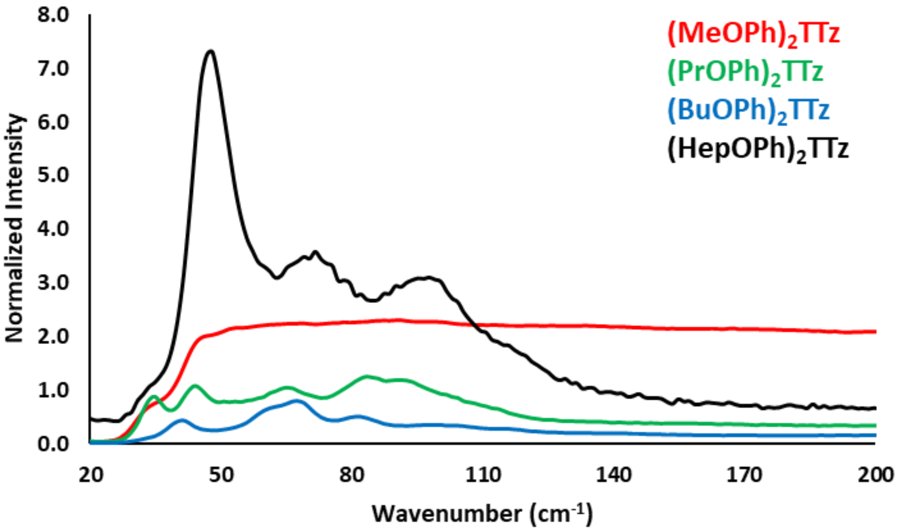

**Figure S3.9.** Lattice-Phonon Raman Spectra of TTz Crystals.

### Section 3.3.3: *Time Dependent Photostability Measurement of TTz Crystals*

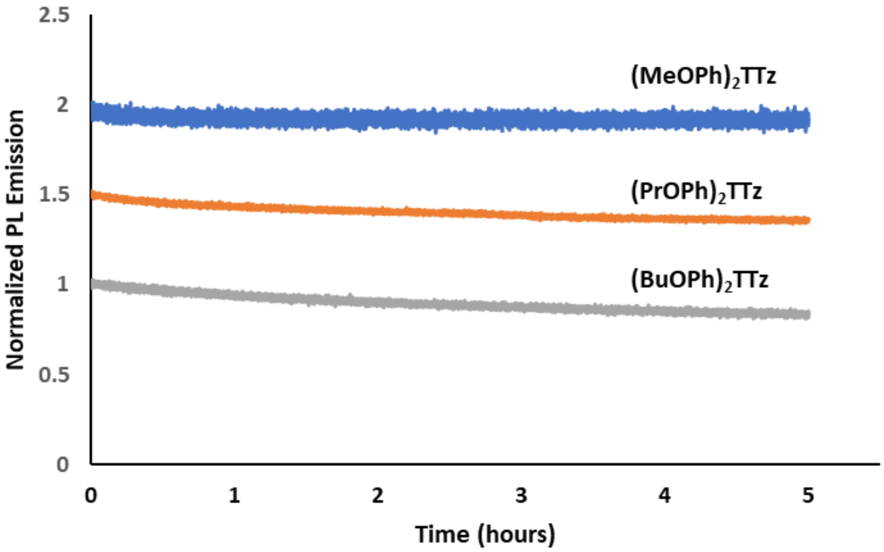

**Figure S3.10.** Time dependent photostability measurement of TTz Crystals under constant illumination by 400 nm in ambient conditions.

| **Material** | **Decrease in PL Intensity after 5 hours of illumination** |
|---|---|
| **(MeOPh)$_2$TTz** | **8 %** |
| **(PrOPh)$_2$TTz** | **14 %** |
| **(BuOPh)$_2$TTz** | **15 %** |

# Appendix C: Supplementary Information (Chapter 4)

## 4.6.1 $^1$H-NMR of EHOPhTTzPy

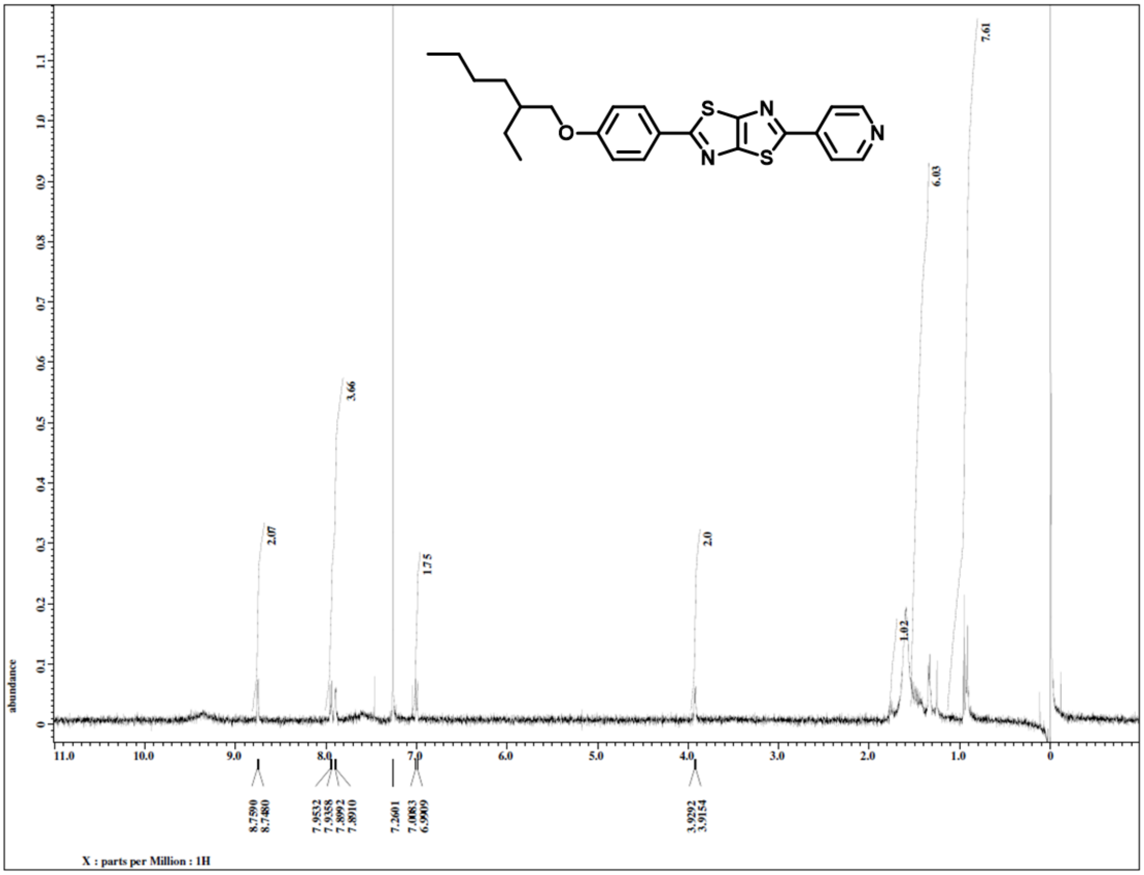

**Figure S4.1.** 1H-NMR Spectra of EHOPhTTzPy

### 4.6.2 MALDI-TOF MS of EHOPhTTzPy

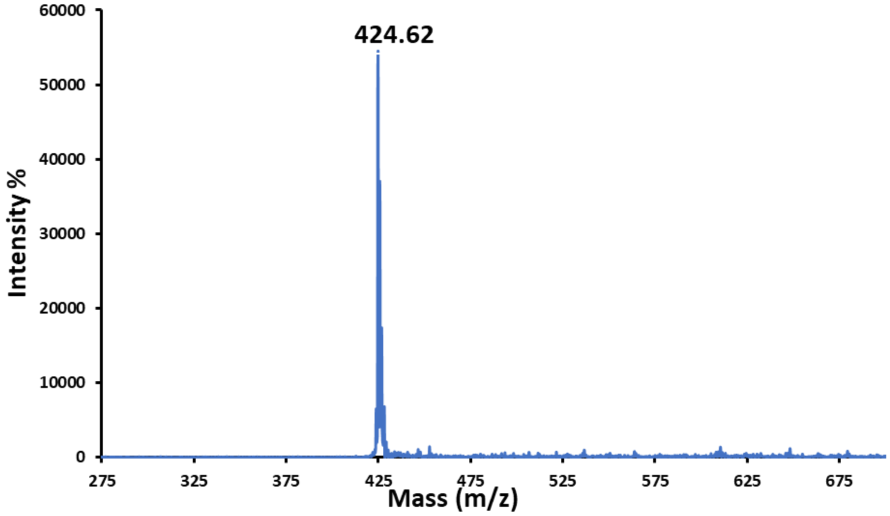

**Figure S4.2.** MALDI-TOF-MS Spectra of EHOPhTTzPy

### 4.6.3 Solvatofluorochromic Characteristics of EHOPhTTzPy

**Table S4.1.** Optical spectrophotometric details of EHOPhTTzPy in different solvents.

| **Solvent** | **λab (nm)** | **ε (M.cm)$^{-1}$** | **λem (nm)** | **$\Phi_{Fl}$** | **τ(ns)** | **$k_r = \Phi/\tau$** | **$k_{nr}=(1 - \Phi)/\tau$** |
|---|---|---|---|---|---|---|---|
| **Toluene** | 372 | 1766.4 | 436 | 0.99 | 0.762 | $1.30\text{x}10^{9}$ | $1.31\text{x}10^{7}$ |
| **Chloroform** | 372 | 419.54 | 442 | 0.99 | 1.125 | $8.80\text{x}10^{8}$ | $8.89\text{x}10^{6}$ |
| **Ethanol** | 372 | 7238.5 | 457 | 0.94 | 1.79 | $5.25\text{x}10^{8}$ | $3.35\text{x}10^{7}$ |
| **Methanol** | 372 | 38062 | 461 | 0.78 | 1.902 | $4.10\text{x}10^{8}$ | $1.16\text{x}10^{8}$ |

### 4.6.4 PL emission spectra of the LED sources

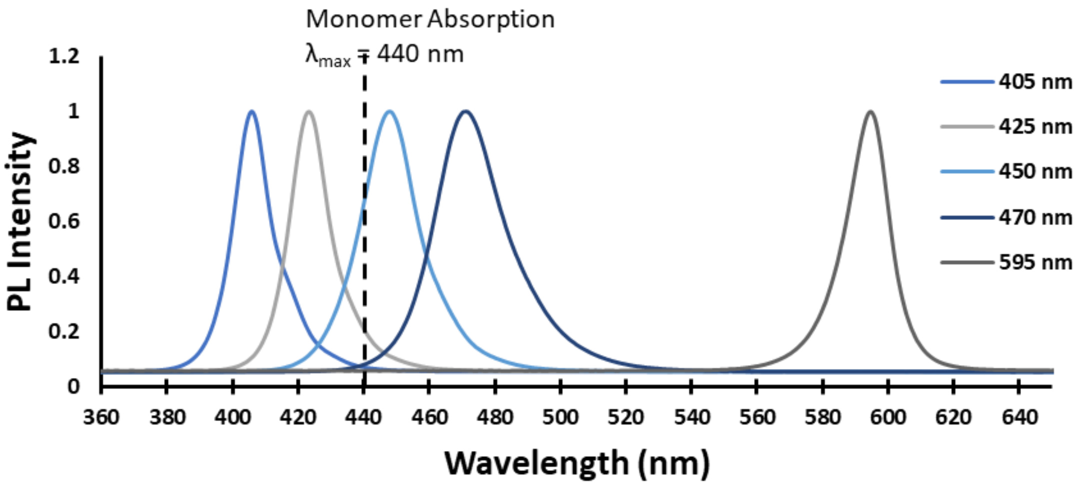

**Figure S4.3. PL emission spectra of the LED sources**

# References

1. P. Cudazzo, F. Sottile, A. Rubio and M. Gatti, *J Phys Condens Matter*, 2015, **27**, 113204.
2. M. Knupfer, *Applied Physics A*, 2003, **77**, 623-626.
3. L. Zhu, Z. Wei and Y. Yi, *The Journal of Physical Chemistry C*, 2021, **126**, 14-21.
4. C. J. Bardeen, *Annu Rev Phys Chem*, 2014, **65**, 127-148.
5. G. G. Macfarlane, T. P. McLean, J. E. Quarrington and V. Roberts, *Journal of Physics and Chemistry of Solids*, 1959, **8**, 388-392.
6. Z. Wang and C. Wang, *Adv Mater*, 2021, **33**, e2005819.
7. K. Feron, W. J. Belcher, C. J. Fell and P. C. Dastoor, *Int J Mol Sci*, 2012, **13**, 17019-17047.
8. X. H. Jin, M. B. Price, J. R. Finnegan, C. E. Boott, J. M. Richter, A. Rao, S. M. Menke, R. H. Friend, G. R. Whittell and I. Manners, *Science*, 2018, **360**, 897-900.
9. A. J. Sneyd, T. Fukui, D. Palecek, S. Prodhan, I. Wagner, Y. Zhang, J. Sung, S. M. Collins, T. J. A. Slater, Z. Andaji-Garmaroudi, L. R. MacFarlane, J. D. Garcia-Hernandez, L. Wang, G. R. Whittell, J. M. Hodgkiss, K. Chen, D. Beljonne, I. Manners, R. H. Friend and A. Rao, *Sci Adv*, 2021, **7**, eabh4232.
10. J. Bauri, R. B. Choudhary and G. Mandal, *Journal of Materials Science*, 2021, **56**, 18837-18866.
11. A. Salehi, X. Fu, D. H. Shin and F. So, *Advanced Functional Materials*, 2019, **29**, 1808803.
12. S. M. Menke, W. A. Luhman and R. J. Holmes, *Nat Mater*, 2013, **12**, 152-157.
13. T. Kinuta, T. Sato, N. Tajima, R. Kuroda, Y. Matsubara and Y. Imai, *Journal of Molecular Structure*, 2010, **982**, 45-49.
14. N. S. S. Kumar, S. Varghese, C. H. Suresh, N. P. Rath and S. Das, *The Journal of Physical Chemistry C*, 2009, **113**, 11927-11935.
15. S. Varghese and S. Das, *J Phys Chem Lett*, 2011, **2**, 863-873.
16. Y. Fan, Q. Li and Z. Li, *Materials Chemistry Frontiers*, 2021, **5**, 1525-1540.
17. E. Rabinowitch, *The Journal of Physical Chemistry*, 1957, **61**, 870-878.
18. G. S. Engel, T. R. Calhoun, E. L. Read, T. K. Ahn, T. Mancal, Y. C. Cheng, R. E. Blankenship and G. R. Fleming, *Nature*, 2007, **446**, 782-786.
19. D. I. G. Bennett, G. R. Fleming and K. Amarnath, *Proc Natl Acad Sci U S A*, 2018, **115**, E9523-E9531.
20. T. Fujita, J. C. Brookes, S. K. Saikin and A. Aspuru-Guzik, *J Phys Chem Lett*, 2012, **3**, 2357-2361.
21. L. Jin, S. Lv, Y. Miao, D. Liu and F. Song, *ChemCatChem*, 2021, **13**, 140-152.
22. Y. Matsuo, K. Ogumi, I. Jeon, H. Wang and T. Nakagawa, *RSC Adv*, 2020, **10**, 32678-32689.
23. M. K. Panda, K. Ladomenou and A. G. Coutsolelos, *Coordination Chemistry Reviews*, 2012, **256**, 2601-2627.
24. N. Soudi, S. Nanayakkara, N. M. Jahed and S. Naahidi, *Solar Energy*, 2020, **208**, 31-45.
25. M. G. Walter, A. B. Rudine and C. C. Wamser, *Journal of Porphyrins and Phthalocyanines*, 2010, **14**, 759-792.
26. L. L. Li and E. W. Diau, *Chem Soc Rev*, 2013, **42**, 291-304.
27. A. Mahmood, J.-Y. Hu, B. Xiao, A. Tang, X. Wang and E. Zhou, *Journal of Materials Chemistry A*, 2018, **6**, 16769-16797.
28. J. Min Park, J. H. Lee and W.-D. Jang, *Coordination Chemistry Reviews*, 2020, **407**, 213157.
29. G. Lin, H. Ding, R. Chen, Z. Peng, B. Wang and C. Wang, *J Am Chem Soc*, 2017, **139**, 8705-8709.

30. I. Roy, S. Goswami, R. M. Young, I. Schlesinger, M. R. Mian, A. E. Enciso, X. Zhang, J. E. Hornick, O. K. Farha, M. R. Wasielewski, J. T. Hupp and J. F. Stoddart, *J Am Chem Soc*, 2021, **143**, 5053-5059.
31. J. Chen, Y. Zhu and S. Kaskel, *Angew Chem Int Ed Engl*, 2021, **60**, 5010-5035.
32. F. C. da Silva, L. P. Rosa, I. M. de Jesus, G. P. de Oliveira Santos, N. M. Inada, K. C. Blanco, T. S. D. Araujo and V. S. Bagnato, *Lasers Med Sci*, 2022, **37**, 1227-1234.
33. M. Ekrami, G. Magna, Z. Emam-Djomeh, M. Saeed Yarmand, R. Paolesse and C. Di Natale, *Sensors (Basel)*, 2018, **18**.
34. T. Sun, Z. Zhang, J. Xu, L. Liang, C.-L. Mai, L. Ren, Q. Zhou, Y. Yu, B. Zhang and P. Gao, *Dyes and Pigments*, 2021, **193**, 109469.
35. M. Kaushal, A. L. Ortiz, J. A. Kassel, N. Hall, T. D. Lee, G. Singh and M. G. Walter, *Journal of Materials Chemistry C*, 2016, **4**, 5602-5609.
36. T. Ghosh, L. Gerbig, M. Lambov, M. Dechant and M. Lehmann, *Journal of Materials Chemistry C*, 2020, **8**, 5562-5571.
37. C. R. Martin, K. C. Park, R. E. Corkill, P. Kittikhunnatham, G. A. Leith, A. Mathur, S. L. Abiodun, A. B. Greytak and N. B. Shustova, *Faraday Discuss*, 2021, **231**, 266-280.
38. S. Matsubara and H. Tamiaki, *Journal of Photochemistry and Photobiology C: Photochemistry Reviews*, 2020, 100385.
39. G. Magna, D. Monti, C. Di Natale, R. Paolesse and M. Stefanelli, *Molecules*, 2019, **24**, 4307.
40. A. L. Ortiz, G. S. Collier, D. M. Marin, J. A. Kassel, R. J. Ivins, N. G. Grubich and M. G. Walter, *Journal of Materials Chemistry C*, 2015, **3**, 1243-1249.
41. M. T. Sajjad, A. Ruseckas and I. D. Samuel, *Matter*, 2020, **3**, 341-354.
42. J. Otsuki, *Journal of Materials Chemistry A*, 2018, **6**, 6710-6753.
43. O. V. Mikhnenko, H. Azimi, M. Scharber, M. Morana, P. W. M. Blom and M. A. Loi, *Energy & Environmental Science*, 2012, **5**, 6960-6965.
44. A. Huijser, T. J. Savenije, A. Kotlewski, S. J. Picken and L. D. Siebbeles, *Advanced materials*, 2006, **18**, 2234-2239.
45. M. G. Walter, C. C. Wamser, J. Ruwitch, Y. Zhao, D. Braden, M. Stevens, A. Denman, R. Pi, A. Rudine and P. J. Pessiki, *Journal of Porphyrins and Phthalocyanines*, 2007, **11**, 601-612.
46. L. E. de Sousa, F. T. Bueno, L. Ribeiro, L. A. Ribeiro Junior, D. A. da Silva Filho and P. H. de Oliveira Neto, *Chemistry of Materials*, 2019, **31**, 6818-6823.
47. B. A. L. Raul, Y. N. Luponosov, W. Yang, N. M. Surin, O. Douheret, J. Min, T. L. C. Jansen, S. A. Ponomarenko and M. S. Pshenichnikov, *Sci Rep*, 2020, **10**, 21198.
48. D. Rai, J. S. Bangsund, J. G. Barriocanal and R. J. Holmes, *Journal of Materials Chemistry C*, 2020, **8**, 6118-6123.
49. O. V. Mikhnenko, M. Kuik, J. Lin, N. van der Kaap, T. Q. Nguyen and P. W. Blom, *Adv Mater*, 2014, **26**, 1912-1917.
50. O. V. Mikhnenko, J. Lin, Y. Shu, J. E. Anthony, P. W. Blom, T. Q. Nguyen and M. A. Loi, *Phys Chem Chem Phys*, 2012, **14**, 14196-14201.
51. A. Zieleniewska, F. Lodermeyer, A. Roth and D. M. Guldi, *Chem Soc Rev*, 2018, **47**, 702-714.
52. Y. Long, G. J. Hedley, A. Ruseckas, M. Chowdhury, T. Roland, L. A. Serrano, G. Cooke and I. D. W. Samuel, *ACS Appl Mater Interfaces*, 2017, **9**, 14945-14952.
53. M. T. Sajjad, A. J. Ward, C. Kastner, A. Ruseckas, H. Hoppe and I. D. Samuel, *J Phys Chem Lett*, 2015, **6**, 3054-3060.
54. B. Siegmund, M. T. Sajjad, J. Widmer, D. Ray, C. Koerner, M. Riede, K. Leo, I. D. Samuel and K. Vandewal, *Adv Mater*, 2017, **29**, 1604424.

55. O. V. Mikhnenko, P. W. M. Blom and T.-Q. Nguyen, *Energy & Environmental Science*, 2015, **8**, 1867-1888.
56. G. Rotas, M. B. Thomas, R. Canton-Vitoria, F. D'Souza and N. Tagmatarchis, *Chemistry*, 2020, **26**, 6652-6661.
57. S. K. Das, B. Song, A. Mahler, V. N. Nesterov, A. K. Wilson, O. Ito and F. D'Souza, *The Journal of Physical Chemistry C*, 2014, **118**, 3994-4006.
58. A. Huijser, T. J. Savenije, S. C. Meskers, M. J. Vermeulen and L. D. Siebbeles, *J Am Chem Soc*, 2008, **130**, 12496-12500.
59. S. Ryuzaki, T. Hasegawa and J. Onoe, *Journal of Applied Physics*, 2009, **105**, 113529.
60. C. Gu, H. Zhang, J. Yu, Q. Shen, G. Luo, X. Chen, P. Xue, Z. Wang and J. Hu, *Nano Lett*, 2021, **21**, 1102-1107.
61. M. Vasilopoulou, A. M. Douvas, D. G. Georgiadou, V. Constantoudis, D. Davazoglou, S. Kennou, L. C. Palilis, D. Daphnomili, A. G. Coutsolelos and P. Argitis, *Nano Research*, 2014, **7**, 679-693.
62. N. Kumaran, P. A. Veneman, B. A. Minch, A. Mudalige, J. E. Pemberton, D. F. O'Brien and N. R. Armstrong, *Chemistry of Materials*, 2010, **22**, 2491-2501.
63. L. Đorđević, N. Demitri and D. Bonifazi, *Supramolecular Chemistry*, 2016, **28**, 753-761.
64. A. Huijser, T. J. Savenije, J. E. Kroeze and L. D. Siebbeles, *J Phys Chem B*, 2005, **109**, 20166-20173.
65. L. D. A. Siebbeles, A. Huijser and T. J. Savenije, *Journal of Materials Chemistry*, 2009, **19**, 6067-6072.
66. J. M. Ha, S. H. Hur, A. Pathak, J.-E. Jeong and H. Y. Woo, *NPG Asia Materials*, 2021, **13**, 53.
67. V. F. Traven, D. A. Cheptsov and C. Lodeiro, *J Fluoresc*, 2023, **33**, 799-847.
68. G. Hong, X. Gan, C. Leonhardt, Z. Zhang, J. Seibert, J. M. Busch and S. Brase, *Adv Mater*, 2021, **33**, e2005630.
69. C. Xu, Z. Zhao, K. Yang, L. Niu, X. Ma, Z. Zhou, X. L. Zhang and F. Zhang, *Journal of Materials Chemistry A*, 2022, **10**, 6291-6329.
70. L. Wang, S. Guo, K. Zhou and W. Ma, *Sustainable Energy & Fuels*, 2020, **4**, 4934-4955.
71. C. Gu, X. Wang, H. Wang, Y. Tian, J. Ma and R. Yang, *Molecular Systems Design & Engineering*, 2022, **7**, 832-855.
72. L. Wu, C. Huang, B. P. Emery, A. C. Sedgwick, S. D. Bull, X. P. He, H. Tian, J. Yoon, J. L. Sessler and T. D. James, *Chem Soc Rev*, 2020, **49**, 5110-5139.
73. H. Shuai, C. Xiang, L. Qian, F. Bin, L. Xiaohui, D. Jipeng, Z. Chang, L. Jiahui and Z. Wenbin, *Dyes and Pigments*, 2021, **187**, 109125.
74. J. Li and K. Pu, *Chem Soc Rev*, 2019, **48**, 38-71.
75. B. Lu, H. Yuying, H. Quan, Z. Zhang and Y. Yao, *Materials Chemistry Frontiers*, 2022, **6**, 2968-2993.
76. J. Zhang, X. Zhao, H. Shen, J. W. Lam, H. Zhang and B. Z. Tang, *Advanced Photonics*, 2021, **4**, 014001.
77. N. Muhamad Sarih, P. Myers, A. Slater, B. Slater, Z. Abdullah, H. A. Tajuddin and S. Maher, *Sci Rep*, 2019, **9**, 11834.
78. K. Panigrahi and A. Nag, *The Journal of Physical Chemistry C*, 2022, **126**, 8553-8564.
79. S. Kundu, B. Sk, P. Pallavi, A. Giri and A. Patra, *Chemistry*, 2020, **26**, 5557-5582.
80. D. Bevk, L. Marin, L. Lutsen, D. Vanderzande and W. Maes, *RSC Advances*, 2013, **3**, 11418-11431.
81. G. Reginato, A. Mordini, L. Zani, M. Calamante and A. Dessì, *European Journal of Organic Chemistry*, 2016, **2016**, 233-251.
82. Y. Z. Yousif and A. J. Al-hamdani, *Liquid Crystals*, 1993, **15**, 451-460.

83. J. Bartulin, C. Zuñiga, H. Muller and T. R. Taylor, *Molecular Crystals and Liquid Crystals Incorporating Nonlinear Optics*, 1990, **180**, 297-304.
84. I. Osaka, M. Saito and K. Takimiya, *NIHON GAZO GAKKAISHI (Journal of the Imaging Society of Japan)*, 2014, **53**, 523-528.
85. N. A. Sayresmith, A. Saminathan, J. K. Sailer, S. M. Patberg, K. Sandor, Y. Krishnan and M. G. Walter, *J Am Chem Soc*, 2019, **141**, 18780-18790.
86. A. R. Brotherton, A. Shibu, J. C. Meadows, N. A. Sayresmith, C. E. Brown, A. M. Ledezma, T. A. Schmedake and M. G. Walter, *Adv Sci (Weinh)*, 2023, **10**, e2205729.
87. H. Z. Akpinar, Y. A. Udum and L. Toppare, *Journal of Polymer Science Part A: Polymer Chemistry*, 2013, **51**, 3901-3906.
88. U. Olgun and M. Gülfen, *Reactive and Functional Polymers*, 2014, **77**, 23-29.
89. U. Olgun and M. Gülfen, *RSC Adv.*, 2014, **4**, 25165-25171.
90. T.-X. Wang, H.-P. Liang, D. A. Anito, X. Ding and B.-H. Han, *Journal of materials chemistry A*, 2020, **8**, 7003-7034.
91. Q. Huang, L. Guo, N. Wang, X. Zhu, S. Jin and B. Tan, *ACS Appl Mater Interfaces*, 2019, **11**, 15861-15868.
92. Q. Shi, H. Fan, Y. Liu, J. Chen, Z. Shuai, W. Hu, Y. Li and X. Zhan, *Journal of Polymer Science Part A: Polymer Chemistry*, 2011, **49**, 4875-4885.
93. O. P. Dimitriev, *Chem Rev*, 2022, **122**, 8487-8593.
94. K. Wang, H. Zhang, S. Chen, G. Yang, J. Zhang, W. Tian, Z. Su and Y. Wang, *Advanced Materials*, 2014, **26**, 6168-6173.
95. M. Ghora, P. Majumdar, M. Anas and S. Varghese, *Chemistry*, 2020, **26**, 14488-14495.
96. J. Gierschner, J. Shi, B. Milián-Medina, D. Roca-Sanjuán, S. Varghese and S. Park, *Advanced Optical Materials*, 2021, **9**, 2002251.
97. S. Hamai and F. Hirayama, *The Journal of Physical Chemistry*, 2002, **87**, 83-89.
98. S. Ando, D. Kumaki, J.-i. Nishida, H. Tada, Y. Inoue, S. Tokito and Y. Yamashita, *J. Mater. Chem.*, 2007, **17**, 553-558.
99. G. M. Sheldrick, *Acta Crystallogr A*, 2008, **64**, 112-122.
100. O. V. Dolomanov, L. J. Bourhis, R. J. Gildea, J. A. Howard and H. Puschmann, *Journal of applied crystallography*, 2009, **42**, 339-341.
101. A. S. Glassner, *Principles of digital image synthesis*, Elsevier, 2014.
102. J. F. Varner, N. Eldabagh, D. Volta, R. Eldabagh and J. J. Foley, *Journal of open research software*, 2019, **7**.
103. T. W. F. M. Mansencal, Michael; Parsons, Michael; Shaw, Nick; Wheatley, Kevin; Cooper, Sean; Vandenberg, Jean D.; Canavan, Luke; Crowson, Katherine; Lev, Ofek; Leinweber, Katrin; Sharma, Shriramana; Sobotka, Troy James; Moritz, Dominik; Pppp, Matt; Rane, Chinmay; Eswaramoorthy, Pavithra; Mertic, John; Pearlstine, Ben; Leonhardt, Manuel; Niemitalo, Olli; Szymanski, Marek; Schambach, Maximilian; Huang, Sianyi; Wei, Mike; Joywardhan, Nishant; Wagih, Omar; Redman, Pawel; Goldstone, Joseph; Hill, Stephen; Smith, Jedediah; Savoir, Frederic; Saxena, Geetansh; Chopra, Saransh; Sibiryakov, Ilia; Gates, Tim; Pal, Gajendra; Tessore, Nicolas; Pierre, Aurélien; Thomas, François-Xavier; Srinivasan, Sabarish; Downs, Tucker, *Journal*, 2022, DOI: 10.5281/zenodo.7367239.
104. A. Huang, Q. Li and Z. Li, *Chinese Journal of Chemistry*, 2022, **40**, 2356-2370.
105. T. Iwasaki, S. Murakami, Y. Takeda, G. Fukuhara, N. Tohnai, Y. Yakiyama, H. Sakurai and N. Kambe, *Chemistry*, 2019, **25**, 14817-14825.
106. Q. Li and Z. Li, *Accounts of chemical research*, 2020, **53**, 962-973.
107. A. Shibu, C. Middleton, C. O. Kwiatkowski, M. Kaushal, J. H. Gillen and M. G. Walter, *Molecules*, 2022, **27**, 35.

108. R. Thomas, S. Varghese and G. U. Kulkarni, *Journal of Materials Chemistry*, 2009, **19**, 4401-4406.
109. J. Yang, X. Zhen, B. Wang, X. Gao, Z. Ren, J. Wang, Y. Xie, J. Li, Q. Peng, K. Pu and Z. Li, *Nature Communications*, 2018, **9**, 840.
110. Z. Liu, Y. Tian, J. Yang, A. Li, Y. Wang, J. Ren, M. Fang, B. Z. Tang and Z. Li, *Light: Science & Applications*, 2022, **11**, 142.
111. P. R. Spackman, M. J. Turner, J. J. McKinnon, S. K. Wolff, D. J. Grimwood, D. Jayatilaka and M. A. Spackman, *J Appl Crystallogr*, 2021, **54**, 1006-1011.
112. Y. C. Wei, S. W. Shen, C. H. Wu, S. Y. Ho, Z. Zhang, C. I. Wu and P. T. Chou, *J Phys Chem A*, 2021, **125**, 943-953.
113. P. Irkhin, A. Ryasnyanskiy, M. Koehler and I. Biaggio, *Physical Review B*, 2012, **86**, 085143.
114. Y.-C. Wei, Z. Zhang, Y.-A. Chen, C.-H. Wu, Z.-Y. Liu, S.-Y. Ho, J.-C. Liu, J.-A. Lin and P.-T. Chou, *Communications Chemistry*, 2019, **2**, 10.
115. M. Brinkmann, G. Gadret, M. Muccini, C. Taliani, N. Masciocchi and A. Sironi, *Journal of the American Chemical Society*, 2000, **122**, 5147-5157.
116. M. L. Clapham, R. R. Frontiera and C. J. Douglas, *Crystal Growth & Design*, 2023, **23**, 3942-3946.
117. E. Venuti, I. Bilotti, R. G. Della Valle, A. Brillante, P. Ranzieri, M. Masino and A. Girlando, *The Journal of Physical Chemistry C*, 2008, **112**, 17416-17422.
118. B. Subramanian, N. Tchoukanova, Y. Djaoued, C. Pelletier and M. Ferron, *Journal of Raman Spectroscopy*, 2013, **44**, 219-226.
119. N. Q. Shikhaliyev, S. T. Çelikesir, M. Akkurt, K. N. Bagirova, G. T. Suleymanova and F. A. Toze, *Acta Crystallographica Section E: Crystallographic Communications*, 2019, **75**, 465-469.
120. J. Birks, *Reports on progress in physics*, 1975, **38**, 903.
121. T. Förster, *Angewandte Chemie International Edition in English*, 1969, **8**, 333-343.
122. B. Stevens and E. Hutton, *Nature*, 1960, **186**, 1045-1046.
123. J. Mei, N. L. C. Leung, R. T. K. Kwok, J. W. Y. Lam and B. Z. Tang, *Chemical Reviews*, 2015, **115**, 11718-11940.
124. A. Musser, S. K. Rajendran, K. Georgiou, L. Gai, R. Grant, Z. Shen, M. Cavazzini, A. Ruseckas, G. A. Turnbull and I. D. W. Samuel, *Journal of Materials Chemistry C*, 2017, **5**, 8380-8389.
125. F. M. Winnik, *Chemical reviews*, 1993, **93**, 587-614.
126. Y.-H. Chen, K.-C. Tang, Y.-T. Chen, J.-Y. Shen, Y.-S. Wu, S.-H. Liu, C.-S. Lee, C.-H. Chen, T.-Y. Lai and S.-H. Tung, *Chemical Science*, 2016, **7**, 3556-3563.
127. A. Garci, Y. Beldjoudi, M. S. Kodaimati, J. E. Hornick, M. T. Nguyen, M. M. Cetin, C. L. Stern, I. Roy, E. A. Weiss and J. F. Stoddart, *Journal of the American Chemical Society*, 2020, **142**, 7956-7967.
128. S. Karuppannan and J. C. Chambron, *Chemistry–An Asian Journal*, 2011, **6**, 964-984.
129. J. Han, Y. Ding, X. Lv, Y. Zhang and D. Fan, *Biosensors*, 2023, **13**, 489.
130. C. Wu, L. Yan, C. Wang, H. Lin, C. Wang, X. Chen and C. J. Yang, *Biosensors and Bioelectronics*, 2010, **25**, 2232-2237.
131. Y. Zhong, J. Zhan, G. Xu, Y. Chen, Q. Qin, X. Liao, S. Ma, Z. Yang and Y. Cai, *Angewandte Chemie International Edition*, 2021, **60**, 8121-8129.
132. B. Santiago-Gonzalez, A. Monguzzi, J. M. Azpiroz, M. Prato, S. Erratico, M. Campione, R. Lorenzi, J. Pedrini, C. Santambrogio and Y. Torrente, *Science*, 2016, **353**, 571-575.
133. A. Thomas, S. Polarz and M. Antonietti, *The Journal of Physical Chemistry B*, 2003, **107**, 5081-5087.

134. Y. Zhao, P. Xu, K. Zhang, H. Schönherr and B. Song, *Cell Reports Physical Science*, 2022, **3**.
135. M. Inouye, K. Hayashi, Y. Yonenaga, T. Itou, K. Fujimoto, T. a. Uchida, M. Iwamura and K. Nozaki, *Angewandte Chemie International Edition*, 2014, **53**, 14392-14396.
136. Y. Appiarius, P. J. Gliese, S. A. W. Segler, P. Rusch, J. Zhang, P. J. Gates, R. Pal, L. A. Malaspina, K. Sugimoto, T. Neudecker, N. C. Bigall, S. Grabowsky, A. A. Bakulin and A. Staubitz, *The Journal of Physical Chemistry C*, 2022, **126**, 4563-4576.
137. Z. Zhao, S. Chen, J. W. Lam, Z. Wang, P. Lu, F. Mahtab, H. H. Sung, I. D. Williams, Y. Ma and H. S. Kwok, *Journal of Materials Chemistry*, 2011, **21**, 7210-7216.
138. P. Pinter, H. Mangold, I. Stengel, I. Münster and T. Strassner, *Organometallics*, 2016, **35**, 673-680.
139. X. Shan, W. Chi, H. Jiang, Z. Luo, C. Qian, H. Wu and Y. Zhao, *Angewandte Chemie International Edition*, 2023, **62**, e202215652.
140. H. Yoo, J. Yang, A. Yousef, M. R. Wasielewski and D. Kim, *Journal of the American Chemical Society*, 2010, **132**, 3939-3944.
141. E. Wellner, M. Ottolenghi, D. Avnir and D. Huppert, *Langmuir*, 1986, **2**, 616-619.
142. S. Ogawa, T. Wakayama, H. Watanabe, K. Hayashi, S. Ogata, Y. Oaki, M. Hasegawa and H. Imai, *Bulletin of the Chemical Society of Japan*, 2018, **91**, 87-91.
143. M. Saito, K. Ito and H. Yokoyama, *Macromolecules*, 2021, **54**, 8538-8547.
144. G. Lubarsky, M. Davidson and R. Bradley, *Surface science*, 2004, **558**, 135-144.
145. A. G. Leal-Junior, C. Marques, A. Frizera and M. J. Pontes, *IEEE Sensors Journal*, 2018, **18**, 2353-2361.